To the Graduate Council:
I am submitting herewith a dissertation written by Meenambika Gowrishankar entitled "Error Management on Near-Term Quantum Computers." I have examined the final paper copy of this dissertation for form and content and recommend that it be accepted in partial fulfillment of the requirements for the degree of Doctor of Philosophy, with a major in Energy Science and Engineering.

Travis Humble, Major Professor

We have read this dissertation
and recommend its acceptance:

Rebekah Herrman

Himanshu Thapliyal

Jim Ostrowski

Accepted for the Council:

Dixie L. Thompson

Vice Provost and Dean of the Graduate School

To the Graduate Council:
I am submitting herewith a dissertation written by Meenambika Gowrishankar entitled “Error Management on Near-Term Quantum Computers.” I have examined the final electronic copy of this dissertation for form and content and recommend that it be accepted in partial fulfillment of the requirements for the degree of Doctor of Philosophy, with a major in Energy Science and Engineering.

Travis Humble, Major Professor

We have read this dissertation
and recommend its acceptance:

Rebekah Herrman

Himanshu Thapliyal

Jim Ostrowski

Accepted for the Council:

Dixie L. Thompson

Vice Provost and Dean of the Graduate School

(Original signatures are on file with official student records.)

Error Management on Near-Term Quantum Computers

A Dissertation Presented for the
Doctor of Philosophy
Degree
The University of Tennessee, Knoxville

Meenambika Gowrishankar
December 2024

I would not have been able to pursue this PhD as comfortably as I did without the constant and unwavering patience, encouragement, support and advice of my mother, Meenakshi Gowrishankar and sister, Visalaakshi Gowrishankar. I also received enourmous support from my husband, Ganapathy Premkumar, who constantly cheered me on especially during some of the most demanding times, particularly during the tail end of the PhD. I am also very lucky to have friends with whom I could discuss the common trials and tribulations of pursuing a PhD and who offered continuous support and encouragement especially during challenging times in my personal life. I dedicate this thesis to my family and all my friends for they form a big part of the successful completion of this dissertation.

Acknowledgements

I would like to thank my advisor, Dr. Travis Humble, for his continuous and unwavering support towards my graduate education and professional development. I particularly received excellent support during the time of the COVID pandemic, and I am immensely thankful for his patience and kindness during such challenging times. I would like to also thank my committee members, Dr. Rebekah Herrman, Dr. Himanshu Thapliyal and Dr. Jim Ostrowski, for their support, encouragement and feedback that led to a more complete final version of the dissertation. I thank the Department of Energy for funding my research and the Oak Ridge Leadership Computing Facility for providing the access and resources that enabled me to perform the computations for my research. And last but not least, I would like to thank Allie Burns, Dr. Suresh Babu, Dr. Lee Riedinger and others at the Bredesen Center for Interdisciplinary Science and Research at the University of Tennessee for all their help and support to make this PhD across two institutions, the University of Tennessee and Oak Ridge National Laboratory, possible.

vidyā dadāti vinayaṃ vinayād yāti pātratām |
pātratvāt dhanam āpnoti dhanād dharmaṃ tataḥ sukham ||
-Hitopadeśa

Abstract

Quantum computing devices are developing at a rapid pace with error rates that are on the cusp of early fault tolerance. The promise quantum computing offers for quantum chemistry is exponential speed up in simulations of large scale molecular systems with enough accuracy to predict outcomes of experiments in the real world. Delivering on the promise of high accuracy and precision requires methods to evaluate the computational accuracy of the quantum computing devices. We develop and demonstrate a device agnostic framework to benchmark the computational accuracy of near-term noisy intermediate scale quantum computing (NISQ) devices using a quantum chemistry application and the domain specific threshold of chemical accuracy. We use numerical simulations of noisy quantum circuits to model the impact of noise on the accuracy and variance of the energy estimate, and the fidelity of the prepared state when simulating the ground state of prototypical two-electron chemistry problems using a near-term quantum-classical algorithm, the variational quantum eigensolver (VQE). We use device agnostic error-mitigation schemes, quantum error detection (QED) and read out error detection, with post-selection, to mitigate different types of noise and show improvement in the accuracy of the results along with the impact on the precision due to post-selection. With this framework of evaluating the computational accuracy of a quantum computing device we estimate the resources required to perform the benchmark and demonstrate the analysis for a commercially available trapped-ion device.

Table of Contents

List of Tables

List of Figures

Chapter 1

Introduction

Energy is the bedrock of civilization. From heating homes to powering our vehicles to exploring outer space, the need for energy touches every aspect of our lives. The industrial revolution that propelled us to the modern age of information technology is entirely due to discoveries of new sources of energy and means to convert one form of energy to another. Today we face a situation marked by a finite source of energy that fuels much of our modern life, i.e, fossil fuels. And we are on the lookout for ways to use finite sources of fuel more efficiently while engaging in the pursuit of generating and storing energy from renewable sources Smil (2004, 2018); Solomon and Krishna (2011).

As in the case of all such pursuits, scientific research is at the heart of finding new and innovative solutions. And at the heart of all such research today, is a much used resource: the computer. Just as in our daily life, there are not many fields of scientific research today left untouched by the power of computation, be it speeding up research in the lab by using predictions based on simulations on a supercomputer or finding solutions to optimization problems for various applications in the real world or validating hypotheses in the theoretical sciences. Computation is the mainstay or the supporting resource in nearly all fields of research. However, there are some specific niche problems that are hard to solve efficiently even with the fastest super computer. And these niche problems have real world consequences some of which directly impact the efficient use of energy.

An example of such a problem is understanding the activity of an enzyme in nature called nitrogenase, which converts nitrogen to ammonia under ambient temperature and pressure. The corresponding industrial manufacturing process currently uses about 1% of the energy globally due to the high pressure and temperature required, and is responsible for nearly as much emission McArdle et al. (2020); Hoffman et al. (2014); Capdevila-Cortada (2019). The significant proportion of energy consumption is due to ammonia being critical for fertilizer production, which is in turn critical for agriculture. Nearly half of the world's population relies on industrially produced ammonia for agriculture. Understanding the activity of the enzyme and replicating it, therefore, has enormous implications both for energy efficiency and agriculture worldwide Hoffman et al. (2014). As a result, it is an extensively studied topic both experimentally and computationally. However, not much is known about the mechanism of this process, which is complicated by the involvement of multiple transition metals (iron, molybdenum and cobalt) and the resulting strong electron correlation, a phenomena found in many transition metal catalysts important for various real world applications McArdle et al. (2020); Reiher et al. (2017); Hoffman et al. (2014). While there has been considerable experimental and computational effort to understand the kinetics of the nitrogenase enzyme, not much is known yet due to the presence of strong electron correlation, a phenomena found in many transition metal catalysts important for various real world applications.

Gaining insight into the mechanism of any chemical process requires the knowledge of the rate constants that govern the reactions that are part of the process. The rate constants for the various reactions inform the transformations of the intermediates involved and are derived from the energies of the stable intermediates, a property that can be calculated using computational methods Reiher et al. (2017). Calculation of energies to reliably predict reaction rates requires very high quantitative accuracy and is defined by the threshold known as chemical accuracy, a quantity that bridges the gap between the accuracy required from a computational method to make experimental predictions in the real world Peterson et al. (2012); McArdle et al. (2020); Cao et al. (2019b). Using computational quantum chemistry methods to extract this information by simulating just the active space of this enzyme on a conventional or classical digital computer is considered intractable as the cost of the simulation scales exponentially with system size just in the amount of memory and time Lloyd (1996).

Methods in computational chemistry for calculating exact energy of molecules scale exponentially with system size both in terms of time and space required Lloyd (1996); McArdle et al. (2020); Elfving et al. (2020). For instance, the full configuration interaction (FCI) is a method in computational chemistry for exact energy calculation for a given basis set. Making an FCI calculation on a classical computer scales by nearly $\mathcal{O}(M^N)$ in terms of the memory required, where M is the number of spin orbitals and N is the number of electrons, while simulating the same wavefunction on a quantum computer would require M qubits McArdle et al. (2020); Aspuru-Guzik et al. (2005). As a result, simulating the active space of the nitrogenase enzyme on a small error-corrected quantum computer may be accomplished with as few as a 120 qubits, albeit perfect qubits, without loss of accuracy and is expected to provide exponential speed ups over classical computation for the same problem Lidar and Wang (1999); Reiher et al. (2017); McArdle et al. (2020).

This is just one example of a problem that is intractable for the fastest classical supercomputer today and in the foreseeable future. Many such simulations in physics and chemistry that are critical to understanding mechanisms to improve energy efficiency and energy storage are part of this niche set of problems that, while being intractable for a classical computer, may be efficiently simulated using a quantum computer Paudel et al. (2022); Rice et al. (2021); Von Burg et al. (2021); Elfving et al. (2020); McArdle et al. (2020).

1.1 Quantum Computing

Quantum computing promises a computational advantage over conventional digital computers for some specific problems that are believed to be as yet classically intractable. A problem is considered tractable if the algorithm to find its solutions within a given computational model requires resources in terms of space and time that are polynomial in input size and intractable if they scale faster than polynomial or exponentially with size of the input. Among these problems are prime factorization of integers, unstructured search, and quantum simulation which have important consequences in fields such as cryptography, and the simulation of large scale systems in quantum physics and chemistry as argued in the 80s by Richard Feynman Feynman (1982); Shor (1994, 1999); Grover (1997); Abrams and Lloyd (1999); Kitaev (1997); Yung et al. (2014); Nielsen and Chuang (2010b). The quantum algorithms for finding solutions to these problems promise substantial speed ups over their classical counterparts.

Quantum computers differ from classical computers in the way information is encoded and processed for computation Lloyd (1996). Classical computers encode information using transistors in binary bits, 0 and 1 representing the state of absence or presence of voltage on the transistor. The information is processed using a universal gate set of AND, NOT and OR. Quantum computers encode information in quantum bits or qubits which in addition to the states 0 and 1, can be in states that are in a superposition of 0 and 1, enabling exponential scaling in storage with increase in number of qubits. This is discussed in more detail in chapter 2. There are different models of quantum computation such as adiabatic quantum computation, continuous variable quantum computation and measurement based quantum computation Lloyd and Braunstein (1999); Farhi et al. (2000); Aharonov et al. (2008); Raussendorf and Briegel (2001); Raussendorf et al. (2003); Braunstein and Van Loock (2005). The focus in this thesis will be on gate or circuit model of quantum computation which is closely analogous to the circuits and gate operations used in classical computers Nielsen and Chuang (2010a).

A required feature for computational devices is accuracy which is ensured by detection and minimization or elimination of errors. Combating errors in quantum computers is not as straightforward as in classical computers where redundancy by the ability to copy information into multiple bits can be exploited to arrive at the correct information by, in the simplest case, a majority vote. Copying the information of an unknown quantum system or state, however, is prohibited by quantum mechanics due to the no-cloning theorem Nielsen and Chuang (2010a); Wootters and Zurek (1982); Park (1970). Additionally, classical computers have to protect information only against one type of error: the bit flip error. The quantum computer on the other hand has to additionally protect against phase flip errors. These factors proved to be a challenge for quantum computation till a key development in 1995 and 1996 when Peter Shor and others discovered quantum error correction (QEC) algorithms to protect quantum information during quantum computation using the quantum mechanical property known as entanglement which was also the cause of the errors Shor (1995a, 1996); Calderbank and Shor (1996); Steane (1996). This milestone paved the way for experimental realization of quantum computers. Since then quantum computational devices have made several leaps from small quantum devices with one to three qubits to industrial/commercial development of quantum hardware with more than 100 qubits and a wide variety of architectures including but not limited to superconducting, ion-trap, quantum-dot, photonic, nitrogen vacancy and toplogical quantum computersDevoret et al. (2004); Cory et al. (1997); Gershenfeld and Chuang (1997); Loss and DiVincenzo (1998); Adami and Cerf (1999); Wineland et al. (1999); Sørensen and Mølmer (1999); Imamoglu et al. (1999); Ramanathan et al. (2005); Kok et al. (2007); Blatt and Wineland (2008); Nayak et al. (2008); Devoret and Schoelkopf (2013); Monroe and Kim (2013); Doherty et al. (2013); Barends et al. (2013); Córcoles et al. (2015);

Gambetta et al. (2017); Wendin (2017); Bernien et al. (2017); Mi et al. (2018); Saffman (2019).

A major milestone in the process was the demonstration of quantum supremacy in 2019 and 2020, in which the performance of a quantum computer outdid a classical computer in terms of the speed with which it was able to solve a sampling problem Arute et al. (2019); Zhong et al. (2020). Google AI demonstrated preparation of quantum states over 53 qubits (statespace of $2^{53} \approx 10^{16}$) and sampled from the resulting probability distribution repeatedly. They reported taking a million measurements of a single instance of a quantum circuit in 200 seconds. An equivalent task with the state-of-the-art classical supercomputer was determined to require 10,000 years at the time of the experiment. The second study at the University of Science and Technology of China demonstrated supremacy using a Gaussian boson sampling task with the dimension of the output statespace of 10^{30} and reported that the sampling rate was faster by a factor of $\sim 10^{14}$ than the classical equivalent.

Quantum error correction codes protect quantum information by redundantly encoding a single logical qubit using several physical qubits, decoding the error events as they occur and applying recovery or correction operations based on the decoded information. Even though the discovery of QEC codes spurred the development of quantum computing devices, the number of qubits required for the implementation of quantum error correction codes increases with the number of logical qubits and the scale depends on the the QEC code. Additionally, errors in a quantum computer can propagate due to entanglement and accumulate over the course of computation, making it a challenging task to implement error correction when the operations required for the implementation themselves can introduce error in the computation. This particular concern was resolved by the idea of fault tolerant quantum computing (FTQC), which is the design of gate operations and error correction protocols such that the propagated and accumulated errors during the computation are removed and managed. FTQC imposes a constraint that makes successful fault tolerant error correction and scalable quantum computation possible. The constraint is described by the threshold theorem, which is the threshold of error or noise below which a quantum error correction code can be used without propagation of errors, and is a quantity that varies depending on the QEC code Aharonov and Ben-Or (1997). However, both QEC and FTQC require qubits in the order of millions and orders of magnitude higher number of gate operations than currently available to successfully implement any of the quantum algorithms for the problems described earlier Fowler et al. (2012). Nevertheless, it is the predominant challenge for quantum computing and a highly active area of research with many recent breakthroughs Bluvstein et al. (2024); AI (2023); Livingston et al. (2022); Sivak et al. (2023); Ryan-Anderson et al. (2021); Krinner et al. (2022); Acharya et al. (2023); Mayer et al. (2024). The devices are also achieving ever lower gate error rates of $0.5 - 0.01\%$ per two-qubit gate (AI, 2023; Evered et al., 2023; Yamamoto et al., 2024).

The errors in quantum computers result from quantum noise which arise from different sources that corrupt the information encoded in a qubit. Some of the types of quantum noise are environmental decoherence, which introduces errors due to the interaction of the quantum computer with the environment and coherent control errors, which can occur while calibrating or implementing gates on the quantum computer. There are also more complicated sources of error such as crosstalk, where interactions with neighboring qubits introduce errors. Due to this sensitivity of the quantum devices, they need to be sufficiently isolated from the environment while also allowing controlled operations to perform the desired computation.

On the journey to quantum fault tolerance, there are now devices of a wide variety that are available for experiments and some are even being tested for commercial applications. This has been made possible in spite of qubits that have higher error rates than required for QEC, and low lifetimes, due to techniques such as quantum error mitigation that improve the signal to noise ratio of qubits based on the noise profile of the qubits obtained from prior characterization experiments.

With the advent of these devices, now known as noisy intermediate scale quantum (NISQ) computers Preskill (2018a), there are a plethora of algorithms and error mitigation techniques that have been specifically designed for use on a near term quantum computer in conjunction with a classical computer. The variational quantum eigensolver (VQE) and quantum approximate optimization algorithms (QAOA) are examples of such algorithms and are often referred to as quantum-classical hybrid algorithms Peruzzo et al. (2014a); Farhi et al. (2014). A part of the algorithm, which is the preparation of a parameterized quantum state, is handled by the quantum hardware and the parameter optimization is handled by the classical computer. These algorithms are both a means to benchmark quantum computers and to extract utility out of near term noisy quantum computers.

Quantum error mitigation techniques were developed to combat noise on near-term devices. They are distinct from QEC codes and are either targeted towards specific types of noise, like randomized compiling, which converts coherent noise to stochastic noise by twirling circuits and averaging over several circuit executions, or can be implemented more generally, such as zero noise extrapolation, which extrapolates the correct answer by calculating estimates from executions with increasing noise and extrapolating to zero noise by curve fitting Wallman and Emerson (2016a); Hashim et al. (2020); Li and Benjamin (2017); Temme et al. (2017a). More recently, probabilistic error cancellation has emerged as another error mitigation technique that uses noise characterization from the device to develop a quasi-probability distribution to cancel the noiseTemme et al. (2017a). These mitigation techniques require some knowledge about the noise profile of the device and hence, depend on noise characterization, and as a result, the scalability of these techniques remains a challenge Takagi et al. (2022). There are also other problem specific error mitigation strategies such as quantum subspace expansion, methods targeted towards VQE ansatzes and using symmetries in quantum circuits Sagastizabal et al. (2019a); McClean et al. (2017); Sagastizabal et al. (2019b); Bonet-Monroig et al. (2018).

Quantum error detection (QED) codes sit somewhere in the middle of QEC and quantum error mitigation, although they lean much closer to QEC in structure and technique. They are codes that encode a logical qubit using several physical qubits just as in quantum error correction. However, quantum error correction codes can detect the location and type of error that has occurred at a given moment in time of the computation. Quantum error detection codes can only detect that an error has occurred and the type of error that has occurred but not the location of the error Devitt et al. (2013). They reduce errors in computation by discarding or post-selecting outcomes with detected error events. They have been studied and applied in experiments and provide improved results even at high error rates Knill (2004); Aliferis et al. (2007); Reichardt (2009); Vuillot (2017).

With such a wide variety of quantum computers available commercially, the ever lower error rates, and the several techniques for error mitigation, there is a question of whether these computers, even with noisy qubits, can be used for an application? If they are to be used for an application, then the computational accuracy of the device must be known to estimate the accuracy of the result of the application. However, how do we verify or benchmark the accuracy of the device?

Accuracy is a metric that describes how close an outcome is to the correct answer and entirely dependent on the sampling and measurement process. For a known answer, the difference between the measured outcome and the target or correct outcome is the measure of accuracy. However, the repeatability of this accurate measurement is an equally important measure to completely evaluate the accuracy of a given measurement and particularly, the accuracy of the device being used for the measurement Dasgupta and Humble (2021). Therefore, both the difference between the measured outcome and the target outcome and the uncertainty in the measured outcome are required to evaluate the computational accuracy of a given device.

Accuracy of results on near term quantum computers have been reported several times in literature. Some studies focused on demonstrating improvement in accuracy of the results for some small problems Sokolov et al. (2023); Urbanek et al. (2020b); Peruzzo et al. (2014a); Fauseweh and Zhu (2021); Motta et al. (2020); Urbanek et al. (2020a). One of the earlier quantum chemistry simulations using the VQE and the phase estimation algorithm demonstrated within chemical accuracy for the VQE algorithm O'Malley et al. (2016). They show that the calculation of dissociation energy defined as the energy difference between energy at equilibrium bond distance and distance at which dissociation occurs is within $(8 \pm 5) \times 10^{-4}$Ha, although the accuracy of the ground state energies at those distances is not reported. Many other studies also report results within chemical accuracy for similar simulationsMcCaskey et al. (2019); Google AI Quantum et al. (2020). While the results from Google AI include error bars in the potential energy surface plots presented, the magnitude of these error bars is difficult to gauge visually. Google AI used different error mitigation strategies and also used their study to evaluate the accuracy of their device. The study by McCaskey et al. (2019) demonstrated results within chemical accuracy with error mitigation on a device by Rigetti QCS accessed using remote cloud quantum computing resources. The magnitude of error bars is reported to be in the order of 10^{-3} for some of the calculations. As described above, near term quantum computers are prone to noise that obscure the signal and therefore, require methods to manage the resulting errors in order to get a sufficiently large signal to noise ratio so as to evaluate the accuracy and precision of the device. Some studies in literature evaluating the device or reporting on the accuracy of the calculation often involve one or more techniques of quantum error mitigation in order to combat noise in a given quantum computing hardware.

One of the studies exclusively evaluating the accuracy of the device as part of their investigation reported on the results of simulating the same unitary operation forwards and backwards in time on an IBM device, which in the ideal case would result in the final state being the same as initial state Smith et al. (2019). Another study also evaluated the accuracy of two IBM devices using a two-, three- and four-qubit Grover's algorithm and compared the results to the expected theoretical accuracy of $> 95\%$ Mandviwalla et al. (2018). This study reported on the standard deviation of their calculations and found it to be small at about 1.5% compared to deviations from the theoretical results (74% accuracy on average compared to the expected $> 95\%$) indicating low variance in the device measurements with low accuracy.

In these test cases, accuracy indicates the absolute error of the experimental result from the known exact result. However, even when the result is within the accuracy threshold, how reproducible that accuracy is on the given device is determined by the precision of the calculation. Because most near term quantum classical hybrid algorithms estimate the answer by sampling and averaging, a straightforward metric to measure the certainty of the accuracy of the result, is the standard deviation or more precisely, the standard error of the mean. This determines whether the observed accuracy of the instrument being used is reproducible. From the experiments reporting accuracy of results, while the estimated quantity is within the domain specific accuracy threshold, it is not clear that the uncertainty in the calculation is small enough to reproduce the calculation within that same threshold. Quantum computing promises quantitative accuracy for quantum chemistry calculations to make reliable predictions about reaction dynamics that will inform real world applications such as improving efficiency of the production of ammonia for agriculture. Given the significance of quantitative accuracy, an important step towards building a quantum computer that can answer such questions is to benchmark the computational accuracy of quantum computing devices as they are developed.

This dissertation investigates the question of computational accuracy of a given noisy near-term hardware by evaluating both the accuracy and precision of a problem with a known answer to determine whether a given calculation with error management and sufficient sampling falls within a defined accuracy threshold, and is reproducible. Such an evaluation of near-term hardware must involve techniques to manage errors from different sources and for the purposes of benchmarking, the more device agnostic the technique the better. As a result, algorithmic quantum error detection and read out error detection strategies are employed as the error mitigation methods against gate error and measurement error, respectively. Additionally, these methods do not depend on prior characterization of the device.

While there are many near term applications and algorithms that can be studied for this type of benchmarking experiment as described above, in keeping with the motivation for this research and like many others in the community, we select a small quantum chemistry application and an accuracy threshold defined within quantum chemistry known as chemical accuracy to extract the answer to this question. We use the most suitable near-term quantum-classical hybrid algorithm for the purpose, the variational quantum eigensolver. We first analyze the behavior of the algorithm in the presence of noise using numerical simulations. We then build upon recent results from Urbanek et al. (2020b), which used a quantum error detection code to counteract the noise, to numerically study the change in error rates, accuracy and precision with and without the use of the error detection code. We finally use this setup to evaluate the resources required to run simulations on a commercial device with techniques for error management to benchmark the computational accuracy of the device using the domain specific accuracy threshold known as chemical accuracy and the corresponding precision of the calculation.

We start with studying the accumulation of noise when using the VQE algorithm to simulate the ground state of the sodium hydride, a prototypical two-electron problem. We use numerical simulations and a standard single- and two-qubit gate depolarizing noise model to assess the impact of noise on optimal parameter corresponding to the minimum energy, the variance of the energy with respect to the ansatz we have considered and the accuracy of the energy estimate. We present the methods and results in chapter 3.

We extend the previous study by including different ansatzs and different optimizers. We simulate the same molecule under the same noise model to assess the impact of different optimizers and different logically equivalent variants of the original ansatz on the optimal parameter, the minimum energy and the variance of the energy in chapter 4.

In chapter 5 we investigate the impact of an error detection code with post-selection on the accuracy and precision of the energy estimates from the numerical simulation of VQE for molecular hydrogen. We perform an in-depth error analysis of the error detection code and report the contributions of the different post-selection methods involved towards the improved accuracy of the result. Additionally, we find that threshold of noise at which the energy estimates reach chemical accuracy is higher for the ansatz encoded with the error detection code compared to the unencoded ansatz.

In the final chapter, we use the methods developed in the chapter 5 to evaluate the resources required to benchmark the computational accuracy of a commercial quantum computing device from Quantinuum using the emulator provided by Quantinuum for their H1-1 device. The noise model used for the numerical simulations in chapter 5 did not include read out or measurement error, which is a dominant source of error in many quantum computing devices. We include a read out error detection strategy to mitigate read out error in addition to the [[4,2,2]] error detection code to mitigate gate and other Pauli errors. The results were evaluated in terms of both the accuracy of the energy expectation value and the precision of the outcome using standard error of the mean. The studies in the previous chapter indicate that the current two-qubit gate error rate of the H1-1 device and emulator might be low enough for the energy estimate to reach chemical accuracy provided the read out error is sufficiently mitigated. The accuracy and precision are compared against the domain specific threshold of chemical accuracy to estimate the computational accuracy of the device from the device emulator.

We find that the read out error detection code improves the accuracy of the energy for both the unencoded and encoded ansatzes with post-selection, especially the latter. It is particularly remarkable that the encoded ansatz with a higher qubit and gate overhead than the unencoded ansatz results in an estimate that is both lower than the estimate from the unencoded ansatz and reaches chemical accuracy. However, none of the estimates from the unencoded ansatz reach chemical accuracy. We demonstrate that the framework developed for effectively managing errors on near-term quantum computers makes achieving the target benchmark of chemical accuracy possible by using the emulator of a near-term commercial quantum computing device. The benchmark also demanded that the precision be within chemical accuracy and the estimated precision is well within that target indicating that the benchmark is reproducible.

Chapter 2

Technical Background

Quantum computing is a paradigm of computation that makes use of quantum mechanics for manipulation of quantum information. The fundamental properties defining this paradigm are superposition, entanglement and interference. As in classical computation, the unit of information is defined in terms of bits and in quantum computing they are known as quantum bits or qubits, a term coined by Benjamin Schumacher and W.K. Wootters Schumacher (1995). While bits in classical computation can take values of 0 and 1 depending on the voltage of the transistor, qubits can be in states $|0\rangle$ and $|1\rangle$. They can also be in states known as *superposition*, which are a linear combination of states. An example of a state in superposition is shown in equation 2.1.

$$|\psi\rangle = \alpha|0\rangle + \beta|1\rangle \tag{2.1}$$

A qubit can be defined by any isolated two-level quantum mechanical system. For instance, in the case of an atom or ion with sufficient energy difference between the ground state and the first excited state, the bit 0 can be represented by the ground state and the bit 1 can be represented by the first excited state. They are defined and governed by the postulates of quantum mechanics which are discussed below for qubits but are generally applicable to all quantum systems Nielsen and Chuang (2010a).

The first postulate states that a qubit, $|\psi\rangle$, is mathematically represented by a unit vector, known as a state vector, in a two-dimensional complex vector space known as the Hilbert space, $\mathcal{H}$, with an inner product. The complete information about the state of the qubit is given by the state vector typically represented using the braket notation with $|\psi\rangle$ as the ket, and $\langle\psi|$, the dual vector bra to the ket $|\psi\rangle$. The basis states, $|0\rangle$ or $|1\rangle$, also known as computational basis states, represent unit vectors $\begin{pmatrix}1\\0\end{pmatrix}$ and $\begin{pmatrix}0\\1\end{pmatrix}$, respectively. As mentioned above, the superposition is represented as a linear combination of states such as $\alpha|0\rangle \pm \beta|1\rangle$, where α and β are complex numbers and $|\alpha|^2$ and $|\beta|^2$ are the probabilities of measuring the qubit in the $|0\rangle$ and $|1\rangle$ state. Since the total probability must equal 1, $|\alpha|^2 + |\beta|^2 = 1$. The states are normalized such that $\langle\psi|\psi\rangle = 1$, where $\langle\psi|\psi\rangle$ is the inner product.

The second postulate provides the description of the evolution of an isolated quantum system. The transformation of the state of an isolated quantum system or a qubit from $|\psi_1\rangle$ to $|\psi_2\rangle$ is described by a unitary operation U, such that $UU^\dagger = U^\dagger U = \mathbb{I}$. The evolution of an isolated quantum system over time, t, is given by the Schrödinger equation:

$$i\hbar\frac{\partial|\psi\rangle}{\partial t} = H(t)|\psi\rangle \tag{2.2}$$

where $\hbar$ is the Planck's constant, i is the imaginary number, and H is the Hamiltonian operator which completely describes the dynamics of the system under evolution.

Some of the commonly used single qubit operators in quantum computing are the Pauli operators shown below,

$$X = \begin{pmatrix}0 & 1\\1 & 0\end{pmatrix}, \quad Y = \begin{pmatrix}0 & -i\\i & 0\end{pmatrix}, \quad \text{and} \quad Z = \begin{pmatrix}1 & 0\\0 & -1\end{pmatrix} \tag{2.3}$$

which satisfy the commutation relation $[X, Y] = -2iZ$ and where X is a bit-flip operator, Z a phase-flip operator and Y is a bit- and a phase-flip operator. Another important operator is the Hadamard operator

$$H = \frac{1}{\sqrt{2}} \begin{pmatrix} 1 & 1 \\ 1 & -1 \end{pmatrix} \tag{2.4}$$

which is commonly used to generate a superposition, such as $H|0\rangle = \frac{1}{\sqrt{2}}(|0\rangle + |1\rangle)$. An example of a two-qubit operator is the $CNOT$, or the controlled-NOT operation

$$CNOT = \begin{pmatrix} 1 & 0 & 0 & 0 \\ 0 & 1 & 0 & 0 \\ 0 & 0 & 0 & 1 \\ 0 & 0 & 1 & 0 \end{pmatrix} \tag{2.5}$$

where the state of the target qubit undergoes a bit-flip or remains unchanged depending on whether the state of the control qubit is $|1\rangle$ or $|0\rangle$, respectively.

The third postulate describes the process and outcome of measurement of quantum systems. Measurement of any observable attribute of a quantum system, in this case, a qubit, results in an outcome that is equal to eigenvalues of the observable. Quantum measurement is described by a set of projection operators so named because they project the state into an eigenstate of the observable being measured immediately after the measurement. The projection operators for an observable A w.r.t a quantum state are given by:

$$A = \sum_m a_m A_m \tag{2.6}$$

where A_m projects the state into the corresponding eigenstate of A with eigenvalue a_m. Additionally, the operators A_m project the state into mutually orthogonal eigenstates of the observable and therefore, $A_m A_{m'} = \delta_{mm'} A_m$. The probability of measuring a particular eigenvalue a_m is given by:

$$p(a_m) = \langle\psi|A_m|\psi\rangle \tag{2.7}$$

Following the measurement the state is projected into the eigenstate:

$$|\psi_{a_m}\rangle = \frac{A_m|\psi\rangle}{\sqrt{\langle\psi|A_m|\psi\rangle}} \tag{2.8}$$

Conservation of probability requires that the set of measurement operators for an observable follow the completeness relation:

$$\sum_m A_m = \mathbb{I} \tag{2.9}$$

In the case of $|\psi\rangle = \alpha|0\rangle + \beta|1\rangle$, the probability of measuring the state $|0\rangle$ is given as $p(|0\rangle) = |\alpha|^2$ and the state after measurement would be $|\psi_0\rangle = |0\rangle$. The possible measurement operators for this state are given by the set $\{|0\rangle\langle 0|, |1\rangle\langle 1|\}$ where the notation $|\psi\rangle\langle\psi|$ represents the outer product. The states $|0\rangle$ and $|1\rangle$ are referred to as the computational basis states in quantum computing and the measurement in this basis is known as the computational basis measurement. Measuring a state in a different basis requires the transformation of the basis of the quantum state followed by measurement in the computational basis.

The average value of the measurement of observable A is given by:

$$\begin{aligned}\mathbb{E}(A) &= \sum_m a_m p(a_m) \\ &= \sum_m a_m \langle\psi|A_m|\psi\rangle \\ &= \langle\psi|\sum_m a_m A_m|\psi\rangle \\ &= \langle\psi|A|\psi\rangle\end{aligned} \tag{2.10}$$

and is known as the expectation value of A. The standard deviation is given by:

$$\Delta A = \sqrt{\langle A^2 \rangle - \langle A \rangle^2} \tag{2.11}$$

Eigenvalues of a measurement must be real and operators with real eigenvalues are Hermitian, i.e., an operator is Hermitian if $A = A^\dagger$. As a result, observables and measurement operators of a qubit or quantum system must be Hermitian. The Hamiltonian **H** is therefore, a Hermitian and unitary operator.

The fourth postulate describes systems of multiple qubits. Composite systems comprising multiple qubits, $|q_0\rangle, |q_1\rangle ... |q_n\rangle$ without entanglement, each in its own Hilbert space $\mathcal{H}_i$ for $i \in [0...n]$ are described by tensor product of the individual qubits as shown in equation 2.12 within the accordingly combined Hilbert space, $\mathcal{H}_0 \otimes \mathcal{H}_1 .. \otimes \mathcal{H}_n$

$$|q_0 q_1 ... q_n\rangle = |q_0\rangle \otimes |q_1\rangle \otimes ... \otimes |q_n\rangle \tag{2.12}$$

Composite systems of qubits that are entangled are represented by states that are not separable into product states shown in equation 2.12. An instance of such an entangling operation, the two-qubit $CNOT$ operation, was described earlier. The two qubit state shown in 2.13 is the simplest example of an entangled state and is known as the Bell state.

$$|\psi\rangle = \frac{1}{\sqrt{2}}(|0_0\rangle \otimes |0_1\rangle + |1_0\rangle \otimes |1_1\rangle) = \frac{1}{\sqrt{2}}(|0_0 0_1\rangle + |1_0 1_1\rangle) \tag{2.13}$$

Entanglement in quantum systems is tested using the CHSH inequality derived from the more general Bell's inequality developed by John Stuart Bell Bell (1964); Clauser et al. (1969). Bell's theorem demonstrated that the measurement statistics generated by entangled quantum systems violated Bell's inequality and cannot be explained by local hidden variables or local realism, which is the theory that the measurement outcome of a system is predetermined (reality) and only influenced by the immediate vicinity of the system (locality) Einstein et al. (1935); Bohm (1952).

Experiments with entangled quantum systems have demonstrated violation of Bell's inequality Aspect et al. (1982); Hensen et al. (2015). They have shown that measurement of a quantum system, A, entangled with another system B influences the measurement outcome of B even if the systems are spatially separated, i.e., not in the immediate vicinity of each other, and that the measurement outcome of a quantum system is entirely determined by measurement alone and is not predetermined by any hidden variables. Together they indicate that either the assumption of locality or realism or both are incorrect assumptions with respect to quantum systems.

An alternate representation of quantum systems uses the density operator formalism, which is used to describe ensembles of pure quantum states $\{p_i, |\psi_i\rangle\}$ where p_i is the probability of measuring the state $|\psi_i\rangle$. A density operator, $\rho = \sum_i p_i |\psi_i\rangle\langle\psi_i|$ must have $\mathrm{Tr}(\rho) = 1$ to conserve probability and must be a positive operator. The same postulates described for the state vector apply here and can be used to describe the density operator. Additionally, a density operator can represent states that cannot be described using the state vector formalism above, such as mixed states. A *mixed state* is different from a *pure state* in that the pure state is normalized. This leads to the condition that differentiates between the two types of states. $\mathrm{Tr}(\rho^2) < 1$ for a mixed state and $\mathrm{Tr}(\rho^2) = 1$ for a pure state. This formalism is particularly useful when describing noise in quantum systems.

2.1 Noise Channels

As described earlier, qubits are, ideally, described by any isolated two-level quantum system. However, no system can be completely isolated from the environment and quantum systems are no exception. In quantum computing, interactions with the environment, neighboring qubits, and control systems that apply gate operations on qubits can lead to unintended corruption of information encoded on the qubits. These effects on quantum systems are described by quantum noise.

Quantum noise is described in quantum information and computation by the channel description used in classical communication. In classical communication systems, channels are used to describe the medium of information transmission and the effect of various types of noise on corrupting information during transmission is described by noise channels. In quantum computing, noise channels are used to describe effects of noise during information processing from initialization or state preparation of qubits to output or measurement. More concretely, the effect of noise is described by a map or quantum operator, $\mathcal{E}$ that maps an initial density operator ρ to another density operator, $\rho' = \mathcal{E}(\rho)$. The necessity that the output of the operation must also be a density operator imposes the constraint that it must be a completely positive trace preserving operator (CPTP).

A CPTP map has the following properties:

- The operator $\mathcal{E}$ must be trace preserving, i.e., $Tr(\rho) = Tr(\mathcal{E}(\rho)) = 1$
- The operator must be linear, such that for an ensemble of density operators, $\rho = \sum_i p_i |\psi_i\rangle\langle\psi_i| = \sum_i p_i \rho_i$, $\mathcal{E}(\rho) = \mathcal{E}(\sum p_i \rho_i) = \sum_i p_i \mathcal{E}(\rho_i)$
- Since density operators are positive, the operator $\mathcal{E}(\rho)$ must be a positive map, i.e, have non-negative eigenvalues.
- Finally, the operator must be completely positive. This means that if the operator acts on a density operator ρ_A in Hilbert space $\mathcal{H}_A$ of a combined system ρ_{AB} with the identity map , $\mathcal{I}$, acting on system ρ_B in Hilbert space $\mathcal{H}_B$ of arbitrary dimension, then the map $(\mathcal{E} \otimes \mathcal{I}_B)(\rho_{AB})$ must also be positive.

The noise channel description is used to model different types of quantum noise such as bit-flip, phase-flip, depolarizing, phase damping and amplitude damping channels. In this thesis, the standard isotropic depolarizing noise channel is used for modeling noise in the numerical simulations. The channel is described for a single qubit in equation 2.14 with the probability p that the qubit is in a completely mixed state and $1 - p$ that the state of the qubit is unaffected by noise.

$$\mathcal{E}(\rho) = (1-p)\rho + p\frac{\mathbb{I}}{2} \tag{2.14}$$

where ρ is a single qubit density matrix. For a composite system of multiple qubits, as in the case of the circuits used in this thesis, the noise model is constructed such that the effect of noise on each qubit is independent or uncorrelated. The model to describe noise affecting n qubits independently is given by:

$$\mathcal{E}^{\otimes n}(\rho) = (1-p)^n\rho + \sum_{i=1}^{n}\sum_{j=1}^{3}(1-p)^{n-1}\frac{p}{r}\sigma_j^i\rho\sigma_j^i + ... \tag{2.15}$$

where the equation continues with higher order terms and σ_j^i for $j \in \{X, Y, Z\}$ is the Pauli operator on qubit i.

How similar or different the output density operator is after noisy computation or noisy numerical simulations can be quantified with distance measures. One common measure for quantum states is the fidelity which can be used to quantify the accuracy of a given noisy state compared to the ideal noiseless state and is given by:

$$F = \sqrt{\sqrt{\rho}\rho'\sqrt{\rho}} \tag{2.16}$$

where ρ is the ideal state and $\rho' = \mathcal{E}(\rho)$ is the noisy state.

2.2 Quantum Chemistry

The central problem of electronic structure theory is to find the ground state of a molecule by finding the lowest eigenvalue of the electronic Hamiltonian. We start with the molecular Hamiltonian in first quantized form:

$$\hat{H}_{\text{mol}} = -\sum_i \frac{\nabla^2_{R_i}}{2M_i} - \sum_i \frac{\nabla^2_{r_i}}{2m_i} - \sum_{i,j}\frac{Z_i}{|R_i - r_j|} + \sum_{i,j>i}\frac{Z_iZ_j}{|R_i - R_j|} + \sum_{i,j>i}\frac{1}{|r_i - r_j|} \tag{2.17}$$

where R_i and r_i are the positions of the ith nuclei and electron, respectively, M_i, m_i their respective masses and Z_i the charge of the nuclei. Under the Born-Oppenheimer approximation, the nuclei are treated as classical point charges due to the large difference in mass between the nucleus and electron. This leads to an electronic Hamiltonian with coefficients that are a function of the internuclear geometry, R and is represented in the second quantized form, with N occupied or unoccupied spin orbitals, as:

$$H(R) = \sum_{pq} h_{pq} a_p^\dagger a_q + \frac{1}{2} \sum_{pqrs} h_{pqrs} a_p^\dagger a_q^\dagger a_r a_s \tag{2.18}$$

where the one-electron integrals

$$h_{pq}(R) = \int d\sigma \varphi_p^*(\sigma) \left(\frac{\nabla_r^2}{2} - \sum_i \frac{Z_i}{|R_i - r|} \right) \varphi_q(\sigma) \tag{2.19}$$

and two-electron integrals

$$h_{pqrs} = \int d\sigma_1 d\sigma_2 \frac{\varphi_p^*(\sigma_1)\varphi_q^*(\sigma_2)\varphi_s(\sigma_1)\varphi_r(\sigma_2)}{|r_1 - r_2|} \tag{2.20}$$

are taken with respect to the variable $\sigma_i = (r_i, s_i)$ denoting both spin s_i and position r_i and depend on the nuclear coordinates R. The associated fermionic creation and annihilation operators satisfy the anti-commutation relations

$$\{a_p^\dagger, a_q\} = \delta_{p,q} \qquad \text{and} \qquad \{a_p, a_q\} = 0 \tag{2.21}$$

where operator $a_p^\dagger$ (a_p) creates (annihilates) an electron from the pth spin orbital.

The electronic Hamiltonian in (2.18) may be transformed into a qubit representation using the usual Pauli operators in the computational basis shown in equation 2.3. Several transformations into the qubit representation are known to satisfy the necessary fermionic commutation relations. For most of the studies in this thesis, we employ the Jordan-Wigner transformation and for the last two chapters we use a slightly modified transformation which is presented in the appendix of chapter 5 Jordan and Wigner (1928); Shee et al. (2022). The Jordan-Wigner transform is defined as

$$a_p^\dagger = \otimes_{i<p} Z_i \otimes \sigma_p^-, \quad \text{and} \quad a_p = \otimes_{i<p} Z_i \otimes \sigma_p^+ \tag{2.22}$$

in terms of the qubit raising and lower operations $\sigma_p^\pm = (X_p \pm iY_p)/\sqrt{2}$ where the p-th spin orbital is represented by the p-th qubit. The implementation of this transformation requires $n \geq N$ qubits, and the resulting representation of the electronic Hamiltonian is

$$H(R) = \sum_j c_j(R) P_j \tag{2.23}$$

where $c_j(R)$ is the corresponding coefficient which can be efficiently computed on a classical computer from equations 2.19 and 2.20 and $P_j = \bigotimes_i \sigma_j^i$ denotes the j-th string or tensor product of Pauli operators $\sigma \in \{X, Y, Z\}$ acting on the i-th qubit. The maximum number of terms in (2.23) is 4^n but, in practice, symmetries within the Hamiltonian significantly reduce the number of terms that have non-zero coefficients (Romero et al., 2018a). On average the number of terms in this reduced Hamiltonian scale as $O(N^4)$ where N is the number of spin orbitals McArdle et al. (2020); Shee et al. (2022).

2.3 Variational Quantum Eigensolver

The variational quantum eigensolver (VQE) method estimates the minimal expectation value of a Hermitian operator with respect to a variable quantum circuit using a quantum computer Peruzzo et al. (2014a). The method relies on the variational principle from quantum mechanics, which states that only the lowest eigenstate of a non-negative operator can minimize the expectation value. Here, we use the qubit representation of the electronic Hamiltonian as the operator of interest, such that the estimated energy expectation value is

$$E(R;\theta^{\star}) = \min_{\theta} \langle \psi(\theta)|H(R)|\psi(\theta)\rangle \tag{2.24}$$

where $|\psi(\theta)\rangle = U(\theta)|\psi(0)\rangle$ is a variable pure quantum state prepared by a (unitary) ansatz operator $U(\theta)$. The parameter $\theta^{\star}$ denotes the optimal value that minimizes the energy, and a generalization of θ may include multiple parameters within the ansatz. $H(R)$ is the Hamiltonian as described in equation 2.23. The expectation value of the Hamiltonian is calculated by finite sampling of the individual Pauli terms from the probability distribution determined by the prepared ansatz state. The expectation values of the Pauli terms are calculated from these measurements which are then summed to calculate the expectation value of the Hamiltonian as shown in 2.25. This is known as Hamiltonian averaging.Aspuru-Guzik et al. (2005); McClean et al. (2014, 2016a).

$$\langle H(\theta)\rangle = \sum_{j} c_j \langle P_j(\theta)\rangle \tag{2.25}$$

Measurements of an observable of a quantum system gives the probability of measuring the eigenvalues of the observable as shown in 2.7. Finite sampling of observables of the Hamiltonian result in expectation values that equal the probability of measuring the observable in the limit of infinite samples. Numerical simulations of measurements in the infinite sampling limit are represented by state vector simulations.

Benchmarking the computational accuracy of the device includes calculating the uncertainty in the measurements. For the case of finite sampling of observables and evaluating the precision of the calculation with respect to chemical accuracy, we calculate the standard error of the mean from the variance of the ansatz with respect to the Hamiltonian at the optimal parameter. The variance is calculated as

$$\begin{aligned} var &= \sum_i g_i^2(\langle P_i^2\rangle - \langle P_i\rangle^2) \\ &= \sum_i g_i^2(1 - \langle P_i\rangle^2) \end{aligned} \tag{2.26}$$

where P_i is the ith Pauli term of the Hamiltonian and g_i is the coefficient of the ith Pauli term. The standard error $\sigma_{E(\theta^*)}$ is derived from the variance:

$$\sigma_{E(\theta^*)} = \sqrt{\frac{var}{N}} \tag{2.27}$$

where N is the number of shots or samples and var is the variance of the calculation. From these we calculate the number of samples required to calculate energy within chemical accuracy in the noiseless case:

$$N = \frac{var}{\sigma^2_{E(\theta^*)}} \tag{2.28}$$

The critical choice in applying the VQE method to a given Hamiltonian is selection of the ansatz operator $U(\theta)$ and the underlying reference state $\psi(0)$. The latter may be selected by using conventional approximations to the electronic ground state that are efficiently encoded as superpositions of binary states. For example, using the Hartree-Fock solution to the electronic Hamiltonian offers a convenient choice for the reference state, and the vacancy or occupation of a molecular orbital may be encoded by 0 or 1, respectively Romero et al. (2018b); Peruzzo et al. (2014a).The choice of the ansatz operator plays a significant role in determining the accuracy of the energy estimate Grimsley et al. (2019a); McCaskey et al. (2019); Google AI Quantum et al. (2020). The greater the overlap of the prepared state with the ground state of the Hamiltonian, the greater the accuracy of the ground state energy. The ansatz operator may be drawn from conventional electronic structure theory, and many recent efforts have focused on unitary coupled cluster (UCC) theory to generate possible choices for the ansatz operator (Romero et al., 2018a; Sokolov et al., 2020a).

For all the studies in this dissertation, we consider an ansatz based on UCC theory which derives from the well known coupled cluster methods in quantum chemistry (Romero et al., 2018b; Bartlett et al., 1989; Taube and Bartlett, 2006). To derive the UCC ansatz, we start by replacing operators from classical coupled cluster theory with unitary excitation operators. This results in an exponentiated sum of operators

$$\begin{aligned} U(\theta) &= e^{T(\theta)-T(\theta)^\dagger} \\ T(\theta) &= \sum_k T_K(\theta) \\ T_1 &= \sum_{q\in occ, p\in virt} \theta_q^p a_p^\dagger a_q \\ T_2 &= \sum_{r>s\in occ, p>q\in virt} \theta_{rs}^{pq} a_p^\dagger a_q^\dagger a_r a_s \end{aligned} \tag{2.29}$$

where T_k is the excitation operator manifold and θ_q^p and θ_{rs}^{pq} are singles and doubles amplitudes, respectively. This operator can be approximated as a product of exponentiated operators using Trotterization resulting in a unitary coupled cluster operator (Suzuki, 1993; Trotter, 1959; Evangelista et al., 2019). The unitary operator approximated to the first Trotter step ($t = 1$) is shown in equation 2.30.

$$\begin{aligned} U(\theta) &= e^{\sum_i \theta_i(\tau_i - \tau_i^\dagger)} \\ &\approx \Big(\prod_i e^{\frac{\theta_i}{t}(\tau_i - \tau_i^\dagger)}\Big)^t \\ &\approx \prod_i e^{\theta_i(\tau_i - \tau_i^\dagger)} \end{aligned} \tag{2.30}$$

where,

$$\tau_j - \tau_j^\dagger = i\sum_j a_j P_j \tag{2.31}$$

is the transformation from fermionic representation shown in equation 2.29 to qubit representation, $P_j = \bigotimes_i \sigma_j^i$ denotes the j-th string or tensor product of Pauli operators $\sigma \in \{X, Y, Z\}$ acting on the i-th qubit and $a_j \in \mathbb{R}$ is a scalar resulting from the fermion-to-qubit transformation. The operator is transformed to the qubit representation using the same mappings mentioned earlier in the case of transforming the electronic Hamiltonian to the qubit representation.

2.4 Error Detection

The error detection codes employed for mitigating different sources of errors in hardware are discussed in this section. Quantum error detection is a technique to encode information in such a way as to enable detection of errors with the help of specific measurements known as syndrome measurements Devitt et al. (2013). The technique follows the structure of quantum error correction codes, but without the ability to correct errors due to absence of information about the location of the error. Quantum error correction encodes information redundantly by using multiple physical qubits to encode a logical qubit. Computation using an encoded qubit involves the subsequent and repeated process of detection and decoding of errors followed by recovery operations throughout the course of the computation. Quantum error detection stops at the detection process and uses post-selection to improve accuracy of the outcomes. Detection of errors involve ancillary qubits or ancillas that are entangled with the encoded data qubits to extract information about the error or syndrome without destructively measuring the data qubits. The syndrome measurement circuits are defined for each code and for type of error, bit or phase flip. The codewords of a code define the corresponding logical computational basis state in terms of the physical qubits, and consequently, the logical operations are defined by the corresponding physical qubit operations that transform the state from one logical basis state to another. The code distance, also known as the Hamming distance, is defined as the number of bit-flips that takes a logical $|0\rangle$ state to the logical $|1\rangle$ state.

2.4.1 [[4,2,2]] Quantum Error Detection Code

The [[4,2,2]] quantum error detection code, following the $[[n, k, d]]$ convention, is a distance $d = 2$ code that encodes $k = 2$ logical qubits using $n = 4$ physical qubits. The basis states for the logical codespace of this encoding are shown in equations 2.33 and the corresponding physical operations for each logical operation are described in **Table 2.1**. The $SWAP_{12}$ operation swaps the state of two qubits $(|q_1\rangle, |q_2\rangle)$ and is defined as:

$$SWAP_{12} = \begin{pmatrix} 1 & 0 & 0 & 0 \\ 0 & 0 & 1 & 0 \\ 0 & 1 & 0 & 0 \\ 0 & 0 & 0 & 1 \end{pmatrix} \tag{2.32}$$

$$\begin{aligned} \overline{|00\rangle} &= \frac{1}{\sqrt{2}}(|0000\rangle + |1111\rangle) \\ \overline{|10\rangle} &= \frac{1}{\sqrt{2}}(|0101\rangle + |1010\rangle) \\ \overline{|01\rangle} &= \frac{1}{\sqrt{2}}(|0011\rangle + |1100\rangle) \\ \overline{|11\rangle} &= \frac{1}{\sqrt{2}}(|0110\rangle + |1001\rangle) \end{aligned} \tag{2.33}$$

The code can detect at most one-single physical qubit bit flip and phase flip error (Pauli X and Z error, respectively) that occurs during the encoding of the initial state (Devitt et al., 2013). The circuit for the error detection or syndrome measurement for this encoding is presented in **Figure 2.1**. Ancillas s_X and s_Z are used for error syndrome measurement and detect bit flip and phase flip errors, respectively.

Table 2.1: Basis operations.

Basis Operations	
Logical Basis	Physical Basis
$X_1 \otimes I_2$	$X \otimes I \otimes X \otimes I$
$I_1 \otimes X_2$	$X \otimes X \otimes I \otimes I$
$Z_1 \otimes I_2$	$Z \otimes Z \otimes I \otimes I$
$I_1 \otimes Z_2$	$Z \otimes I \otimes Z \otimes I$
$H_1 \otimes H_2$	$H \otimes H \otimes H \otimes H$
$CNOT_{12}$	$SWAP_{12}$
$CNOT_{21}$	$SWAP_{13}$

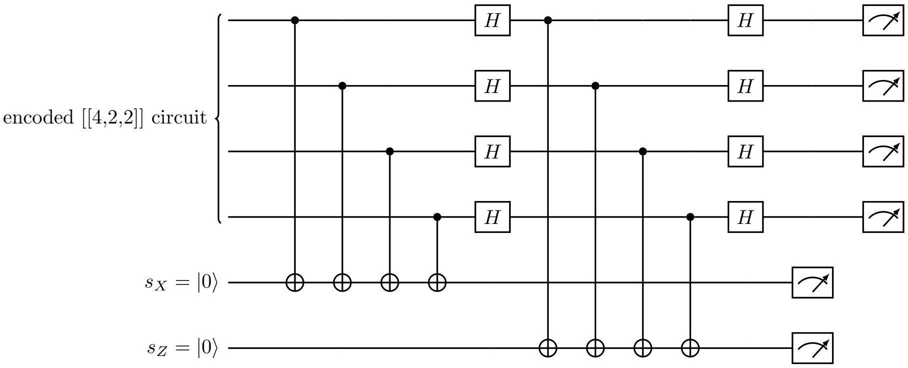

Figure 2.1: Syndrome measurement circuit for the [[4,2,2]] error detection code.

Since all the basis states of this encoding have even parity (even number of 1s in the physical basis), any single physical qubit bit flip error will take the state outside the logical codespace and result in a state with odd parity. As a result, a single physical qubit bit flip error will lead to a measurement of $s_X = 1$. If the state is rotated using the Hadamard ($H^{\otimes 4}$) operation before measurement, any single physical qubit phase flip error will lead to a measurement of $s_Z = 1$. Two physical qubit bit-flip errors take the state to another logical state and will remain undetected by the ancillas. Two physical qubit phase-flip errors can add a global phase to the state or leave the state effectively unchanged.

Since the error detection depends on parity of the physical qubits, the error syndrome can be extracted in another way. Upon measurement of all qubits, they can be post-selected based on parity. Odd parity measurements indicate that a single qubit bit-flip error has occurred and is akin to performing the stabilizer measurement with ancilla s_X in **Figure 2.1**. Similarly, odd parity of measurements made after rotating the state by applying the Hadamard ($H^{\otimes 4}$) operation indicate that a physical qubit phase-flip error has occurred and is equivalent to an $s_Z = 1$ measurement in **Figure 2.1**. The advantage of this method over the stabilizer measurement is the reduction in the number of two-qubit gates for syndrome detection. The disadvantage is that the detection of errors requires a destructive measurement and only allows detection of one of the two types of errors, a physical bit flip or phase flip error.

2.4.2 Read Out Error Detection

This method is part of the proposed research for the dissertation. Currently, the dominant source of error in a quantum computer is read out error or measurement error. While, the [[4,2,2]] QED code is to enable detection of errors occurring during the execution of the circuit, the outcome is not protected against errors during measurement. In order to mitigate read out errors while using the a QED code for protecting the circuit, we propose to use a read out error detection code.

The two qubit repetition code can be used for mitigating read out error Hicks et al. (2022). The three-qubit quantum repetition code is an error correction code that encodes a logical qubit into three physical qubits with distance $d = 3$ Devitt et al. (2013). The codewords in the computational basis for the bit-flip repetition code are shown in equation 2.34. A quantum error correction code can correct at most $t = \frac{d-1}{2}$ errors and for this code, $t = 1$. The three qubit repetition code can correct at most one single qubit bit- or a phase-flip error depending on the basis of the encoding. The codewords in the computational basis for the bit-flip repetition code are shown in equation 2.34. A phase-flip error in this encoding will remain undetected. A bit-flip error on one physical qubit such as $|000\rangle \rightarrow |001\rangle$ can be corrected, however, a bit-flip error on more than one physical qubit such as $|000\rangle \rightarrow |011\rangle$ will be detected as a bit-flip error on the left-most qubit and lead to incorrect decoding and correction. As a result the encoding is successful in protecting against one type of error, a bit or phase-flip error, provided only one single physical qubit error, and one type of error occurs per logical qubit.

$$\begin{aligned} |\bar{0}\rangle &= |0\rangle^{\otimes 3} \\ |\bar{1}\rangle &= |1\rangle^{\otimes 3} \end{aligned} \tag{2.34}$$

Since read out error involves only one type of error, a bit flip error, the bit-flip repetition code can be employed for protecting against read out errors. However, since the error rate on near-term quantum computers does not guarantee occurrence of at a most a single physical qubit error per logical qubit during measurement, the code is used only for error detection to minimize introducing errors greater than single physical qubit errors. The code encodes the data qubits just prior to measurement in a two qubit repetition code which we refer to as the read out error detection code. The data qubits $|q_i\rangle$ are encoded by entangling each of them with another qubit $|r_i\rangle$ just prior to measurement as shown in **Figure 2.2** for a circuit representing the preparation of a bell state. The codewords for this encoding are shown in equation 2.35.

$$
\begin{aligned}
|\bar{0}\rangle &= |00\rangle \\
|\bar{1}\rangle &= |11\rangle
\end{aligned}
\tag{2.35}
$$

The data qubits q_0, q_1 are redundantly encoded using qubits r_0, r_1. In the noiseless case, the qubits r_0, r_1 would be measured in the same state as the data qubits q_0, q_1 they are entangled with, respectively. Measurement differences between the data and encoded qubits such as $|q_0 r_0\rangle = |01\rangle$ indicate an error has occurred on one of the qubits and therefore, measurements with odd parity are discarded. Even parity measurements indicate either no error has occurred or an error has occurred on both qubits. Since the latter cannot be detected by the code, even parity measurements, such as $|q_0 r_0\rangle = |11\rangle$, are retained. The success of the code depends on the difference in magnitude of error rates between the two-qubit gate error and read out error. Having a much lower two-qubit gate error rate than read out error will lead to higher accuracy in the post-selected measurements.

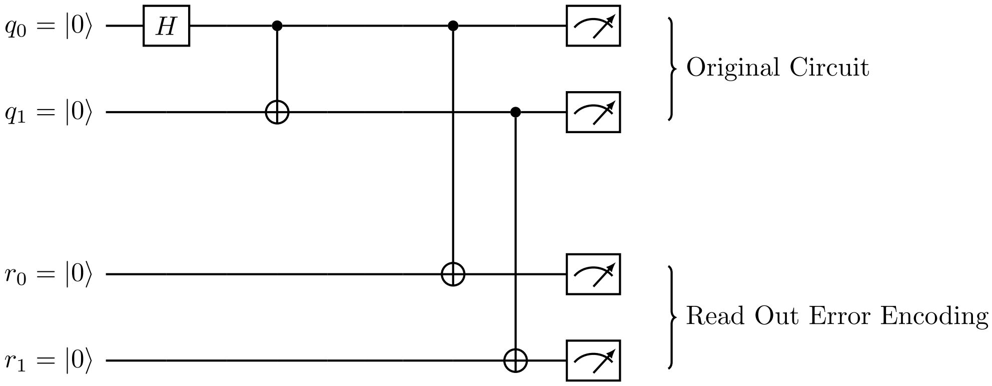

Figure 2.2: Encoding qubits with read out error detection code

2.5 Numerical Simulations

We use the XACC framework to run the numerical simulations of the VQE algorithm. XACC is a software framework developed at Oak Ridge National Lab (ORNL) for the development of hardware-agnostic programs for quantum-classical hybrid algorithms, and their implementation on near-term quantum hardware (McCaskey et al., 2020; Daniel et al., 2022) . We use the IBM Aer simulator within XACC for numerically simulating each ansatz and use brute force optimization by scanning 150 values of parameter $\theta \in [-\pi, \pi]$.

We model gate noise with a depolarizing error channel given as

$$\xi_j^G(\rho) = (1-p)\rho' + p \sum_k \sigma_j^k \rho' \sigma_j^k \tag{2.36}$$

where $\rho' = G\rho G^\dagger$, G is any single-qubit gate in the circuit acting on qubit j in density matrix ρ, $\sigma_j \in \{X_j, Y_j, Z_j\}$, and p is the noise parameter. Errors on a two-qubit gate acting on qubits i and j are modeled as $\xi_{i,j}^G(\rho) = \xi_i^I(\xi_j^G(\rho))$ with I the identity. The noise parameter for the two-qubit gate is an order of magnitude higher than the single-qubit noise parameter as is typical in current devices. The errors resulting from this channel are single qubit errors, E_j on qubit j or two qubit errors $E_i \otimes E_j$ on qubits, i and j for $E_k \in \{X_k, Y_k, Z_k, \mathbb{I}_k\}$.

Chapter 3

Numerical Simulations of Noisy Variational Quantum Eigensolver Ansatz Circuits

We investigate a computational chemistry application of the variational quantum eigensolver (VQE) algorithm to calculate the electronic ground state and its energy for Sodium Hydride (NaH), a prototypical two-electron problem, to test the influence of noise on the accuracy of the underlying circuit ansatz. Using a one-parameter ansatz derived from unitary coupled cluster (UCC) theory, we simulate the effects of noise on the energy expectation value and variance with respect to the ansatz parameter. These numerical simulations provide insights into the accuracy of the prepared quantum state and the efficiency of the classical optimizer that iteratively refines the ansatz. We conduct a comparative study between analytical results derived for the UCC ansatz in the absence of noise and the noisy numerical simulation results obtained using an isotropic depolarizing noise model for each gate. We also compare the relative increase in noise on logically equivalent UCC ansatz circuits generated by randomized compiling. Notably, we observe that the intrinsic variance in the energy due to the simplicity of the ansatz itself compares with the noise induced by the bare circuit.

3.1 Introduction

Testing and evaluation of noisy intermediate-scale quantum (NISQ) devices provides insights into the versatility and performance of near-term quantum computing (McCaskey et al., 2019; Claudino et al., 2020; Arute et al., 2020; Urbanek et al., 2020a; Yeter-Aydeniz et al., 2021). Variational algorithms have emerged as a promising approach to mitigate the non-ideal gate and circuit executions observed with NISQ devices (Peruzzo et al., 2014b). By tuning the circuit parameters, variational methods permit optimization of performance in the presence of ill-defined sources of noise. However, there are open questions about the efficacy of variational methods to mitigate against the loss of accuracy that accompanies noisy evaluation. While parameter tuning may provide a better estimate, it is unclear when the observed result is representative of the true solution (Claudino et al., 2020). Within the context of variational methods for quantum chemistry, these concerns become a statement about the fidelity of the prepared state relative to the correct solution state.

Previously, Claudino et al. investigated the trade-off in fidelity and energy accuracy for several variational quantum eigensolver methods in the absence of noise (Claudino et al., 2020). Their approach used noiseless numerical simulations to estimate the fidelity by which various ansatz circuits for VQE methods, including ADAPT-VQE (Grimsley et al., 2019b), prepare the correct solution state for small hydrogen-like molecules. Given sufficient iterations in tuning the circuit parameters, highly accurate energy estimates and state preparations were observed relative to the full-configuration interaction (FCI) results obtained by conventional computational chemistry packages. However, those studies did not consider the influence of noise on ansatz circuit or the parameter optimizer.

Here we extend those noiseless baseline results of the variational quantum eigensolver (VQE) method by using numerical simulation to test the influence of noise on the accuracy of the underlying circuit ansatz. We consider the use of VQE to calculate the electronic ground state and energy of Sodium Hydride (NaH), reduced to a prototypical two-electron problem, using a one-parameter ansatz derived from unitary coupled cluster (UCC) theory. In the absence of noise, we derive an analytical expression for the prepared quantum state and the corresponding expectation value for each (Pauli string) term contributing to the total electronic energy. We then compare these expressions with the noisy numerical simulations of the same ansatz and quantify the accuracy with which the minimal energy state can be prepared.

We also compare these results with noisy numerical simulations of randomly compiled instances of the UCC circuit ansatz. Randomized compiling is a technique by which a circuit, or subcircuit, instance is transformed in gate structure but preserves logically equivalent output state (Wallman and Emerson, 2016a). The principle of this approach is to use randomized unitary transformations of a specified input circuit such that sampling the resulting ensemble leads to an averaging, or twirling, of the underlying hardware noise. This approach is designed to convert coherent and non-Markovian error sources into stochastic errors and, therefore, reduce the effects of correlated noise (Erhard et al., 2019; Hashim et al., 2020). Here we use an uncorrelated, stochastic noise model, i.e., isotropic depolarizing noise, which randomized compiling will not mitigate. Our purpose is to understand how much additional noise will accumulate within the randomly compiled circuits if coherent noise is absent.

3.2 Methods

The variational quantum eigensolver is a method for estimating the minimal expectation value of a specified operator with respect to a variable quantum circuit

(Peruzzo et al., 2014b). The method relies on the variational principle, which states that only the lowest eigenvalue state of a non-negative operator can minimize the expectation value. Here, we minimize the Hamiltonian operator H to yield the expectation value

$$E(r;\theta^{\star}) = \min_{\theta} \langle\psi(\theta)|H(r)|\psi(\theta)\rangle \tag{3.1}$$

where $|\psi(\theta)\rangle = U(\theta)|\psi(0)\rangle$ is the pure-state wavefunction prepared by the unitary ansatz operator $U(\theta)$, $\theta^{\star}$ denotes the optimal value, and r represents the inter-nuclear distance.

As reviewed elsewhere (Cao et al., 2019a), the molecular Hamiltonian may be reduced from a fermionic representation to spin representation. Here we reduce the two-electron Hamiltonian representing NaH within the frozen-core approximation to a four-spin problem using the Jordan-Wigner transformation following Ref. (McCaskey et al., 2019). In general, this energy depends on the inter-molecular distance r and yields a summation of 4^n Pauli strings

$$H(r) = \sum_{j} c_j(r) P_j \tag{3.2}$$

with $c_j(r)$ the real-valued coefficient that depends on the one- and two-electron integrals and corresponds to the j-th combination P_j of n Pauli operators. Here we use $n = 4$ qubits to encode two electrons, the STO-3G basis set, and a range of inter-nuclear distances, r, from 1.0 to 4.0 Å. The Hamiltonian for NaH then reduces to a decomposition of $J = 27$ non-trivial terms for each value of r, an example of which is presented in **Table 3.1** for a nominal value of $r = 1.91438$ Å(McCaskey et al., 2019).

We next motivate our ansatz circuit from unitary coupled cluster (UCC) theory, which provides a formal approach to generating the unitary operators that prepare an electronic ground state. By expanding to second order in the excitation operator,

Table 3.1: Four-spin representation of the two-electron, NaH Hamiltonian and expectation value of the Pauli strings with respect to the UCC1 ansatz for $r = 1.91438$Å.

j	$c_j(r_0)$ [Ha]	P_j	$\langle P_j(\theta)\rangle$
0	-159.40289	$I_0I_1I_2I_3$	1
1	0.0323625	$X_0X_1I_2I_3$	0
2	0.0202421	$X_0X_1X_2X_3$	$-\sin\theta$
3	0.0202421	$X_0X_1Y_2Y_3$	$-\sin\theta$
4	0.0229208	$X_0X_1Z_2I_3$	0
5	-0.00944179	$X_0X_1I_2Z_3$	0
6	0.0323625	$I_0I_1X_2X_3$	0
7	0.0323625	$Y_0Y_1I_2I_3$	0
8	0.0202421	$Y_0Y_1X_2X_3$	$-\sin\theta$
9	0.0202421	$Y_0Y_1Y_2Y_3$	$-\sin\theta$
10	0.0229208	$Y_0Y_1Z_2I_3$	0
11	-0.00944179	$Y_0Y_1I_2Z_3$	0
12	0.0323625	$I_0I_1Y_2Y_3$	0
13	0.0149385	$Z_0I_1I_2I_3$	$-\cos\theta$
14	0.0229208	$Z_0I_1X_2X_3$	0
15	0.0229208	$Z_0I_1Y_2Y_3$	0
16	0.0816923	$Z_0Z_1I_2I_3$	-1
17	0.158901	$Z_0I_1Z_2I_3$	1
18	0.101934	$Z_0I_1I_2Z_3$	-1
19	-0.387818	$I_0Z_1I_2I_3$	$-\cos\theta$
20	-0.00944179	$I_0Z_1X_2X_3$	0
21	-0.00944179	$I_0Z_1Y_2Y_3$	0
22	0.101934	$I_0Z_1Z_2I_3$	-1
23	0.117450	$I_0Z_1I_2Z_3$	1
24	0.0149385	$I_0I_1Z_2I_3$	$-\cos\theta$
25	0.0816923	$I_0I_1Z_2Z_3$	-1
26	-0.387818	$I_0I_1I_2Z_3$	$\cos\theta$

we define the one-parameter UCC ansatz, presented previously in Ref. (McCaskey et al., 2019) as UCC-1,

$$U(\theta) = e^{i\frac{\theta}{2}Y_0X_1X_2X_3} \tag{3.3}$$

This specific ansatz is capable of preparing doubly excited superposition states, but lacks the ability to match the electronic ground state available from more sophisticated full configuration interaction (FCI) methods. The corresponding circuit specification for this operator is given in **Figure 3.1**, where $Z(\theta) = \exp(-i\theta Z/2)$. We use the initial state $|\psi(0)\rangle = |1010\rangle$ as the Hartree-Fock reference state.

From this UCC-1 ansatz, we derive the expressions for the energy expectation value. We use analytical approaches based on the Schrodinger and Heisenberg representations to describe the evolution of the system. First, using the Heisenberg representation, we present the expectation value for each P_J as

$$\langle P_j(\theta)\rangle = \langle\psi(0)|U^{\dagger}(\theta)P_jU(\theta)|\psi(0)\rangle \tag{3.4}$$

with the results for each j shown in **Table 3.1**. The resulting expectation value for the Hamiltonian is then

$$\begin{aligned}\langle H(\theta)\rangle =& \sum_j c_j\langle P_j(\theta)\rangle \\ =& -159.494002 - 0.805512\cos(\theta) \\ & - 0.0809325\sin(\theta)\end{aligned} \tag{3.5}$$

We may similarly calculate the variance in the expectation value of the energy as

$$\begin{aligned}\langle(\Delta H(\theta))^2\rangle =& \sum_j c_j^2\langle(\Delta P_j(\theta)^2\rangle \\ =& 0.309498 - 0.301251\cos^2(\theta) \\ & - 0.00163752\sin^2(\theta)\end{aligned} \tag{3.6}$$

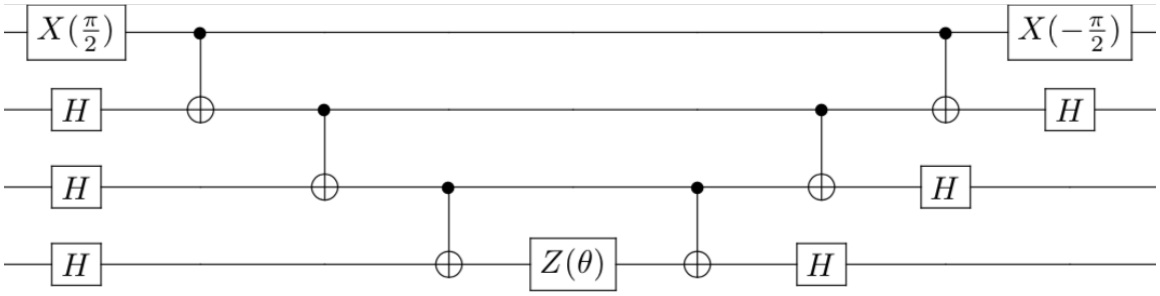

Figure 3.1: The circuit diagram describing the unitary coupled cluster ansatz used for these numerical studies.

where $\langle(\Delta P_j(\theta)^2\rangle = (1 - \langle P_j(\theta)\rangle^2)$ as $P_j^2 = 1$. We find from Eq. (3.5) that the energy reaches a minimum value of $\langle H(\theta^\star)\rangle = -160.3037$ Ha for the ansatz parameter $\theta^\star = 0.1001$ with a corresponding variance of $\langle(\Delta H(\theta^\star))^2\rangle = 0.011239$.

Secondly, using the Schrödinger representation, we use the circuit representation of the ansatz in **Figure 3.1** to derive the quantum computational state prepared after each gate operation. We find that upon completion of the UCC-1 circuit, the prepared noiseless quantum state is

$$|\psi(\theta)\rangle = \cos(\theta/2)|1010\rangle - \sin(\theta/2)|0101\rangle \tag{3.7}$$

which yields the same energy as above. As expected, this state corresponds to a superposition of the original Hartree-Fock reference state and the doubly excited state, but lacks the singly excited manifold needed to reproduce FCI results (Yeter-Aydeniz et al., 2021).

We use the known form of the state as a check for our numerical simulations of the circuit, for which we implement the VQE algorithm using the XACC programming framework (McCaskey et al., 2020). A listing from the program is shown in **Figure 3.2**, which highlights the use of the PySCF package to generate the molecular Hamiltonian using the frozen core basis with four active orbitals and the translation of this Hamiltonian using the XACC methods (Sun et al., 2018). We have verified the correctness of these programs using multiple numerical simulators supported within XACC and we present results below using the numerical simulator "aer" imported from the IBM Qiskit software package (Abraham et al., 2019). The aer simulator supports a matrix-based simulation of noiseless and noisy quantum states, and we have confirmed that simulations of the energy expectation value $E(\theta)$ and corresponding $\theta^\star$ found using brute force optimization matched the analytically derived solutions for $r = 1.91438$Å. We similarly found $E(\theta)$ and $\theta^\star$ by brute force optimization for values of $r \in [1.0, 4.0]$Å to arrive at energy as a function of r for use as the analytical baseline for our comparative studies.

```
# Define frozen core and active orbitals for electronic states
fo = [0, 1, 2, 3, 4, 10, 11, 12, 13, 14]
ao = [5, 9, 15, 19]

#Loop over internuclear distance
rvalues = np.linspace(1,4,16)

for r in rvalues:
    #Define geometry for molecular Hamiltonian
    geom = create_geom_data(r)
    print("r= ", r)
    output_file.write("r = ",+str(r)+"\n")

    #Define Hamiltonian observable using xacc method with PySCF chemistry package
    H = xacc.getObservable('pyscf', {'basis': 'sto-3g', 'geometry': geom,
                                   'frozen-spin-orbitals': fo, 'active-spin-orbitals': ao})

    qpu = xacc.getAccelerator('aer', {"noise-model": noise_model.toJson(), "sim-type": "density_matrix"})

    ##Create empty results array to store energy and optimal angles
    results = []

    for ansatz in ansatzae:
        #Create the VQE algorithm using ansatz from above
        vqe = xacc.getAlgorithm('vqe', {
                                'ansatz': ansatz,
                                'accelerator': qpu,
                                'observable': H,
                                'optimizer': opt,
                                'gradient_strategy':'central'

                                })
        vqe.execute(buffer)
```

Figure 3.2: A listing of the XACC program used for the VQE algorithm, in which the energy for sequential values of inter-molecular position are estimated. The results presented in **Figure 3.3** correspond to $r = 1.91438$ Å

.

We next incorporate a discrete noise model for each gate comprising the UCC-1 ansatz shown in **Figure 3.1**. We use an isotropic depolarizing noise in which the action of a single-qubit unitary gate G acting on the qubit j in the quantum state ρ is simulated as

$$\xi_j^G(\rho) = (1-p)\rho' + p \sum_k \sigma_j^k \rho' \sigma_j^k \tag{3.8}$$

with $\rho' = G\rho G^\dagger$, $\sigma_j^k \in X_j, Y_j, Z_j$, and the noise parameter $p \in [0,1]$. Errors on a two-qubit gate acting on elements i and j are modeled as $\xi_{i,j}^G(\rho) = \xi_i^I(\xi_j^G(\rho))$ with I the identity operator. In our noisy simulations of the UCC-1 ansatz circuit, we use the built-in aer methods to specify the channel description as described above and applied to all register locations for a value of the noise parameter $p \in \{0.001, 0.01\}$ for the two-qubit gate noise and $p/10$ for the single qubit gate noise as is typical of current devices. We note that aer simulator methods assume that the $u1$ (Z) gate is virtual and has no error, and, as a result, the results of the noisy simulations reported in this paper model the Z gates as noise-free.

The output of the simulation includes the expectation value for each Pauli operator, which are combined to generate the estimate of the electronic energy. We estimate the energy as a function of r for both the original ansatz circuit and a set of randomly compiled circuits. In the presence of the noise operators in Eq. 3.8, numerical simulation with aer produces a density matrix $\rho(\theta)$. We use the density matrix to estimate the expectation value of each Pauli operator as well as the total energy

$$\langle H(\theta)\rangle = \mathrm{Tr}[H(r)\rho(\theta)] \tag{3.9}$$

For randomly compiling the UCC-1 ansatz circuit, we used the commercially available TrueQ software package from Quantum Benchmark (Beale et al., 2020a). The original circuit was programmed in the TrueQ language and randomly compiled using the TrueQ 'randomly_compile' function. The resulting circuit instructions were then translated into OpenQASM for integration with the XACC VQE algorithm as an ansatz data structure, cf. **Figure 3.2**.

For our case study, we simulate a set of ten such randomly compiled (RC) circuits as representative of the effects that uncorrelated stochastic noise will have on the observed expectation value. We compare the average energy expectation values of the 10 RC circuits for different $r \in [1.0, 4.0]$ to those of the original circuit under the same noise conditions, and the analytical baseline established earlier in this section using brute force optimization. We also use the first of these circuits to obtain the energy expectation value through brute force optimization under the influence of noise and compare it to similarly simulated original circuit and the analytically derived noise free solution.

3.3 Results

We present results from numerical simulations of the VQE ansatz circuits in **Figure 3.3**, which plots the expectation value for energy with respect to the variational parameter θ for the noiseless and noisy models. All three curves follow similar sinusoidal patterns, as expected from the analytic results. As summarized in **Table 3.2**, the analytic minimum for the energy was found to be -160.3037 Ha at $\theta^\star = 0.1001$, a noisy simulation of the original circuit with $p = 0.01$ yielded an expectation value of -160.2779 Ha at $\theta^\star = 0.09394$, and the randomly compiled circuit gave a lowest energy value of -160.2685 Ha at the same $\theta^\star = 0.09394$. We did observe deviations in $\theta^\star$ for the RC and original circuit as the noise parameter value increases above $p = 0.10$.

Noisy simulations of the original circuit and the randomly compiled circuit yield different minimal expectation values for energy while the optimal values of $\theta^\star$ remain the same. The energy expectation value and the associated $\theta^\star$ of the noisy original and RC circuit deviate from the noiseless analytic solution to nearly the same extent. The additional single-qubit gates introduced by randomized compiling represent an increase of more than 50% in gate count but do not significantly impact the results between the original and RC circuits. There is a slightly larger

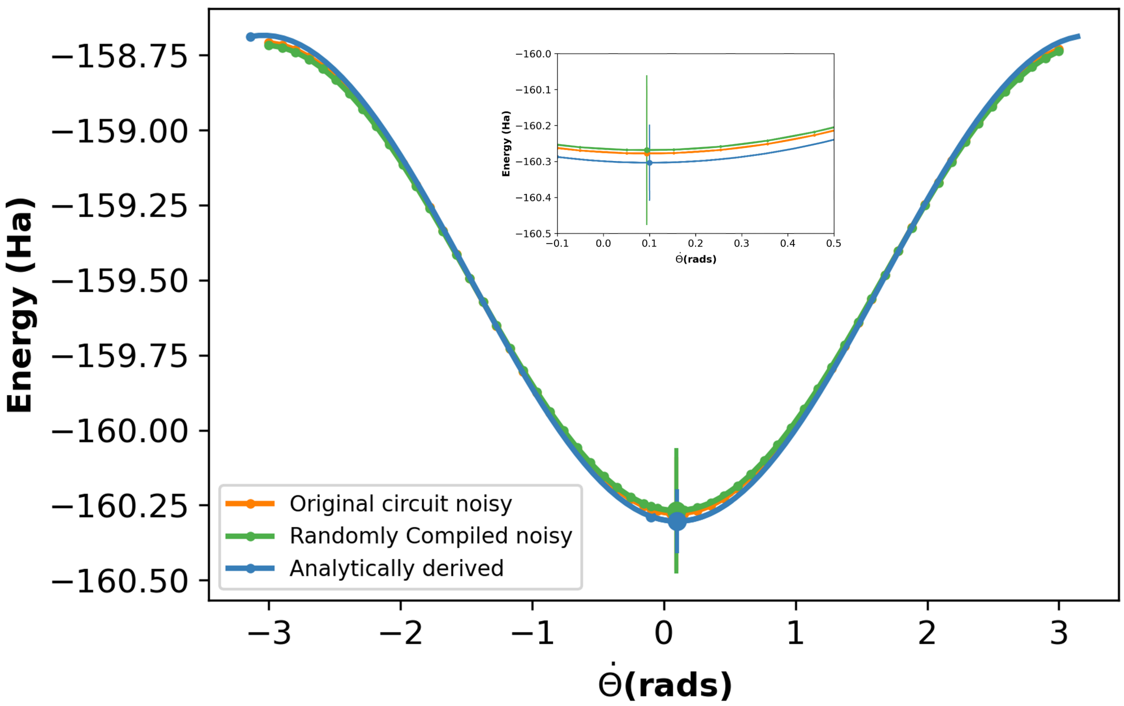

Figure 3.3: The expectation value for the total energy of NaH with respect to the one-parameter, θ, of the UCC-1 ansatz using noise simulation and brute force optimization. The inset magnifies the region near the lowest energy expectation values and corresponding difference in the standard deviation for the original and randomly compiled circuits. See **Table 3.2** for numerical results.

Table 3.2: Optimal parameter, energy expectation value and standard deviation for simulation case studies with $p = 0.01$.

Simulation	θ^*	$E(\theta^*)$ [Ha]	StdDev
Analytically Derived	0.1001	−160.3037	0.1060
Noisy Original Circuit	0.09394	−160.2779	0.1881
Noisy RC circuit	0.09394	−160.2685	0.2085

shift in energy with the RC circuit and an increase in the standard deviation. However, the number of CNOT gates (6) remains constant and these constitute the majority of the noise in the circuit under our noise model.

As noted earlier, the noiseless UCC-1 ansatz fails to match the true ground state of the NaH Hamiltonian and, therefore, the analytic variance from Eq. (3.6) represents a noise floor from which to evaluate the effects of gate noise. As shown in **Figure 3.3** and summarized in **Table 3.2**, the standard deviation of the energy for the noisy simulation of the UCC-1 ansatz for $p = 0.01$ increases by approximately 77% at the optimal angle. The corresponding increase in standard deviation for the randomly compiled circuit is approximately 97%.

We present results from noisy circuit simulations as a function of the inter-molecular distance in **Figure 3.4** over a range of noise parameter values, $p \in \{0, 0.001, 0.01\}$.The energy expectation values follow the results from **Figure 3.3** and are consistently higher for all values of r for noisy ansatzes, including both the original and RC circuits. It is notable that the standard deviation is largest in the range $[1.5, 2.0]$ Å, which corresponds with the lowest energy for the molecular state and the greatest degree of mixing for the ansatz. The analytic curve is constructed from the minimum energy obtained using brute force optimization as shown in **Figure 3.5**. As r approaches 4.0 Å, the corresponding $\theta^\star$ approaches 0 rads, an indication that the prepared electronic state is no longer strongly correlated.

From this case study, we find that additional noise manifests as a dampening of the energy landscape shown in **Figure 3.3**, **Figure 3.4**. However, these shifts are much smaller than the corresponding increases in the variance of the energy. We anticipate this to be a significant challenge for identifying the global energy minimum when using finite sampling and heuristic optimizers.

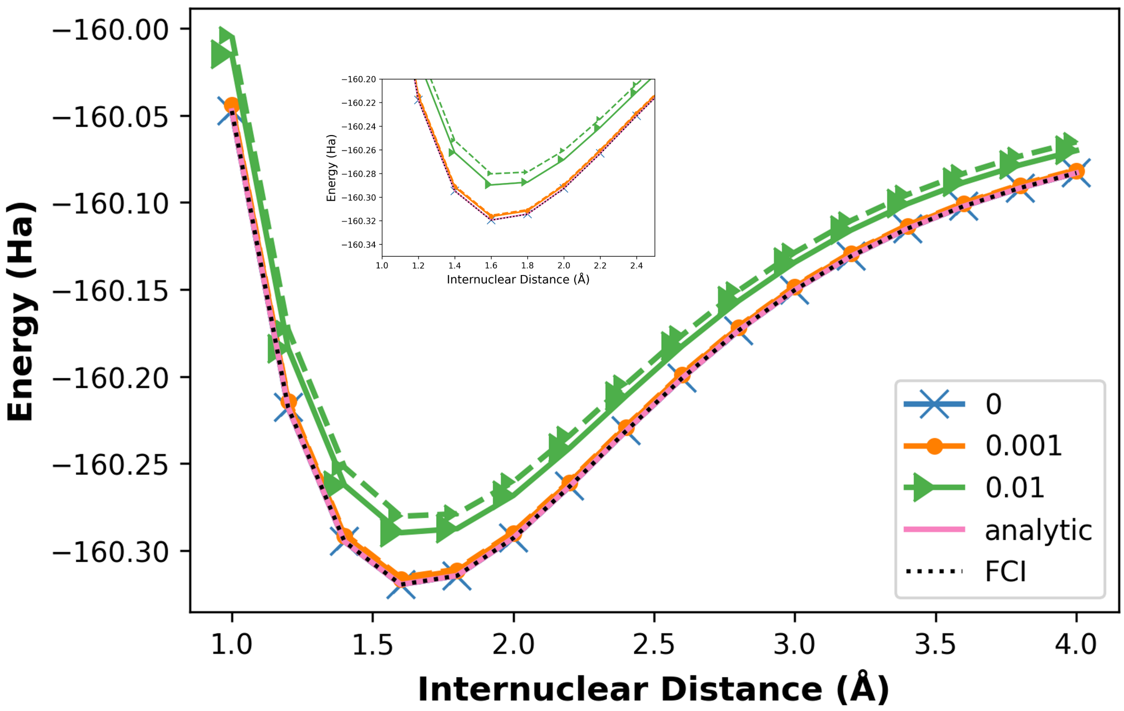

Figure 3.4: The ground-state electronic energy of NaH calculated using VQE with the UCC1 ansatz (solid line) and average of 10 logically equivalent randomly compiled (RC) circuits of the UCC1 ansatz generated with the TrueQ software (dashed line) as a function of inter-nuclear distance of NaH. Lines represent different values of the depolarizing noise parameter p as defined in the text and indicated in the legend. Inset highlights the effect of noise and circuit depth.

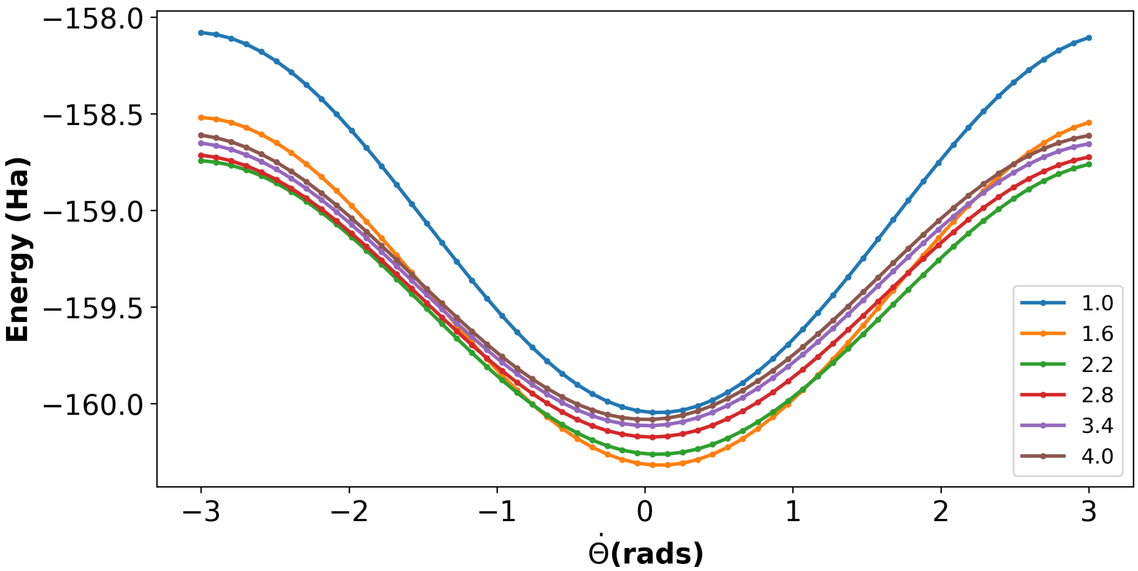

Figure 3.5: Energy as a function of the single parameter, θ, for a range of internuclear distances, $r \in [1.0, 4.0]$Å calculated using VQE with the UCC1 ansatz. Each color represents the energy landscape for the corresponding value of r indicated in the legend.

3.4 Conclusions

We have presented a case study for numerical simulation of noisy VQE ansatz circuits. We present new analytic formulae for the expectation value and variance in energy of the NaH molecule when using the UCC-1 ansatz, and we compare them with noisy circuit simulation when using an isotropic depolarizing noise model. We observe shifts in the energy and variance for the UCC-1 ansatz that suggests that the intrinsic error in the noisy VQE ansatz circuit will limit quantum computational accuracy. This error arises from the limitations of the ansatz circuit as well as the noisy gates that prepare the defined state.

Concerns for the noise floor and error budget play an important role in designing quantum computing applications on current NISQ hardware. While techniques for mitigating errors, such as randomized compiling, offer powerful tools for addressing some of these errors, our results indicate that a trade off between sources of noise is likely to arise in most practical applications.

Acknowledgment

The research is supported by the Department of Energy Office of Science, Basic Energy Sciences. This work used resources of the Oak Ridge Leadership Computing Facility, which is a DOE Office of Science User Facility supported under Contract DE-AC05-00OR22725.

Chapter 4

Numerical Simulations of Noisy Quantum Circuits for Computational Chemistry

Here we investigate the behavior of noisy quantum circuits using numerical simulations to estimate the accuracy and fidelity of the prepared quantum states relative to the ground truth obtained by conventional means. We implement several different types of ansatz circuits derived from unitary coupled cluster theory, some of which were discussed in chapter 3, for the purposes of estimating the ground-state energy of sodium hydride using the variational quantum eigensolver algorithm. We show how relative error in the energy and the fidelity scale with the levels of gate-based noise, the internuclear configuration, the ansatz circuit depth, and the parameter optimization methods. We show how relative error in the energy and the fidelity scale with the levels of gate-based noise, the internuclear configuration, the ansatz circuit depth, and the parameter optimization methods. [*]

---

[*] Meenambika Gowrishankar and Jerimiah Wright contributed equally to the manuscript in this chapter. Contributions by M Gowrishankar include studies on the one parameter UCC ansatz and the ansatzes obtained by randomized compiling.

4.1 Introduction

Computation is a staple of predicting the behaviors and properties of new chemicals and materials, and leading computational methods must take advantage of state-of-the-art computers to address the most challenging calculations. The advent of quantum computers has motivated the development and testing of new methods for solving familiar problems by using quantum mechanics itself to perform the computation (Whitfield et al., 2011a; McArdle et al., 2020; Cao et al., 2019a; Bauer et al., 2020). Current quantum computing methods range from fault-tolerant quantum error corrected algorithms that support arbitrarily long calculations to noisy intermediate-scale quantum (NISQ) algorithms that adapt to the error-prone devices available today (Preskill, 2018b). We shall focus on the latter setting but we note the underlying quantum mechanical model affords novel opportunities to simulate the structure and dynamics of chemical systems within both regimes.

Among several approaches to NISQ algorithms, the family of variational methods have emerged in recent years as especially promising for testing the behavior of noisy quantum devices. Typified by the variational quantum eigensolver (VQE) (McClean et al., 2016b), these algorithms use tunable quantum circuits to prepare approximations to the quantum mechanical states of a model Hamiltoninan (O'Malley et al., 2016). The familiar variational principle offers a promise that the parameters which minimize the observed energy also prepare the best approximation to the Hamiltonian ground state, while modifications of this approach may be used to approximate higher energy eigenstates, i.e., excited states (Claudino et al., 2021).

Multiple experimental investigations have tested the principles of VQE for recovering the electronic states of small molecular Hamiltonians (Kandala et al., 2017; McCaskey et al., 2019; Sokolov et al., 2020b; Yeter-Aydeniz et al., 2021; Arute et al., 2020). Those results indicate that the choice of the parameterized quantum circuit, i.e., the ansatz, plays a significant role in the accuracy of the estimated energy as well as the complexity of finding the optimal parameters. In particular, development of an expressive and efficient ansatz is essential to temper the influence of noise and errors that arise during experimental implementation (Grimsley et al., 2019a; Bauman et al., 2019; Xia and Kais, 2020; Metcalf et al., 2020; Mizukami et al., 2020; Elfving et al., 2021; Tkachenko et al., 2021). Many different techniques, including symmetry, constraints, and iterative approximations, have been used to further the construction of efficient ansatz circuits (Grimsley et al., 2019b; Gard et al., 2020; Tang et al., 2021).

Despite the continuing improvement of such experimental demonstrations, there is an outstanding question as to how the fidelity of the prepared quantum state compares to the idealized pure state representation of the sought electronic ground state. All demonstrations to date are well within the range of conventional computation yet the leading observable for comparison is the energy estimate and not the state. By construction, the applied ansatz circuit has a best approximation to the true ground state of the given Hamiltonian operator, but the accuracy with which this state is found is not the leading metric for experimental validation. This is due primarily to the complexity of estimating the prepared state, which requires tomographic techniques for reconstructing the quantum state (Sagastizabal et al., 2019a; Smart and Mazziotti, 2020).

Previously, Claudino et al. investigated the fidelity of several variational methods in approximating the ground state of few-electron molecular models (Claudino et al., 2020). Those results show that VQE methods with sophisticated ansatz circuits could approximate the ground electronic state with very high fidelity in the absence of circuit noise, depending on the ansatz and method of parameter selection. However, implementations on NISQ devices are prone to noise that leads to errors in state preparation, and there is an outstanding need to assess how noise influences circuit accuracy. The effects of noise and errors invalidate the pure-state representation used to motivate VQE methods and lead to significant sources of uncertainty in the prepared state.

Here we examine the accuracy and precision of the ansatz in several VQE methods by using numerical simulations of the noisy quantum circuits. This includes the nominal form of VQE with one- and two-parameter ansatz circuits derived from unitary coupled cluster (UCC) theory as well as the more sophisticated ADAPT-VQE. In both instances, the ansatz is inspired by how coupled cluster theory approximates the ground state based on a basis of singly and doubly excited determinants (UCCSD) as well as a basis of singlet adapted configurations (singlet-adapted UCCSD). We investigate variations in parameter optimization due to noisy gate operations, testing the COBYLA(Powell, 1998) (derivative-free) and BFGS(Nocedal, 1980; Liu and Nocedal, 1989) (gradient-based) optimizers, and in all cases we consider the influence of gate noise on the estimated energy and prepared state fidelity. As a test case, we simulate VQE calculations of the expected ground state and energy for sodium hydride (NaH) and we compare with conventional electronic structure calculations.

The remainder of the presentation is organized as follows: in Sec. 4.2, we present the background on the theory for the VQE methods and ansatz circuits; in Sec. 4.3 we present the methods in which we conducted the noisy and noiseless numerical simulations; in Sec. 4.4, we present results from numerical simulations of the noisy ansatz circuits and we make comparisons with conventional solutions in terms of energy and state fidelity; and in Sec. 4.5, we discuss conclusions from our analysis.

4.2 Variational Quantum Eigensolver Methods

Within the context of computational chemistry, the non-relativistic, time-independent molecular Hamiltonian is

$$\hat{H}_{\text{mol}} = -\sum_i \frac{\nabla^2_{R_i}}{2M_i} - \sum_i \frac{\nabla^2_{r_i}}{2m_i} - \sum_{i,j} \frac{Z_i}{|R_i - r_j|} + \sum_{i,j>i} \frac{Z_i Z_j}{|R_i - R_j|} + \sum_{i,j>i} \frac{1}{|r_i - r_j|} \quad (4.1)$$

with R_i the coordinate of the i-th nuclei of mass M_i and charge Z_i and with r_i the coordinate of the i-th electron with mass $m_e = 1$ and charge $e = 1$. Under the Born-Openheimer approximation, the molecular Hamiltonian is decomposed into an electronic Hamiltonian and nuclear Hamiltonian. By adopting a spin-orbital basis $\{\varphi_p : p = 1, \ldots, N\}$ for the electronic degrees of freedom, the second-quantized form of the electronic Hamiltonian is expressed as

$$H(R) = \sum_{pq} h_{pq}(R) a_p^\dagger a_q + \frac{1}{2} \sum_{pqst} h_{pqst}(R) a_p^\dagger a_q^\dagger a_s a_t \tag{4.2}$$

where the one-electron integrals

$$h_{pq}(R) = \int d\sigma \varphi_p^*(\sigma) \left(\frac{\nabla_r^2}{2} - \sum_i \frac{Z_i}{|R_i - r|} \right) \varphi_q(\sigma) \tag{4.3}$$

and two-electron integrals

$$h_{pqst} = \int d\sigma_1 d\sigma_2 \frac{\varphi_p^*(\sigma_1)\varphi_q^*(\sigma_2)\varphi_s(\sigma_1)\varphi_t(\sigma_2)}{|r_1 - r_2|} \tag{4.4}$$

are taken with respect to the variable σ denoting both spin and position and depend on the nuclear coordinates R. The associated fermionic creation and annihilation operators satisfy the anti-commutation relations

$$\{a_p^\dagger, a_q\} = \delta_{p,q} \qquad \text{and} \qquad \{a_p, a_q\} = 0 \tag{4.5}$$

The fermionic representation of the Hamiltonian in (4.2) may be transformed into a qubit representation using the usual Pauli operators

$$X = \begin{pmatrix} 0 & 1 \\ 1 & 0 \end{pmatrix}, \quad Y = \begin{pmatrix} 0 & -i \\ i & 0 \end{pmatrix}, \quad \text{and} \quad Z = \begin{pmatrix} 1 & 0 \\ 0 & -1 \end{pmatrix} \tag{4.6}$$

which satisfy $[X, Y] = -2iZ$. Several transformations into the qubit representation are known to satisfy the necessary fermionic commutation relations, and we employ the Jordan-Wigner transformation defined as

$$a_p^\dagger = \otimes_{i<p} Z_i \otimes \sigma_p^-, \quad \text{and} \quad a_p = \otimes_{i<p} Z_i \otimes \sigma_p^+ \tag{4.7}$$

in terms of the qubit raising and lower operations $\sigma_p^\pm = (X_p \pm iY_p)/\sqrt{2}$. The implementation of this transformation requires $n \geq N$ qubits, and the resulting representation of the fermionic Hamiltonian is

$$H(R) = \sum_j c_j(R) P_j \tag{4.8}$$

where P_j denotes the j-th string of Pauli operators over n qubits and $c_j(R)$ is the corresponding coefficient. The maximum number of terms in (4.8) is 4^n but, in practice, symmetries within the Hamiltonian significantly reduce the number of terms that have non-zero coefficients (Romero et al., 2018a).

The variational quantum eigensolver (VQE) method estimates the minimal expectation value of a Hermitian operator with respect to a variable quantum circuit. The method relies on the variational principle, which states that only the lowest eigenstate of a non-negative operator can minimize the expectation value. Here, we use the the qubit representation of the electronic Hamiltonian as the operator of interest, such that the estimated energy expectation value is

$$E(R; \theta^\star) = \min_\theta \langle \psi(\theta) | H(R) | \psi(\theta) \rangle \tag{4.9}$$

where $|\psi(\theta)\rangle = U(\theta)|\psi(0)\rangle$ is a variable pure quantum state prepared by a (unitary) ansatz operator $U(\theta)$. The parameter $\theta^\star$ denotes the optimal value that minimizes the energy, and a generalization of θ may include multiple parameters within the ansatz.

The critical choice in applying the VQE method to a given Hamiltonian is selection of the ansatz operator $U(\theta)$ and the underlying reference state $\psi(0)$. The latter may be selected by using conventional approximations to the electronic ground state that are efficiently encoded as superpositions of binary states. For example, using the Hartree-Fock solution to the electronic Hamiltonian offers a convenient choice for the reference state, and the vacancy or occupation of a molecular orbital may be encoded by 0 or 1, respectively. The choice of the ansatz operator may also be drawn from conventional electronic structure theory, and many recent efforts have focused on unitary coupled cluster (UCC) theory to generate possible choices for the ansatz operator (Romero et al., 2018a; Sokolov et al., 2020a). The accuracy with which a given ansatz operator represents the true ground state of the Hamiltonian may be quantified using the fidelity

$$F = |\langle \Psi | U(\theta) | \psi(0) \rangle|^2 \tag{4.10}$$

where Ψ is the expected ground state in the qubit representation. We next review a family of ansatz operators derived from UCC theory.

4.2.1 Unitary Coupled Cluster Ansatz Operators

Consider the fermionic UCC ansatz operator (Romero et al., 2018a)

$$U(\theta) = \exp\left(T(\theta) - T^\dagger(\theta)\right) \tag{4.11}$$

where

$$T(\theta) = \sum_{k=1}^{M} T_k(\theta) \tag{4.12}$$

and $T_k(\theta)$ represents the k-th cluster operator of M electrons excited. The unitary operator (4.11) may be approximated to first order by the finite series (Barkoutsos et al., 2018)

$$U(\theta) \approx \prod_{m=1}^{M} e^{\tau_m(\theta)} \tag{4.13}$$

with $\tau_m(\theta) = T_m(\theta) - T_m^\dagger(\theta)$ and M is the series limit. Terminating the series at $M = 2$ limits the theory to single and double excitations and yields what is known as the UCC singles and doubles (UCCSD) ansatz

$$U_{\mathrm{SD}}(\theta) = e^{\tau_1(\theta)} e^{\tau_2(\theta)} \tag{4.14}$$

where

$$T_1(\theta) = \sum_{\substack{i \in \mathrm{occ} \\ a \in \mathrm{virt}}} \theta_i^a \hat{t}_i^a \tag{4.15}$$

and

$$T_2(\theta) = \sum_{\substack{i,j \in \mathrm{occ} \\ a,b \in \mathrm{virt}}} \theta_{i,j}^{a,b} \hat{t}_{i,j}^{a,b} \tag{4.16}$$

with $\hat{t}_i^a = a_a^\dagger a_i$, $\hat{t}_{i,j}^{a,b} = a_a^\dagger a_b^\dagger a_i a_j$ and the vector θ defines the single- and double-excitation parameters θ_i^a and $\theta_{i,j}^{a,b}$, respectively, for excitations from occupied orbitals i and j to virtual orbitals a and b of the reference state.

The ansatz operator in (4.14) may be transformed by the Jordan-Wigner transformation (4.7) to yield the individual terms

$$\tau_1(\theta) = \frac{i}{2} \sum_{i,a} \theta_i^a P_i^a \tag{4.17}$$

and

$$\tau_2(\theta) = \frac{i}{8} \sum_{\substack{i,j \in \mathrm{occ} \\ a,b \in \mathrm{virt}}} \theta_{i,j}^{a,b} Q_{i,j}^{a,b} \tag{4.18}$$

with

$$P_i^a = \otimes_{k=i}^{a-1} Z_k \left(X_a Y_i - Y_a X_i \right) \tag{4.19}$$

and

$$
\begin{aligned}
Q_{i,j}^{a,b} = \otimes_{k=i}^{a-1} Z_k \otimes_{\ell=j}^{b-1} Z_\ell \quad & (X_a X_b X_i Y_j + X_a Y_b Y_i Y_j + X_a X_b Y_i X_j + Y_a X_b Y_j Y_i \\
& - Y_a Y_b Y_i X_j - Y_a X_b X_i X_j - Y_a Y_b X_i Y_j - X_a Y_b X_i X_j)
\end{aligned}
\tag{4.20}
$$

Recalling that $X_k = iY_k Z_k$, the latter may be recast as

$$
\begin{aligned}
Q_{i,j}^{a,b} = \otimes_{k=i}^{a-1} Z_k \otimes_{\ell=j}^{b-1} Z_\ell \quad X_a X_b X_i Y_j & (I_a I_b I_i I_j - I_a Z_b Z_i I_j + I_a I_b Z_i Z_j - Z_a I_b Z_j I_i \\
& + Z_a Z_b Z_i Z_j - Z_a I_b I_i Z_j + Z_a Z_b I_i I_j - I_a Z_b I_i Z_j)
\end{aligned}
\tag{4.21}
$$

where, under the Z operator, occupied orbitals yield an eigenvalue $+1$ and virtual orbitals yield an eigenvalue -1 such that each operator $Q_{i,j}^{a,b}$ is determined by the single four-qubit Pauli string $X_a X_b X_i Y_j$.

The UCCSD operator serves as our starting point for developing various ansatz operators. First, we define a one-parameter ansatz operator derived from the UCCSD ansatz by considering only contribution from the doubles excitations in (4.21). For the four-qubit encoding of two-electrons described below, the resulting UCC doubles (UCCD) ansatz operator is reduced to

$$
U(\theta) = e^{i\theta Y_0 X_1 X_2 X_3} \tag{4.22}
$$

We also consider a singlet-adapted variation of the UCCSD ansatz for which the state is defined in a basis of restricted determinants. Specifically, we restrict the ansatz to basis states that are, by construction, spin eigenstates with $S^2 = 0$. Such states are formed from linear combinations of the corresponding excitation operators that conserve electron spin and obey the spin symmetry. These linear combinations are often referred to in chemistry as configuration state functions or symmetry-adapted basis functions. We defer the description of constructing these linear combinations to prior work (Szabo and Ostlund, 1984). Various details on both ansatz operators have been reported previously (McCaskey et al., 2019; Claudino et al., 2020).

An alternative to the fixed-depth ansatz operators above is an adaptive ansatz that changes the generating operator based on iterative evaluations of the energy estimate. Grimsley et al. first proposed the adaptive derivative-assembled pseudo-trotter (ADAPT) ansatz motivated by UCC theory in which the unitary (4.11) is expanded beyond first order (Grimsley et al., 2019b). They showed how the resulting operator expression guides iteratively growing an ansatz circuit until a desired convergence in the expectation value is obtained. The ADAPT method begins by decomposing the individual single- and double-excitations operators represented by (4.14) into a set known as the operator pool. Let $\mathrm{T} = \{\hat{t}_i^a\} \bigcup \{\hat{t}_{i,j}^{a,b}\}$ denote the operator pool derived from the UCCSD approximation. An exact ansatz operator may be expressed as

$$U_{SD}(\theta) = \prod_{k}^{\infty} \prod_{i,a} \exp\left[\theta_{i,k}^{a}(\hat{t}_i^a - \hat{t}_a^i)\right] \prod_{i,j,a,b} \exp\left[\theta_{i,j,k}^{a,b}(\hat{t}_{i,j}^{a,b} - \hat{t}_{a,b}^{i,j})\right] \tag{4.23}$$

in which k indexes the different instances of each excitation operator.

The ADAPT method creates an approximation to (4.23) by selecting a subset of elements in the operator pool T to generate an ansatz operator. Operator selection is initialized with a starting ansatz operator which, for example, prepares the Hartree-Fock state for the given Hamiltonian. The selection then evaluates the commutator between each operator in the pool and the Hamiltonian with respect to the presently prepared state. The resulting vector of commutator evaluations defines a gradient that is steepest in the direction of the operator with the largest commutator. The operator corresponding to the largest commutator is then appended to the ansatz operator and, therefore, the ansatz circuit for the next evaluation of VQE. An associated parameter is introduced to tune the unitary rotation represented by the new operator, such that the number of optimized parameters grows with the size of the ansatz. When the norm of the gradient vector is less than a defined threshold, the algorithm converges and the lowest energy state is recovered.

4.2.2 Ansatz Compilation

The above ansatz operators must be compiled into quantum circuits for execution. We use the XACC programming framework to synthesize circuits representing these ansatz operators. XACC provides a set of software methods to define and implement fermionic and spin transformations that reduce the operator expressions above into a sequence of discrete quantum gates (McCaskey et al., 2020). In addition, the accompanying VQE and ADAPT-VQE methods orchestrate iterative execution of the ansatz and search through the corresponding parameter space. We defer details on the compilation methods to prior references (McCaskey et al., 2019; Grimsley et al., 2019b). The results include, for example, the compiled one-parameter UCCD ansatz from (4.22) decomposed into the sequence of one- and two-qubit gate operations shown in **Figure 4.1**. Compiled circuits are then simulated and XACC facilitates this step as well. Here we perform numerical simulations that interface the compiled circuits with a simulator that otherwise faithfully execute the VQE and ADAPT-VQE methods. Details on the numerical simulations are reviewed below.

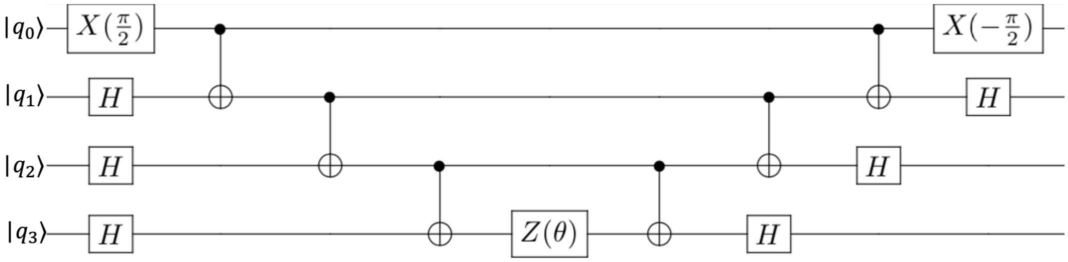

Figure 4.1: The quantum circuit diagram representing the one-parameter UCCD ansatz used in the numerical studies reported here. This ansatz was originally reported in Ref. (McCaskey et al., 2019).

We also study the effect of noise on circuits generated using the randomized compiling method that are logically equivalent to the UCCD one parameter ansatz but have a higher gate depth. Specifically, we consider randomized compiling to transform ansatz circuits by introducing independent, random single-qubit gates such that the output circuit is logically equivalent to the original (Wallman and Emerson, 2016b). The technique is implemented by dividing gate sets into so-called 'easy' and 'hard' gates and then reorganizing the original circuit into clock cycles alternating between a round of easy and hard gates applied to disjoint qubits per cycle (Wallman and Emerson, 2016b). Each round of easy gates is conjugated by a twirling gate T_k from a twirling gate set and an inverse operator T_{k-1}^c. The original single qubit gates and the twirling gates are then compiled into new easy gate cycles.

Randomized compiling was developed to address coherent and correlated noise by effectively transforming the noise into a stochastic Pauli noise channel. While randomized compiling can offer improvements in circuit performance (Hashim et al., 2021), our investigation does not test such promises due to the selected noise model described in the next section. Rather, we investigate the role that additional gates in the ansatz circuit have on the increased circuit depth and output state fidelity. We limit our analysis to randomized compiling of the UCCD ansatz circuit due to its simplicity and single variational parameter. At the time that we used the commercially available TrueQ software package to generate these circuits, it was not equipped to compile parametrized operators of the circuit.(Beale et al., 2020b).

4.3 Numerical Methods

For our numerical studies, we use the model of a two-electron Hamiltonian representing sodium hydride (NaH) within the frozen-core approximation and with the STO-3G basis set. We require $n = 4$ qubits to encode the two spin-orbitals using the Jordan Wigner transformation, and the corresponding Pauli representation of terms in the electronic Hamiltonian is summarized in **Table 4.1**.

As described previously, we use the XACC framework to compile the ansatz circuits and perform optimization of the ansatz parameters with respect to the estimated energy. The compiled circuits are simulated numerically using the IBM aer simulator as the XACC qpu backend, and we integrate a noise model that describes each gate by a noisy operation.

Table 4.1: Four-spin representation of the two-electron, NaH Hamiltonian and expectation value of the Pauli strings with respect to the UCCD ansatz for $r = 1.91438\text{Å}$.

j	$c_j(r_0)$ [Ha]	P_j	$\langle P_j(\theta)\rangle$
0	-159.40289	$I_0I_1I_2I_3$	1
1	0.0323625	$X_0X_1I_2I_3$	0
2	0.0202421	$X_0X_1X_2X_3$	$-\sin\theta$
3	0.0202421	$X_0X_1Y_2Y_3$	$-\sin\theta$
4	0.0229208	$X_0X_1Z_2I_3$	0
5	-0.00944179	$X_0X_1I_2Z_3$	0
6	0.0323625	$I_0I_1X_2X_3$	0
7	0.0323625	$Y_0Y_1I_2I_3$	0
8	0.0202421	$Y_0Y_1X_2X_3$	$-\sin\theta$
9	0.0202421	$Y_0Y_1Y_2Y_3$	$-\sin\theta$
10	0.0229208	$Y_0Y_1Z_2I_3$	0
11	-0.00944179	$Y_0Y_1I_2Z_3$	0
12	0.0323625	$I_0I_1Y_2Y_3$	0
13	0.0149385	$Z_0I_1I_2I_3$	$-\cos\theta$
14	0.0229208	$Z_0I_1X_2X_3$	0
15	0.0229208	$Z_0I_1Y_2Y_3$	0
16	0.0816923	$Z_0Z_1I_2I_3$	-1
17	0.158901	$Z_0I_1Z_2I_3$	1
18	0.101934	$Z_0I_1I_2Z_3$	-1
19	-0.387818	$I_0Z_1I_2I_3$	$-\cos\theta$
20	-0.00944179	$I_0Z_1X_2X_3$	0
21	-0.00944179	$I_0Z_1Y_2Y_3$	0
22	0.101934	$I_0Z_1Z_2I_3$	-1
23	0.117450	$I_0Z_1I_2Z_3$	1
24	0.0149385	$I_0I_1Z_2I_3$	$-\cos\theta$
25	0.0816923	$I_0I_1Z_2Z_3$	-1
26	-0.387818	$I_0I_1I_2Z_3$	$\cos\theta$

In modeling noise in the quantum circuits, we assume a model by which each one- and two-qubit gates are followed by a depolarizing noise channel. The depolarizing noise model is a convenient device agnostic noise model that offers a coarse-grain representation for the loss of coherence caused by a noisy circuit, particularly for few-qubit numerical simulations (Temme et al., 2017b). By setting the depolarizing noise to $p = 0$, we are able to simulate a noiseless circuit. We then chose a few parameters, where $p > 0$, that mimic the settings of current hardware(Dahlhauser and Humble, 2021). Although it does not provide a fine-grain representation of the noise process, it has been used previously for accurately modeling the output from NISQ devices (Dahlhauser and Humble, 2021). In addition, randomized compiling is known to yield a statistical model for the quantum circuit noise that is well approximated by the depolarizing model and motivates our use for the model here (Ville et al., 2021).

Within this model, the action of a single-qubit unitary gate G acting on register element j in the quantum state ρ is simulated as

$$\xi_j^G(\rho) = (1-p)\rho' + p\sum_k \sigma_j^k \rho' \sigma_j^k \tag{4.24}$$

with $\rho' = G\rho G^\dagger$, $\sigma_j^k \in X_j, Y_j, Z_j$, and the noise parameter $p \in [0, 1]$. Errors on a two-qubit gate acting on elements i and j are modeled similarly as $\xi_{i,j}^G(\rho) = \xi_i^I(\xi_j^G(\rho))$ with I the identity operator. For our simulations, we use a gate set consisting of the single-qubit Pauli operator, the Hadamard gate, and single-qubit rotations with the two-qubit CNOT gate. These gates are decomposed by XACC into the OpenQASM representation (McKay et al., 2018). Notably, OpenQASM gates that are diagonal in the computational basis, e..g, Z, are not modeled with noise, a consequence of using the IBM aer simulator. For our noise model, we use noise levels for the two-qubit CNOT gate that is always ten times the value of the single-qubit gate noise. This is motivated by the difference in noise values observed in hardware. We use the same noise level for all single-qubit gates.

For different values of noise, we explore the influence of methodology on parameter optimization by comparing results from two different optimizers, COBYLA and L-BFGS. These two optimizers were chosen as gradient-free and gradient-based methods respectively. Constrained optimization by linear approximation (COBYLA) constructs and optimizes a series of linear approximations to the objective function to compute parameter steps that minimize the objective function (Powell, 1998). We use the third-party library implementation nlopt with a maximum number of iterations set to 1,000 with a convergence tolerance of 10^{-6} (Johnson, 2007). By comparison, the low-memory Broyden-Fletcher-Goldfarb-Shanno (L-BFGS) method is a quasi-Newton method that uses the gradient and an approximate Hessian to determine steps in parameter space that minimize the objective function (Nocedal, 1980; Liu and Nocedal, 1989). We use the third-party library implementation mlpack with the central gradient method with a maximum number of iterations set to 500,000 with a convergence tolerance of 10^{-4} and numerical step set to 10^{-7} (Curtin et al., 2018).

The output of each simulation is a list of expectation values characterizing the individual Pauli terms representing the Hamiltonian shown in **Table 4.1**, which are then combined to estimate the electronic energy. In addition, the output includes the simulated quantum state in the form of a density matrix. We compare the simulated energy estimate and simulated state with the energy and state obtained for the same Hamiltonian molecule calculated using the complete active-space self-consistent field (CASSCF) method within pyscf (Sun et al., 2018). We investigate different levels of noise as well as the behavior with respect to inter-nuclear configuration.

4.4 Results

We conduct a range of studies of the above noise model applied to VQE and ADAPT-VQE simulations of the NaH molecule. We compare the statistics and fidelity of the expectation values of the noisy and noiseless simulations across a range of values for the internuclear distance, R, and different optimizers. For the studies with VQE we study the simulations of the original circuit and compare them with the results of the randomly compiled circuits. The goal is to understand how noise affects these properties and if there are parameters that are more resilient to noise than others.

We begin our study of the results of the ground state electronic energy calculation and fidelity of the prepared state with our simplest ansatz, the UCCD bare circuit (BC) ansatz, shown in **Figure 4.2**. The simulated ground state energy predictably increases with increases in the depolarizing noise parameter p across all R. In addition the fideitly accross all R drops as we increase the depolarizing parameter. The increase in energy from the noisless simulation is no greater than 0.03 Ha at the greatest level of noise, while the fidelity drops less than 5%. Additionally, the overall shape of the curve is fairly standard for a potential energy curve, and the fidelity is relatively flat across all R.

We report little difference between the optimizers used to find the energy and the fidelity of the this ansatz. **Figure 4.3** plots the optimal parameters found to represent the ground state in the UCCD ansatz using the COBYLA and L-BFGS optimizers. There are noticeable differences in the parameters returned by COBYLA and L-BFGS with the latter showing a smoother variation across different levels of the noise parameter, especially at larger values of R. These differences however, didn't correspond to any significant difference to the reported energy or fidelity of the respective optimizer.

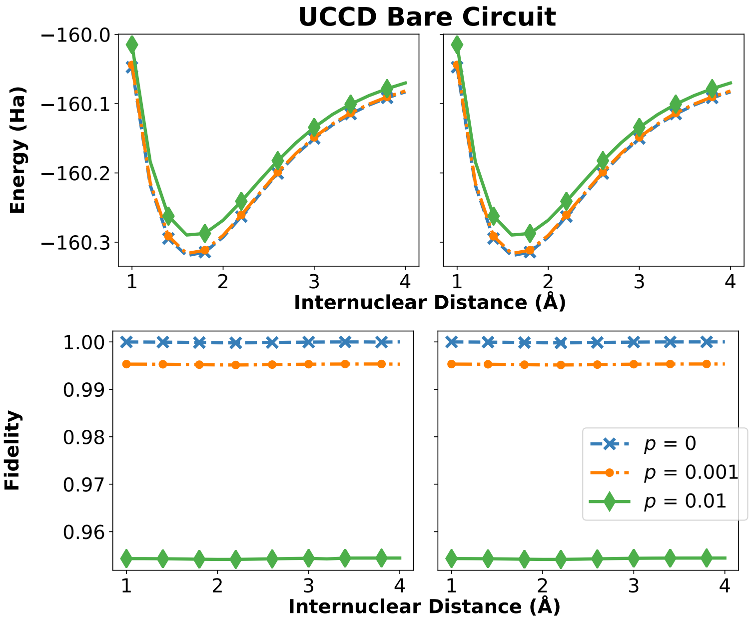

Figure 4.2: The top row presents the ground state electronic energy of NaH using the UCCD bare circuit ansatz within the VQE method with different levels of depolarizing noise, p. The bottom row presents the corresponding fidelity of the prepared quantum state and that of the ground state found through conventional means. The left and right columns differentiate the results found using the COBYLA and L-BFGS optimizers respectively.

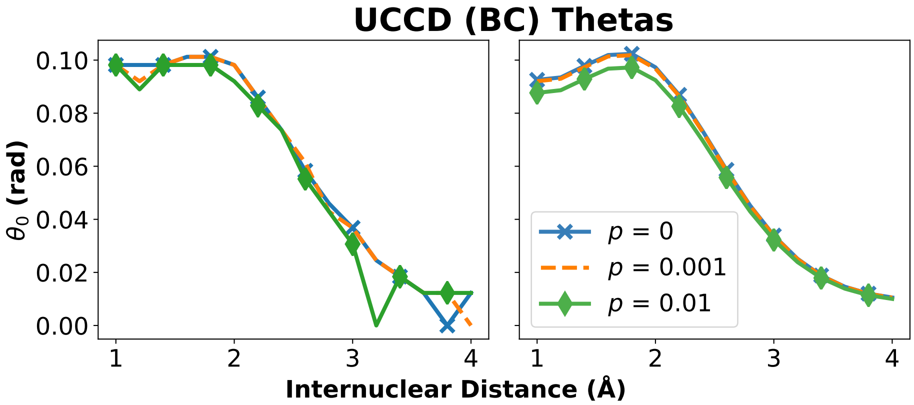

Figure 4.3: The optimal parameters for the ground state energy of the bare UCCD ansatz found using the Cobyla (left) and L-Bfgs (right) optimizers.

Figure 4.4 plots the results of the UCCD randomly compiled (RC) ansatz simulation at varying levels of depolarizing noise. Similar to the bare UCCD ansatz, the simulated ground state energy increases with increases in the noise parameter across all R. Again, we see a corresponding drop in fidelity as we increase the noise parameter, and minimal differences in the reported energy and fidelity when comparing the COBYLA and L-BFGS optimizers. The increase in energy from the noiseless simulation is no greater than 0.04 Ha at the greatest level of noise, while the fidelity drops less than 6%.The overall shape of the curve is standard for a potential energy curve, and the fidelity is relatively flat across all R.The plotted thetas in **Figure 4.5** show a different selection of optimal parameters between the COBYLA and L-BFGS optimizers. Like the bare UCCD ansatz,there are obvious difference between the selected optimal parameter for the ground state as the depolarizing noise increases for both optimizers. For example, the COBYLA optimizer has a greater varriance than that of the L-BFGS optimzer, especially at higher values of R. When comparing the differences in optimal parameter selection between optimizers at the same level of noise, we report no significant difference to the resultant energy or fidelity between the respective optimizers.

The energy and fidelity results of the Singlet-Adapted-UCCSD ansatz are reported in **Figure 4.6**. The general trend of increasing energy and decreasing fidelity as the depolarizing noise increases is still seen within this plot. The general shape of the energy curve is standard to that of potential energy curves, and the fidelities are relatively flat across all R. While there is negligible difference between the reported values of the energy and fidelity between optimizers, there is significant difference between the reported values at varying levels of the noise parameter. The increase in energy from the noiseless simulation is no greater than 0.3 Ha, while the fidelity drops less than 40% at the greatest value of noise.

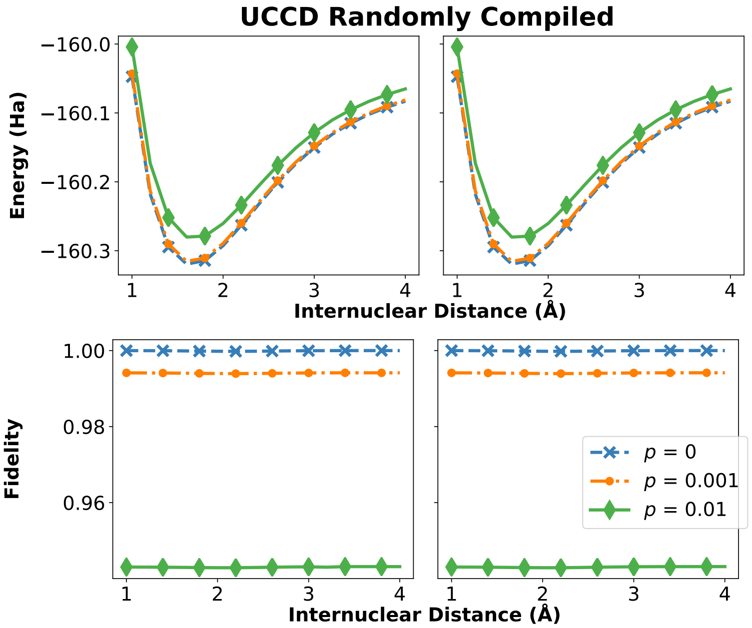

Figure 4.4: The top row presents the ground state electronic energy of NaH using the UCCD randomly circuit ansatz within the VQE method with different levels of depolarizing noise, p. The bottom row presents the corresponding fidelity of the prepared quantum state and that of the ground state found through conventional means. The left and right columns differentiate the results found using the COBYLA and L-BFGS optimizers respectively.

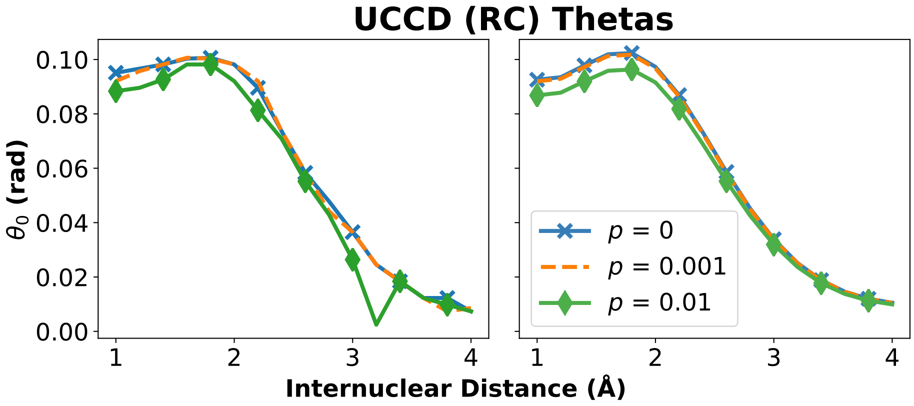

Figure 4.5: The optimal paramters for the ground state enegy of the randomly compiled UCCD ansatz found using the Cobyla (left) and L-Bfgs (right) optimizers.

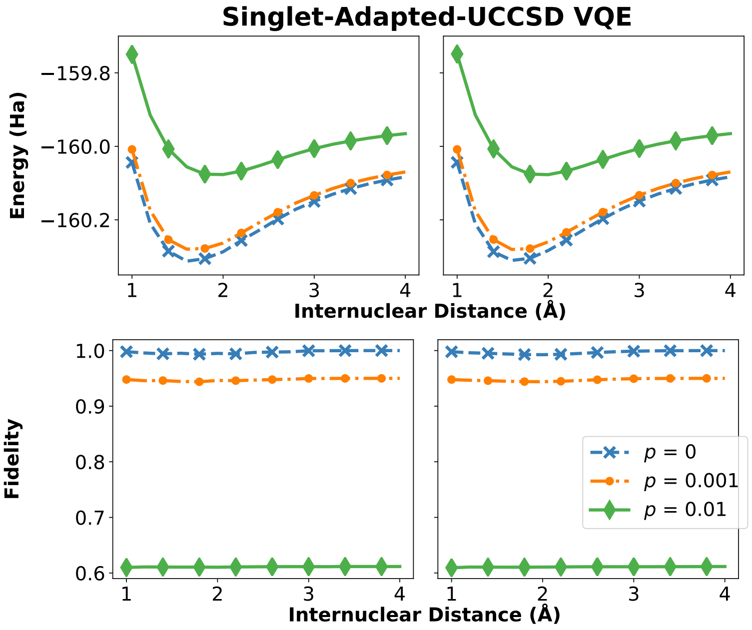

Figure 4.6: The top row presents the ground state electronic energy of NaH using the Singlet-Adapated-UCCSD ansatz within the VQE method with different levels of depolarizing noise, p. The bottom row presents the corresponding fidelity of the prepared quantum state and that of the ground state found through conventional means. The left and right columns differentiate the results found using the COBYLA and L-BFGS optimizers respectively.

Figure 4.7 shows a different selection of optimal parameters between the COBYLA and L-BFGS optimizers. Both optimizers search similar regions but there is noticeable variation in their results. In addition, as the noise level p increases, the parameter search changes in tandem, with the $p = 0.01$ case for the θ_1 parameter showing the most dramatic shift. In general,the COBYLA optimzer varies greatly with a much more jagged curve as we search across all R for both θ_0 and θ_1 when we compare it to that of the L-BFGS optimizer. While being smoother, the L-BFGS optimizer reports similar values of the energy and fidelity to that of the COBYLA optimizer.

The energy and fidelity results of the ADAPT VQE simulation using the singlet-adapted-uccsd operator pool is shown in **Figure 4.8**. The general trend of increasing energy and decreasing fidelity is still seen within in this plot, however with increasing depolarizing noise, the shape of the energy plot deviates from standard potential enegy curves. Likewise, the fidelity of the the state prepared is not flat across all R. The increase in energy from the noiseless simulation is no greater than 1.0 Ha, while the fidelity drops at most a little less than 90% at the greatest value of noise. Contrast to the previous ansatze, the ADAPT-VQE ansatze grow uniquely with respect to R. This growth can be shown by plotting the number of parameters the ADAPT-VQE algorithm used in ansatz construction to reach convergence, which is shown in **Figure 4.9**. There are significant differences in the number of parameters between the COBYLA and L-BFGS optimizers,however,the general trend in this plot shows how the number of parameters decrease as R increases.

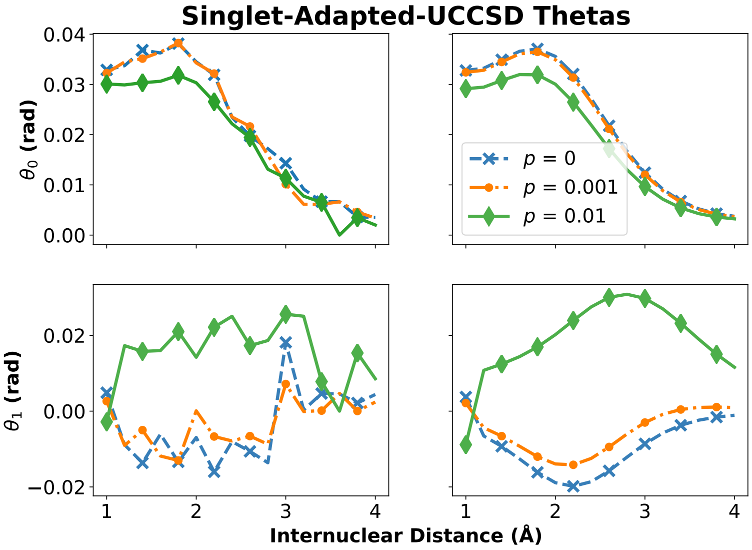

Figure 4.7: The optimal values of the circuit parameters (top row) θ_0 and (bottom row) θ_1 for the singlet-adapted UCCSD ansatz as a function of obtained from VQE with respect to the NaH internuclear distance when using the COBYLA (left column) and L-BFGS (right colum) optimization methods.

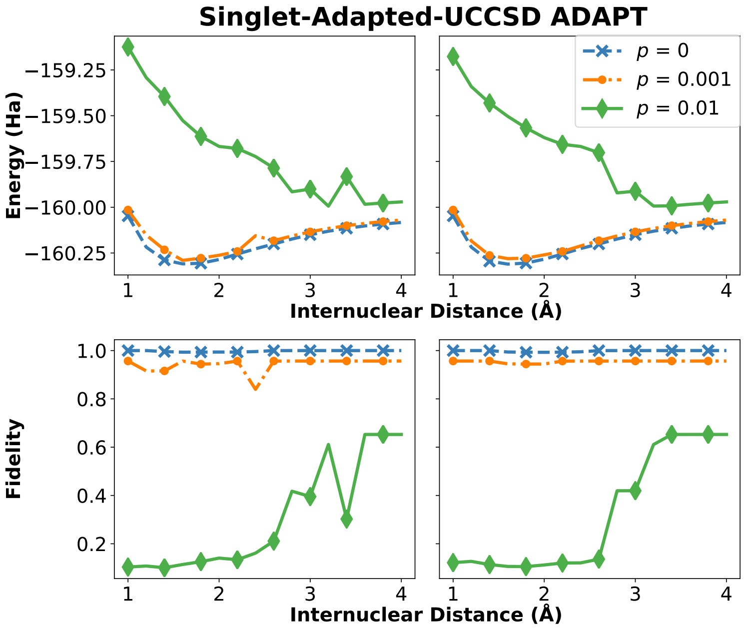

Figure 4.8: The top row presents the ground-state electronic energy of NaH calculated using ADAPT-VQE with Singlet-Adapted-UCCSD operators while the bottom row presents the corresponding fidelity of the prepared quantum state with the ground state calculated using conventional methods. The left and right columns distinguish between the parameters chosen through the COBYLA and L-BFGS optimization routines respectively.

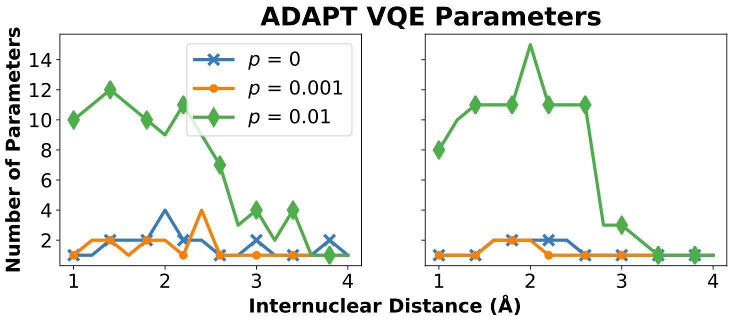

Figure 4.9: The number of optimal parameters chosen by the ADAPT algorithm to reach convergence as a function of the internuclear distance, using the COBYLA (left) and L-BFGS (right) optimizers.

Figure 4.10 plots the absolute error in energy of all the above ansatze simulated from the ground state enegy found through conventional means. As we presented the energy and fidelity data of the different ansatze from the smallest to largest circuits in terms of gate depth, we see a similar trend in the absolute error plot. This is because every one- and two-qubit gate in every circuit is affected by depolarizing noise, thus increasing the number of gates increases the amount of noise in the system. The bare UCCD ansatz is the smallest ansatz and as such sees the smallest change in energy at the greatest value of depolarizing noise. Similarly, the randomly compiled circuits result in slightly larger increase for the same noise level due to the presence of additional one-qubit gates. On average, the randomly compiled circuits consist of approximately 50% more single-qubit gates than the bare UCCD ansatz. The Singlet-Adapted-UCCSD ansatz has more gates, but more significantly, the ansatz has a higher number of two-qubit, CNOT, gates than that of the previous ansatze. The effect of depolarizing noise is an order of magnitude greater within two-qubit gates than that of one-qubit gates. This translates to a greater increase in energy as the depolarizing parameter increases. Lastly, the ADAPT-VQE ansatze exhibit the greatest increase in energy due to the large increase in one- and two-qubit gates within the circuit. The number of one- and two-qubit gates required for $p = 0.01$ is approximately an order of magnitude higher than those found for any other ansatze tested.

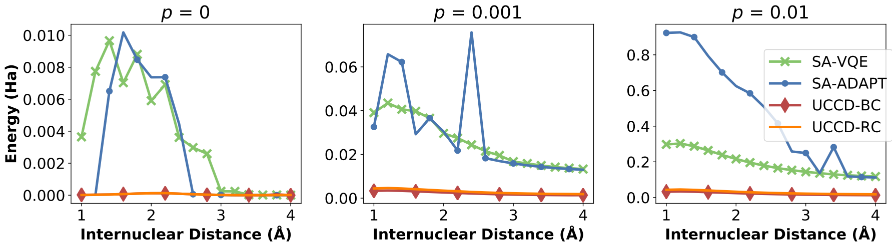

Figure 4.10: The absolute error between the electronic energy of the simulated ansatze and the ground truth found through conventional means. All results shown use the COBYLA optimizer.

4.5 Conclusions

Our goal was to understand how noise affects the energy and fidelity of the ansatz and if there are parameters that are more resilient to noise than others. Across all ansatz circuits, we find that the noiseless simulations always recover the ideal energy and unit fidelity, while in the presence of noise, the depth of the ansatz circuit has the most important influence on the error in these quantities. Increases in gate depth of the ansatz necessarily increases the error in energy and lowers the fidelity and this is amplified at larger noise values. The differences observed between the bare UCCD and the randomly compiled UCCD circuits reflect differences in their single-qubit gate depth while the Singlet-Adapted-UCCSD and ADAPT-VQE related ansatze, reflect differences in the number of two-qubit gates. More specifically, this indicates that the number of CNOT gates is the leading limit on how accurately the ansatz can describe the ground-state wavefunction.

The COBYLA and L-BFGS optimizers do yield different optimal parameters for the UCCD bare circuit, the UCCD randomly compiled circuit, and the Singlet-Adapted-UCCSD circuit however, these differences generally have a small influence on the outcomes of the fidelity and energy. For example, prior work has confirmed that the energy surface characterizing the UCCD ansatz is relatively smooth (Gowrishankar et al., 2021a), while our results presented here confirm similar behavior in the presence of noise. The differences between the two optimizer are more apparent within the ADAPT-VQE method at higher levels of noise, but generally follow the same trend.

A leading feature of the ADAPT-VQE algorithm is that the ansatz grows iteratively to improve the accuracy of the computed energy. This feature allows for variability in the number of and types of gates that make up the ansatz. However, as shown here, variability in the ansatz circuit depth due to increasing depolarizing noise, leads to fluctuations in the energy and fidelity that are not observed within the fixed ansatz.

We studied how depolarizing noise specifically affected different ansatze, but note that other sources of noise could be present in other systems. Thus, this study would not accurately represent systems that included more, or different types of noise such as readout noise or coherent noise. In addition, we are limited to the size of the systems we are able to study due to the use of density matrices which are exponentially larger than statevectors. Finally, we note that the ADAPT-VQE method could be further modified to combat the effects of noise such as modifying the ADAPT-VQE configuration to ensure continuity in the ansatz circuit depth and parameter values. For example, intelligent pruning of the ADAPT ansatz may be beneficial with little loss of accuracy. We defer this point for later work.

4.6 Declarations

Availability of data and materials

The data and materials are available upon request.

Acknowledgements

This research used resources of the Oak Ridge Leadership Computing Facility, which is a DOE Office of Science User Facilities supported by the Oak Ridge National Laboratory under Contract DE-AC05-00OR22725. This research used resources of the Compute and Data Environment for Science (CADES) at the Oak Ridge National Laboratory, which is supported by the Office of Science of the U.S. Department of Energy under Contract No. DE-AC05-00OR22725.

Funding

This work was supported by the “Embedding Quantum Computing into Many-body Frameworks for Strongly Correlated Molecular and Materials Systems” project, which is funded by the U.S. Department of Energy (DOE), Office of Science, Office of Basic Energy Sciences, the Division of Chemical Sciences, Geosciences, and Biosciences. This work was also supported by the Quantum Science Center (QSC), a National Quantum Information Science Research Center of the U.S. Department of Energy (DOE).

Competing interests

The authors declare that they have no competing interests.

Authors’ contributions

J. W. and M. G. developed the methods, performed the experiment, processed the data, and composed the manuscript. D.C. developed the methods and composed the manuscript, P.C.L. processed the data and composed the manuscript, T.N. developed the methods, A.J.M. developed the methods, and T.S.H. processed the data and composed the manuscript.

Chapter 5

Logical Error Rates for a [[4,2,2]]-encoded Variational Quantum Eigensolver Ansatz

As shown in the previous chapters, noisy simulations of the ground state of small quantum chemistry problems using the VQE algorithm decreases the accuracy of the energy estimate and the fidelity of the prepared state. We now focus on mitigating the noise using quantum error detection (QED). QED codes offer a framework by which to encode quantum computations and identify when errors occur. However, the subsequent logical error rate depends on the encoded application circuit as well as the underlying noise. Here, we quantify how the [[4,2,2]] code improves the logical error rate, accuracy, and precision of an encoded variational quantum eigensolver (VQE) application. We benchmark the performance of the encoded VQE for estimating the energy of the hydrogen molecule with a chemical accuracy of 1.6 mHa while managing the trade-off between probability of success of the various post-selection methods. Using numerical simulation of the noisy mixed state preparation, we find that the most aggressive post-selection strategies improve the accuracy and precision of the encoded estimates even at the cost of increasing loss of samples.

5.1 Introduction

Quantum computing hardware has made remarkable strides in improving the coherence times of qubits and the fidelity of gates with error rates in state-of-the-art devices around $0.5 - 0.01\%$ per two-qubit gate (AI, 2023; Evered et al., 2023; Yamamoto et al., 2024). Error rates required for implementing large scale quantum computations are much lower at $\sim 10^{-9}$, which is extremely challenging to achieve on hardware. Such error rates are made possible by the discovery of quantum error correction (QEC) codes, which involve redundantly encoding logical qubits using a larger number of physical qubits such that errors can be detected, decoded and corrected during the computation (Shor, 1995b; Steane, 1996; Calderbank and Shor, 1996; Devitt et al., 2013). The leading QEC codes that promise such error rates at high physical gate error thresholds of 0.1% are the surface code and quantum Low-Density Parity-Check (LDPC) codes (Fowler et al., 2012; Bravyi et al., 2024). However, successfully implementing these error correction codes on near-term devices for large scale quantum algorithms remains an ongoing area of research (AI, 2023; Livingston et al., 2022; Sivak et al., 2023; Ryan-Anderson et al., 2021; Krinner et al., 2022; Acharya et al., 2023; Mayer et al., 2024).

Quantum error detection (QED) codes, on the other hand, can be implemented on current quantum computers. Unlike QEC, quantum error detection uses encoded data qubits only to identify if an error occurred and does not require syndrome decoding or feed-forward operations for its implementation. While QED does not enable fault tolerant implementations, post-selection of the flagged measurement results can be used to improve the accuracy of calculated outcomes. For example, the [[4,2,2]] QED code uses 4 physical qubits to encode 2 logical qubits and detects at most one physical qubit error (Devitt et al., 2013).

QED codes have been studied extensively both theoretically and experimentally (Leung et al., 1997; Knill, 2004, 2005; Reichardt, 2009; Zhong et al., 2014; Córcoles et al., 2015; Gottesman, 2016; Vuillot, 2017; Linke et al., 2017; Willsch et al., 2018; Takita et al., 2017; Rosenblum et al., 2018; Roffe et al., 2018; Chen et al., 2022). Most experiments to date have focused on demonstrating that the QED codes can successfully detect errors during state preparation (Córcoles et al., 2015; Linke et al., 2017; Roffe et al., 2018; Zhong et al., 2014), while others have tested early fault tolerance on near-term devices (Willsch et al., 2018; Vuillot, 2017; Takita et al., 2017; Rosenblum et al., 2018). The [[4,2,2]] code and its variant [[4,1,2]] code have been at the center of most of these studies. Several studies have reported on improvements during state preparation, while others have demonstrated the use for applications (Urbanek et al., 2020b; Pokharel and Lidar, 2024; Yamamoto et al., 2024). These encoded applications include using the [[4,2,2]] QED code with the variational quantum eigensolver (VQE) algorithm and Grover's search algorithm, respectively (Urbanek et al., 2020b; Pokharel and Lidar, 2024). The former demonstrated the use of the [[4,2,2]] code to encode a two-qubit ansatz for molecular hydrogen for the VQE algorithm (Urbanek et al., 2020b). The study showed improvement in accuracy of the ground state expectation value of the encoded hydrogen ansatz across the potential energy surface when compared to the unencoded simulation on an IBM 5Q quantum computing device. The encoding uses a circuit construction introduced in (Gottesman, 2016) that uses an ancilla and a destructive parity measurement to construct state preparation circuits for certain specific input states using the [[4,2,2]] error detection code such that the qubits are fault tolerantly protected.

In this work, we build upon the results in (Urbanek et al., 2020b), by (i) studying the different post-selection methods individually and in comparison with the unencoded ansatz, and (ii) quantitatively evaluating the trade-off between the probability of success and the accuracy of the estimated energy for each method. We perform our analysis using numerical simulations under a standard depolarizing noise model and report results for a single internuclear distance. We estimate the energy expectation value of the ground state of molecular hydrogen using the VQE algorithm with a [[4,2,2]] encoded ansatz for each post-selection method and calculate the precision (variance and standard error of the mean) of the estimate with increasing depolarizing noise.

Here, we use ‘chemical accuracy’ as a useful benchmark to evaluate error estimates in applications of computational chemistry. Chemical accuracy is defined in practice to be within 1.6mHa of the full configuration interaction (FCI) energy for the chosen basis set and is necessary for making reliable predictions about the properties derived from these estimates, such as atomization energies and reaction enthalpies (Cao et al., 2019b). Many studies have reported energy estimates close to or within chemical accuracy for molecular hydrogen using VQE(Colless et al., 2018b,a; O’Malley et al., 2016). We estimate the error rate at which chemical accuracy is possible when using this encoding in comparison to the unencoded simulation in the presence of single- and two-qubit gate depolarizing errors. Additionally, we present an error analysis for each post-selection method using density-matrix simulations and fidelity calculations to elucidate on the advantages and disadvantages of using this specific circuit construction for the [[4,2,2]] error detection code.

5.2 VQE for Chemical Accuracy

This section presents an overview of the VQE algorithm for estimating the energy of a molecular Hamiltonian with chemical accuracy. We then review how to apply the encoding methods defined by the [[4,2,2]] code to prepare the underlying circuit for creating the variational anstaz state before discusing methods to post-process the detection outcomes.

5.2.1 Molecular Electronic Hamiltonian

The central problem of electronic structure theory is to find the ground state of a molecule by finding the lowest eigenvalue of the electronic Hamiltonian. We start with the molecular Hamiltonian in first quantized form:

$$\hat{H}_{\mathrm{mol}} = -\sum_i \frac{\nabla^2_{R_i}}{2M_i} - \sum_i \frac{\nabla^2_{r_i}}{2m_i} - \sum_{i,j} \frac{Z_i}{|R_i - r_j|} + \sum_{i,j>i} \frac{Z_i Z_j}{|R_i - R_j|} + \sum_{i,j>i} \frac{1}{|r_i - r_j|} \tag{5.1}$$

where R_i and r_i are the positions of the ith nuclei and electron, respectively, M_i, m_i their respective masses and Z_i the charge of the nuclei. Under the Born-Oppenheimer approximation, the nuclei are treated as classical point charges due to the large difference in mass between the nucleus and electron. This leads to an electronic Hamiltonian with coefficients that are a function of the internuclear geometry, R and is represented in the second quantized form as:

$$H(R) = \sum_{pq} h_{pq} a_p^\dagger a_q + \frac{1}{2} \sum_{pqrs} h_{pqrs} a_p^\dagger a_q^\dagger a_r a_s \tag{5.2}$$

where $a_p^\dagger$ and a_q are creation and annihilation operators and follow the cannonical fermionic anti-commutation relations:

$$\begin{aligned} \{a_p^\dagger, a_q\} &= \delta_{pq} \\ \{a_p, a_q\} &= 0 \end{aligned} \tag{5.3}$$

and h_{pq} and h_{pqrs} are one- and two-electron integrals classically computed as

$$h_{pq} = \int d\sigma \varphi_p^*(\sigma) \left(\frac{\nabla_r^2}{2} - \sum_i \frac{Z_i}{|R_i - r|} \right) \varphi_q(\sigma) \tag{5.4}$$

and

$$h_{pqrs} = \int d\sigma_1 d\sigma_2 \frac{\varphi_p^*(\sigma_1)\varphi_q^*(\sigma_2)\varphi_s(\sigma_1)\varphi_r(\sigma_2)}{|r_1 - r_2|} \tag{5.5}$$

where σ encodes the position and spin.

In the case study below, we estimate the ground state energy of the hydrogen molecule using VQE. The Hamiltonian in the minimal STO-3G basis can be presented in a two-qubit representation that considers only the spin singlet configuration (Whitfield et al., 2011b). The molecular orbitals $|\psi_u\rangle$ and $|\psi_g\rangle$ are given as linear combinations of the respective atomic orbitals, leading to spin orbitals $|\Psi_i\rangle$ each with spin α or β (Shee et al., 2022; Romero et al., 2018b), as

$$|\psi_g\rangle = |\psi_1\rangle + |\psi_2\rangle \tag{5.6a}$$

$$|\psi_u\rangle = |\psi_1\rangle - |\psi_2\rangle \tag{5.6b}$$

$$|\Psi_0\rangle = |\psi_g(\alpha)\rangle \tag{5.7a}$$

$$|\Psi_1\rangle = |\psi_u(\alpha)\rangle \tag{5.7b}$$

$$|\Psi_2\rangle = |\psi_g(\beta)\rangle \tag{5.7c}$$

$$|\Psi_3\rangle = |\psi_u(\beta)\rangle \tag{5.7d}$$

Using a series of fermionic and spin transformations we arrive at the final Hamiltonian shown in equation 5.8. Details of the transformations are presented in Appendix 5.7.

$$H(R) = g_0 I + g_1 Z_0 + g_2 Z_1 + g_3 Z_0 Z_1 + g_4 X_0 X_1 \tag{5.8}$$

5.2.2 Variational Quantum Eigensolver

The VQE algorithm is a leading quantum-classical hybrid algorithm for electronic structure calculations on near-term noisy intermediate scale quantum devices (NISQ) and has been extensively studied for simulations of small quantum chemistry problems (Peruzzo et al., 2014a; O'Malley et al., 2016; Romero et al., 2018b; Cao et al., 2019b; Nam et al., 2020; Grimsley et al., 2020; P et al., 2021; Zhang et al., 2022). The VQE algorithm is a method to estimate the minimal expectation value of a Hermitian operator with respect to a variable pure quantum state (Peruzzo et al., 2014a). The method itself is based on the variational principle from quantum mechanics, which asserts that only the lowest eigenstate, aka ground state, of a non-negative, hermitian operator minimizes the expectation value. Estimating the energy is then described by the optimization

$$E(\theta^\star) = \min_\theta \langle \psi(\theta) | H | \psi(\theta) \rangle \tag{5.9}$$

where $|\psi(\theta)\rangle = U(\theta)|\psi(0)\rangle$ is a variable pure quantum state prepared by a unitary ansatz operator $U(\theta)$ from the reference state $|\psi(0)\rangle$. The parameter $\theta^\star$ denotes the optimal value obtained from minimizing the energy. While the quantum operator or ansatz for preparing the quantum state can often be efficient relative to classical technique, the number of iterations required to reach the minimum energy is not guaranteed by the method and varies widely. Physically motivated ansatzes, such as ansatzes derived from Unitary Coupled Cluster (UCC) theory, often scale unfavourably in the number of gates with increasing system size while hardware efficient ansatzes (HWE) can suffer from optimization problems due to "barren-plateaus" (Cao et al., 2019b; Cerezo et al., 2021; Tilly et al., 2022). Improvement of the performance of the VQE algorithm by finding strategies to address the unfavourable scaling and classical optimization challenges is an active area of research(Zhang et al., 2022; Metcalf et al., 2020; Liu et al., 2019; Cerezo et al., 2021; Parrish et al., 2019; Zhang et al., 2021; Liu et al., 2024; Lim et al., 2024; Park, 2024; Matoušek et al., 2024).

When computing the electronic structure of molecules, the VQE reference state is often represented by the Hartree-Fock solution to the electronic Hamiltonian or some other mean-field approximation. In our encoding of the hydrogen molecule above, the Hartree-Fock state corresponds to the $|00\rangle$ state. In practice, the choice of the underlying unitary ansatz and the optimization routine play a significant role in whether the prepared quantum state approaches the true ground state of a molecule (Gowrishankar et al., 2021b; Wright et al., 2022).

We consider an ansatz based on UCC theory which derives from the well known coupled cluster methods in quantum chemistry (Romero et al., 2018b; Bartlett et al., 1989; Taube and Bartlett, 2006). To derive the UCC ansatz, we start by replacing operators from classical coupled cluster theory with unitary excitation operators. This results in an exponentiated sum of operators which can be approximated as a product of exponentiated operators using Trotterization resulting in a unitary coupled cluster operator (Suzuki, 1993; Trotter, 1959; Evangelista et al., 2019). The unitary operator approximated to the first Trotter step ($t = 1$) is shown in 5.10.

$$\begin{aligned} U(\theta) = e^{T(\theta)-T(\theta)^\dagger} &= e^{\sum_i \theta_i(\tau_i - \tau_i^\dagger)} \\ &\approx (\prod_i e^{\frac{\theta_i}{t}(\tau_i - \tau_i^\dagger)})^t \\ &\approx \prod_i e^{\theta_i(\tau_i - \tau_i^\dagger)} \end{aligned} \tag{5.10}$$

$$\begin{aligned} T(\theta) &= \sum_k T_K(\theta) \\ T_1 &= \sum_{q \in occ, p \in virt} \theta_q^p a_p^\dagger a_q \\ T_2 &= \sum_{r>s \in occ, p>q \in virt} \theta_{rs}^{pq} a_p^\dagger a_q^\dagger a_r a_s \end{aligned} \tag{5.11}$$

where T_k is the excitation operator manifold and θ_q^p and θ_{rs}^{pq} are singles and doubles amplitudes, respectively.

Considering only the contribution from T_2 we arrive at the unitary coupled cluster doubles (UCCD) ansatz shown in 5.12. The transformation leading to this operator is presented in Appendix 5.7.

$$U(\theta) = e^{-i\theta Y_0 X_1} \tag{5.12}$$

The circuit decomposition of 5.12 involves the subcircuit for the $e^{-i\theta Z_0 Z_1}$ operator surrounded by single qubit rotations to perform the transformation to $e^{-i\theta Y_0 X_1}$(Nielsen and Chuang, 2010b; Barenco et al., 1995). Some of the single qubit rotations in the decomposition are redundant for the initial Hartree-Fock input state, $|00\rangle$, in our encoding, and can be removed. This results in the two-qubit unencoded circuit shown in **Figure 5.1**, which prepares the final state, $|\chi(\theta)\rangle$, shown in 5.13.

$$|\chi(\theta)\rangle = cos\frac{\theta}{2}|00\rangle + sin\frac{\theta}{2}|11\rangle \tag{5.13}$$

We present results for the expectation value of the Hamiltonian at the internuclear distance of 0.74Å shown in 5.14, where the coefficients are obtained from (Colless et al., 2018a).

$$\begin{aligned} H = &-0.349833\ \mathbb{I} - 0.388748\ Z_0 - 0.388748\ Z_1 \\ &+ 0.0111772\ Z_0 Z_1 + 0.181771\ X_0 X_1 \end{aligned} \tag{5.14}$$

The analytical energy expectation value and optimal parameter for this Hamiltonian and ansatz are shown in 5.15.

$$\theta^* = -0.2297 \text{ rads} \tag{5.15a}$$

$$\langle \chi(\theta^*)|H|\chi(\theta^*)\rangle = -1.13712 \text{ Ha} \tag{5.15b}$$

5.2.3 [[4,2,2]] Quantum Error Detection Code

The [[4,2,2]] quantum error detection code, following the $[[n, k, d]]$ convention, is a distance $d = 2$ code that encodes $k = 2$ logical qubits using $n = 4$ physical qubits. The basis states for the logical codespace of this encoding are shown in 5.16 and the corresponding physical operations for each logical operation are described in **Table 5.1**.

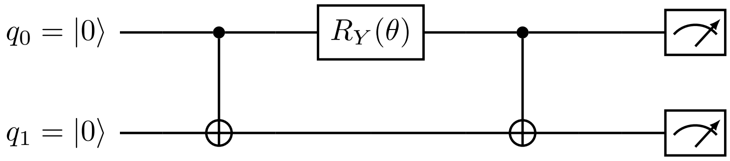

Figure 5.1: The unencoded two-qubit UCC single parameter VQE ansatz.

Table 5.1: Basis operations.

Basis Operations	
Logical Basis	Physical Basis
$X_1 \otimes I_2$	$X \otimes I \otimes X \otimes I$
$I_1 \otimes X_2$	$X \otimes X \otimes I \otimes I$
$Z_1 \otimes I_2$	$Z \otimes Z \otimes I \otimes I$
$I_1 \otimes Z_2$	$Z \otimes I \otimes Z \otimes I$
$H_1 \otimes H_2$	$H \otimes H \otimes H \otimes H$
$CNOT_{12}$	$SWAP_{12}$
$CNOT_{21}$	$SWAP_{13}$

$$
\begin{aligned}
\overline{|00\rangle} &= \frac{1}{\sqrt{2}}(|0000\rangle + |1111\rangle) \\
\overline{|10\rangle} &= \frac{1}{\sqrt{2}}(|0101\rangle + |1010\rangle) \\
\overline{|01\rangle} &= \frac{1}{\sqrt{2}}(|0011\rangle + |1100\rangle) \\
\overline{|11\rangle} &= \frac{1}{\sqrt{2}}(|0110\rangle + |1001\rangle)
\end{aligned} \tag{5.16}
$$

The code can detect at most one-single physical qubit bit flip and/or phase flip error (Pauli X or Z error, respectively) that occurs during the encoding of the initial state (Devitt et al., 2013). The circuit for the error detection or syndrome measurement for this encoding is presented in **Figure 5.2**. Ancillas s_X and s_Z are used for error syndrome measurement and detect bit flip and phase flip errors, respectively.

Since all the basis states of this encoding have even parity (even number of 1s in the physical basis), any single physical qubit bit flip error will take the state outside the logical codespace and result in a state with odd parity. As a result, a single physical qubit bit flip error will lead to a measurement of $s_X = 1$. If the state is rotated using the Hadamard ($H^{\otimes 4}$) operation before measurement, any single physical qubit phase flip error will lead to a measurement of $s_Z = 1$. Two physical qubit bit-flip errors take the state to another logical state and will remain undetected by the ancillas. Two physical qubit phase-flip errors can add a global phase to the state or leave the state effectively unchanged.

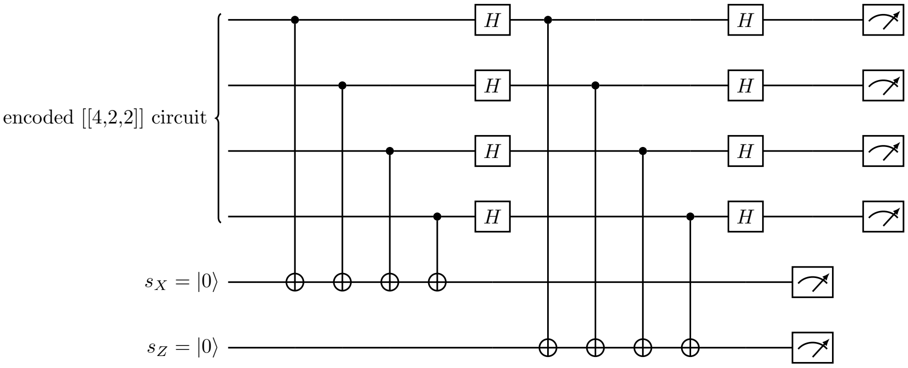

Figure 5.2: Syndrome measurement circuit for the [[4,2,2]] error detection code.

Another way to extract the error syndrome is by measuring all the data qubits and selecting measurements based on parity. Odd parity measurements indicate that a single qubit bit-flip error has occurred and is akin to performing the stabilizer measurement with ancilla s_X in **Figure 5.2**. Similarly, odd parity of measurements made after rotating the state by applying the Hadamard ($H^{\otimes 4}$) operation indicate that a physical qubit phase-flip error has occurred and is equivalent to an $s_Z = 1$ measurement in **Figure 5.2**. The advantage of this method over the stabilizer measurement is the reduction in the number of two-qubit gates for syndrome detection. The disadvantage is that the detection of errors requires a destructive measurement and only allows detection of one of the two types of errors, a physical bit flip or phase flip error.

This alternate method can be coupled with an ancilla for additional error detection during state preparation. This is applicable only to certain specific input logical states, $|\overline{00}\rangle, |\overline{0+}\rangle, |\overline{00}\rangle + |\overline{11}\rangle$ and can be used during the preparation of the Hartree-Fock initial state, $|\overline{00}\rangle$, in this study(Gottesman, 2016). The ancilla detects physical qubit bit-flip errors during preparation of the input state while the parity check measurement described earlier enables detection of single physical qubit bit or phase flip errors.

5.3 Simulated Encoding Methods

In this section, we present details on the methods to encode the VQE algorithm and UCCD ansatz using the [[4,2,2]] code. We also review the methods used to simulate and post-process results for the electronic Hamiltonian of molecular hydrogen in the presence of circuit noise.

5.3.1 [[4,2,2]] Encoding of the UCC Ansatz

We transform the two-qubit Hamiltonian in 5.14 into the corresponding encoded, four qubit Hamiltonian shown in 5.17 using the mapping in **Table 5.1**. The corresponding [[4,2,2]] encoding of the parameterized UCC two-qubit ansatz shown for simulating the hydrogen molecule is presented in **Figure 5.3** (Urbanek et al., 2020b). The first block on the left, labeled "STATE PREP", represents the circuit to prepare the initial logical $|00\rangle$ state of the unencoded ansatz and can be prepared in a wide variety of ways(Gottesman, 2016; Urbanek et al., 2020b; Vuillot, 2017). The second block labeled,"UCC Ansatz", represents the execution of the UCC ansatz in the [[4,2,2]] encoding (Urbanek et al., 2020b). The parameterized rotation gate in the ansatz is non-transversal in this encoding and therefore, an ancilla, a_2, is used to teleport the gate. The final state following the action of the paramatrized unitary operator corresponding to the unencoded ($|\chi(\theta)\rangle$) and encoded circuit ($|\psi_{enc}(\theta)\rangle$) is shown in 5.18.

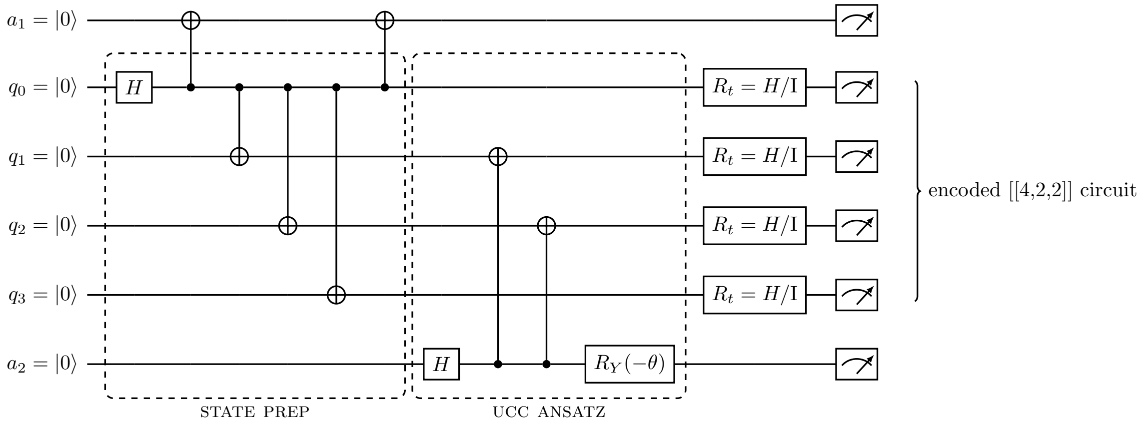

Figure 5.3: The [[4,2,2]] encoded ansatz for the hydrogen molecule. The block labeled 'STATE PREP' describes the circuit to prepare the initial state in the [[4,2,2]] encoding. The block labeled 'UCC ansatz' describes the implementation of the UCC derived hydrogen VQE ansatz in the [[4,2,2]] encoding. $R_t = H/I$ indicates the basis of the state prior to measurement, in the X or computational basis, respectively.

$$H_{physical} = g_0 I + g_1 Z_0 Z_1 + g_2 Z_0 Z_2 + g_3 Z_1 Z_2 + g_4 X_1 X_2 \tag{5.17}$$

$$|\chi(\theta)\rangle = cos\frac{\theta}{2}|00\rangle + sin\frac{\theta}{2}|11\rangle \tag{5.18a}$$

$$\begin{aligned} |\psi_{enc}(\theta)\rangle = \frac{1}{\sqrt{2}}[(|0\rangle_{a_1} \otimes (cos\frac{\theta}{2}|\overline{00}\rangle_{q_0-q_3} + sin\frac{\theta}{2}|\overline{11}\rangle_{q_0-q_3}) \otimes |0\rangle_{a_2}) \\ + (|0\rangle_{a_1} \otimes (cos\frac{\theta}{2}|\overline{11}\rangle_{q_0-q_3} - sin\frac{\theta}{2}|\overline{00}\rangle_{q_0-q_3}) \otimes |1\rangle_{a_2}))] \end{aligned} \tag{5.18b}$$

The action of this non-transversal gate in the encoded circuit results in a uniform superposition of equivalent states, each representing the unencoded final state, with equal probability to be in $a_2 = |0\rangle$ or $|1\rangle$, and with each minimizing the expectation value at a different parameter. The optimal parameter, $\theta^* = \theta$, at $a_2 = |0\rangle$, is shifted by π to $\theta^* = \theta \pm \pi$ when $a_2 = |1\rangle$. For the purpose of calculating expectation values, we only use outcomes with $a_2 = |0\rangle$ resulting in the final state shown in 5.19. This excludes $\sim 50\%$ of the total number of outcomes measured, belonging to the subset with $a_2 = |1\rangle$, from our calculations. The corresponding state for $a_2 = |1\rangle$ is shown in 5.20.

$$\begin{aligned} |\psi_{enc}^{a_2=0}(\theta)\rangle &= \frac{(\mathbb{I}^{\otimes 5} \otimes |0\rangle\langle 0|_{a_2}) \otimes (|\psi_{enc}(\theta)\rangle)}{\sqrt{(\langle\psi_{enc}(\theta)|0\rangle\langle 0|_{a_2}\psi_{enc}(\theta)\rangle)}} \\ &= |0\rangle_{a_1} \otimes (cos\frac{\theta}{2}|\overline{00}\rangle_{q0-q_3} + sin\frac{\theta}{2}|\overline{11}\rangle_{q_0-q_3}) \otimes |0\rangle_{a_2} \end{aligned} \tag{5.19}$$

$$|\psi_{enc}^{a_2=1}(\theta)\rangle = |0\rangle_{a_1} \otimes (cos\frac{\theta}{2}|\overline{11}\rangle_{q_0-q_3} - sin\frac{\theta}{2}|\overline{00}\rangle_{q_0-q_3}) \otimes |1\rangle_{a_2} \tag{5.20}$$

For expectation value calculations, since each Pauli term in the Hamiltonian in 5.17 is in a single basis, X or Z, we measure the final state of the encoded ansatz in the computational basis and rotate the state using the Hadamard operation prior to measurement for the "X_0X_1" term. This is shown in **Figure 5.3** as $R_t = H$ for the "X_0X_1" Pauli term or $R_t = I$ for terms in the computational basis, prior to measurement.

5.3.2 Numerical Model and Simulations

We use the XACC framework to run the numerical simulations of the VQE algorithm. XACC is a software framework for the development of hardware-agnostic programs for quantum-classical hybrid algorithms, and their implementation on near-term quantum hardware (McCaskey et al., 2020; Daniel et al., 2022) . We use the IBM Aer simulator within XACC for numerically simulating each ansatz and use brute force optimization by scanning 150 values of parameter $\theta \in [-\pi, \pi]$.

We model gate noise with a depolarizing error channel given as

$$\xi_j^G(\rho) = (1-p)\rho' + p\sum_k \sigma_j^k \rho' \sigma_j^k \tag{5.21}$$

where $\rho' = G\rho G^\dagger$, G is any single-qubit gate in the circuit acting on qubit j in density matrix ρ, $\sigma_j \in \{X_j, Y_j, Z_j\}$, and p is the noise parameter. Errors on a two-qubit gate acting on qubits i and j are modeled as $\xi_{i,j}^G(\rho) = \xi_i^I(\xi_j^G(\rho))$ with I the identity. The noise parameter for the two-qubit gate is an order of magnitude higher than the single-qubit noise parameter as is typical in current devices. The errors resulting from this channel are single qubit errors, E_j on qubit j or two qubit errors $E_i \otimes E_j$ on qubits, i and j for $E_k \in \{X_k, Y_k, Z_k, \mathbb{I}_k\}$.

We calculate the energy expectation values for both the unencoded and encoded simulations and for each post-selection method, using $N = 2 \times 10^6$ shots, which we determined by calculating the shot count required to estimate the energy within standard error of the mean (SEM) of 0.5mHa for a noiseless simulation. The SEM,

σ, is calculated as:

$$\sigma_{E(\theta^*)} = \sqrt{\frac{var}{N}} \tag{5.22}$$

where N is the number of shots and var is the variance of the calculation. The variance is calculated as,

$$\begin{aligned} var &= \sum_i g_i^2(\langle P_i^2 \rangle - \langle P_i \rangle^2) \\ &= \sum_i g_i^2(1 - \langle P_i \rangle^2) \end{aligned} \tag{5.23}$$

where, P_i is the ith Pauli term of the Hamiltonian and g_i is the coefficient of the ith Pauli term. We analytically calculated the variance of the Hamiltonian to be 0.04700 Ha^2 by using the expectation value of each Pauli term in 5.14. We found the number of shots required to reach our target SEM of 0.5 mHa as shown in 5.24

$$\begin{aligned} N &= \frac{var}{\sigma^2_{E(\theta^*)}} \\ &= \frac{0.04700}{0.0005^2} \\ &= 188000 \end{aligned} \tag{5.24}$$

and rounded up to result in $N = 2 \times 10^6$ shots.

Post-Selection Strategies

We introduce and analyze several different post-selection strategies. We post-select outcomes from the measurement bitstrings once all qubits are measured. The expectation values of each Pauli term in the Hamiltonian are estimated from the available, post-selected measurements. Measurement of ancilla, $a_1 = 1$ indicates a bit flip error has occurred on qubit q_0. As a result, for post-selection by ancilla a_1 (PSA) measurement, we discard all measurements with $a_1 = 1$.

Since measurements of the encoded qubits/data qubits with odd parity indicate a single physical qubit bit or phase flip error, for post-selection by logical state parity (PSP), we discard measurement bitstrings that have odd parity but include measurement counts with both measurements of ancilla, $a_1 = 0$ and $a_1 = 1$. We also consider a post-selection strategy labeled PSAP that combines both the PSA and PSP strategies. In this post-selection method, we discard measurement outcomes that have odd parity or ancilla, $a_1 = 1$.

We also calculate the SEM for the energy estimated from each post-selection method by modifying 5.22 to be:

$$\sigma_{E(\theta^*)} = \sqrt{\frac{var}{n}} \tag{5.25}$$

where n is the number of samples retained after each post-selection method.

Probability of Success

We report on the probability of success (η) for each post-selection strategy. We define it as the fraction of samples that are retained after each post-selection method.

$$\eta = \frac{n}{N} \tag{5.26}$$

The SEM for the resulting binomial distribution for each post-selection method is calculated as

$$\sigma_\eta = \sqrt{\frac{(1-\eta)(\eta)}{N}} \tag{5.27}$$

where n is the number of the samples after post-selection for each method, N is the number of samples with $a_2 = 0$.

Logical Fidelity

We calculate the logical fidelity of the prepared states as generated by the noisy circuit simulations. We simulate the two-qubit UCCD ansatz state for the hydrogen molecule and the corresponding [[4,2,2]] encoded circuit described in **Figure 5.1** and **Figure 5.3**, respectively. With the resulting final state for the encoded circuit shown in 5.19 we use projection operators to assess the impact of each post-selection technique using fidelity. We calculate the fidelity for the PSA method by using operators, Π_A, to project states from the noisy state with ancilla, $a_1 = |0\rangle$ and identity ($\mathbb{I}$) for all other qubits. For the PSP strategy, we project states within the codespace, i.e., within the states in 5.16, using operators Π_P. And we use the operator, Π_{AP} for projecting states with $a_1 = |0\rangle$ and states within the codespace. The operators are shown in 5.28 and presented in expanded form in Appendix 5.7.

$$\Pi_A = |0\rangle\langle 0|_{a_1} \otimes |\mathbb{I}_0\mathbb{I}_1\mathbb{I}_2\mathbb{I}_3\rangle\langle\mathbb{I}_0\mathbb{I}_1\mathbb{I}_2\mathbb{I}_3| \otimes |0\rangle\langle 0|_{a_2=0} \tag{5.28a}$$

$$\begin{aligned}\Pi_P = \mathbb{I}_{a_1} \otimes (&|\overline{00}\rangle\langle\overline{00}|_{q_0-q_3} + |\overline{01}\rangle\langle\overline{01}|_{q_0-q_3} \\ &+ |\overline{10}\rangle\langle\overline{10}|_{q_0-q_3} + |\overline{11}\rangle\langle\overline{11}|_{q_0-q_3}) \otimes |0\rangle\langle 0|_{a_2=0}\end{aligned} \tag{5.28b}$$

$$\Pi_{AP} = \Pi_A \otimes \Pi_P \tag{5.28c}$$

We calculate the logical fidelity of the states projected using operators Π_A, Π_P, Π_{AP}, and the original encoded and unencoded states. We define the fidelity F between two states ρ_1 and ρ_2 as

$$F(\rho_1, \rho_2) = (\mathrm{Tr}\sqrt{\sqrt{\rho_2}\rho_1\sqrt{\rho_2}})^2 \tag{5.29}$$

Here, we consider the case that $\rho_1 = |\Psi\rangle\langle\Psi|$, $|\Psi\rangle$ is the expected ground state, i.e., the noiseless state, from the noise-free simulation and ρ_2 is the representation of the prepared, noisy unencoded, encoded or projected state. The fidelity of the projected state, F_i, is given as:

$$F_i(\rho_1, \rho_i) = (\mathrm{Tr}\sqrt{\sqrt{\rho_i}\rho_1\sqrt{\rho_i}})^2 \tag{5.30}$$

where $\rho_i = \frac{\Pi_i \rho_{\text{noisy}} \Pi_i^\dagger}{\mathrm{Tr}(\Pi_i \rho_{\text{noisy}} \Pi_i^\dagger)}$ is the projected state, ρ_{noisy} is the noisy encoded state, and $\Pi_i \in \{\Pi_A, \Pi_P, \Pi_{AP}\}$. We also calculate the minimum expectation value of energy for the state ρ as

$$E(\theta^*) = \mathrm{Tr}(H\rho(\theta^*)) \tag{5.31}$$

which represents an estimate in the limit of infinite samples of the measured state.

Logical Errors

We define logical error (p_ϵ) for the encoded circuit in **Figure 5.3** as probability of any error that takes the target or ideal encoded logical state to a different encoded logical state. We restrict the calculation to states with $a_2 = 0$. Therefore the logical error is the probability of measuring any state within the codespace shown in 5.16 other than the state $|\psi_{enc}^{a_2=0}(\theta^*)\rangle$ shown in 5.19.

We first calculate the probability to measure the ideal state, p_{ideal}, in the noisy mixed state, ρ_{noisy}, and the probability to measure any logical state, i.e., any state in the codespace described in 5.16.

$$p_{\text{ideal}} = \mathrm{Tr}(\rho_{\text{noisy}} \rho_{\text{ideal}}) \tag{5.32a}$$

$$p_{\text{logical}} = \mathrm{Tr}(\Pi_P \rho_{\text{noisy}}) \tag{5.32b}$$

From these we find the probability of any error ($p_{\epsilon_{all}}$) and probability of any non-logical error ($p_{\epsilon_{NL}}$), which is any error, single- or multi-qubit, that takes the target or ideal state, ρ_{ideal}, outside the codespace described in 5.16.

$$p_{\epsilon_{all}} = 1 - \mathrm{Tr}(\rho_{\text{noisy}} \rho_{\text{ideal}}) \tag{5.33a}$$

$$p_{\epsilon_{NL}} = 1 - p_{\text{logical}} \tag{5.33b}$$

The probability of any logical error to occur, p_{ϵ_L}, is then obtained by subtracting the probability of any non-logical error from the probability of any error as shown in

5.34.

$$\begin{aligned} p_{\epsilon_L} &= p_{\epsilon_{all}} - p_{\epsilon_{NL}} \\ &= \mathrm{Tr}(\rho_{\text{noisy}}\Pi_P) - \mathrm{Tr}(\rho_{\text{noisy}}\rho_{\text{ideal}}) \end{aligned} \tag{5.34}$$

We additionally calculate the impact of PSA on the logical error by replacing Π_P in 5.32b with Π_{AP} and find probability of logical error p_{ϵ_A} in this case as:

$$p_{\epsilon_A} = \mathrm{Tr}(\Pi_{AP}\rho_{\text{noisy}}) - \mathrm{Tr}(\rho_{\text{noisy}}\rho_{\text{ideal}}) \tag{5.35}$$

5.3.3 Circuit Error Analysis

While the errors detected by the PSP method are straightforward, in that, the method detects single physical qubit bit-flip or phase-flip error, the errors detected by the ancilla, a_1, in the PSA and PSAP methods are not as clear. We analyze the errors in this circuit construction under the standard depolarizing error model we have considered to elucidate on the errors discarded when the PSA or the PSAP method is used.

Errors under the depolarizing noise model we have considered include one- and two-qubit gate errors of the form E_i on qubit q_i and $E_i \otimes E_j$ on qubits q_i, q_j, respectively. Additionally, $CNOT$ gates generate two-qubit correlated errors such as a bit-flip error on the control qubit will result in a bit-flip error in the target qubit. The effective error ($E_k^{'}$) after a CNOT operation is applied on control qubit, i and target qubit j after an error has occurred on one of the qubits can be represented as $U_{ij}E_k|q_iq_j\rangle = E_k^{'}U_{ij}|q_iq_j\rangle$ where $U_{ij} = CNOT_{ij}$ is the ideal operation and $E_k^{'} = U_{ij}E_kU_{ij}^{\dagger}$ for $k \in \{i, j\}$. Multi-qubit errors of the form $E_1 \otimes E_2 \otimes E_3 \otimes E_4$ for $E_k \in \{X, Y, Z\}$ may also arise from concurrent one-qubit noise processes occurring on multiple qubits or from propagation of error under the two-qubit error model.

During the [[4,2,2]] input state encoding, or the section labeled "STATE PREP" in **Figure 5.3** and shown explicitly in **Figure 5.4**, the ancilla qubit a_1 is entangled with the data qubit q_0. Any bit-flip error $E_0 \in \{X_0, Y_0\}$ that occurs on qubit q_0, and effectively remains a bit-flip error after the last two-qubit CNOT gate from control q_0 to target q_3, labeled $E_{eff} \in \{X, Y\}$ in **Figure 5.4**, will result in a measurement outcome for ancilla $a_1 = 1$ and indicate that an error has occurred. However, a similarly occurring phase-flip error on q_0 will not impact the ancilla, a_1 and therefore, will remain undetected.

Since the "STATE PREP" section is dominated by two-qubit CNOT gates, there's a high likelihood of two-qubit errors occurring in that section. Additionally, these errors may cascade into multi-qubit errors with each successive CNOT gate execution as represented in **Figure 5.4**. As a result, the discarding of the errors by ancilla a_1 while effected by detection of bit-flip errors on q_0, may inadvertently remove multi-qubit errors as well. Construction of the circuit such that all the CNOT gates originate at q_0 with q_0 as the control ensures that many, if not most, two-qubit errors will impact q_0. Entangling the ancilla a_1 to this qubit q_0 enables the additional detection of errors that impact more than a single qubit. Conversely, the errors that do not affect q_0 in this "STATE PREP" section will not be detected by a_1 but the likelihood of such errors is low.

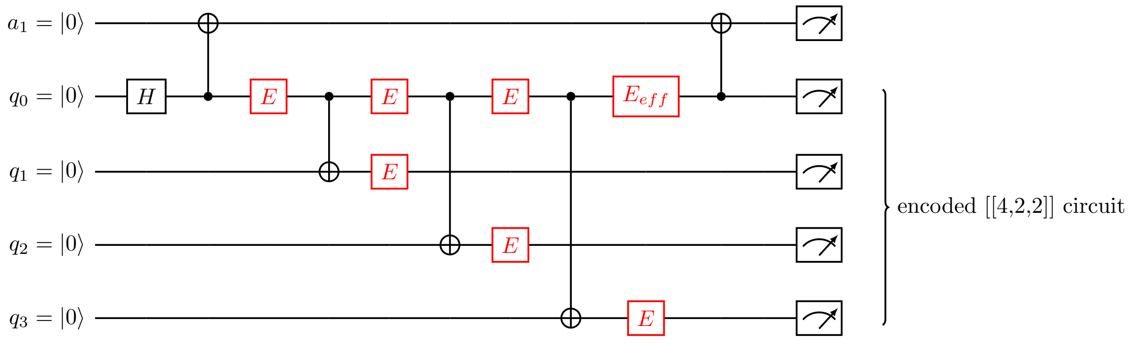

Figure 5.4: Logical $|\overline{00}\rangle$ state preparation circuit for error analysis. Errors, $E \in \{X, Y, Z\}$, that can occur in the input state preparation circuit, locations are representative. Ancilla $a_1 = 1$ if $E_{eff} \in \{X, Y\}$.

To verify whether the detection of error events by ancilla a_1 indeed enables multi-qubit error detection, we study the input logical state, $|\overline{00}\rangle$, prepared under the depolarizing noise channel immediately after the disentangling CNOT on the ancilla, a_1, which is the circuit labeled "STATE PREP" in **Figure 5.1** and shown explicitly in **Figure 5.4**. We calculate the contribution towards improvement in fidelity of each post-selection method at this initial stage, when errors detected by each method are for the same final state, $|\overline{00}\rangle$, as opposed to the circuit with the UCC ansatz where the PSA method is used to detect errors during initial input state preparation and PSP at the end of the circuit. We run density matrix simulations of the circuit shown in **Figure 5.4** for preparing the encoded logical $|\overline{00}\rangle$ state $|\phi\rangle$ shown in 5.36 with increasing depolarizing noise and use operators to project states similar to those in 5.28. Since this circuit does not include the ancilla a_2, the projection operators differ slightly and are presented in 5.37. We calculate the fidelity corresponding to each post-selection method by projecting states (i) with $a_1 = |0\rangle$, (ii) within the codespace, and (iii) both within the codespace and with $a_1 = |0\rangle$, using projection operators, S_A, S_P, and S_{AP}, respectively. We use 5.30 to calculate fidelity, F_{S_i}, of the projected states where, in this case, $\rho_1 = |\phi\rangle\langle\phi|$ is the noiseless state, $\rho_i = \frac{S_i \rho_{noisy} S_i^\dagger}{\mathrm{Tr}(S_i \rho_{noisy} S_i^\dagger)}$ for $S_i \in \{S_A, S_P, S_{AP}\}$ are the projected states and ρ_{noisy} is the noisy encoded input state.

$$\begin{aligned} |\phi\rangle &= |a_1\rangle \otimes |\overline{00}\rangle \\ &= |0\rangle \otimes \frac{1}{\sqrt{2}}(|0000\rangle + |1111\rangle) \end{aligned} \tag{5.36}$$

$$S_A = |0\rangle\langle 0|_{a_1} \otimes |\mathbb{I}_0\mathbb{I}_1\mathbb{I}_2\mathbb{I}_3\rangle\langle \mathbb{I}_0\mathbb{I}_1\mathbb{I}_2\mathbb{I}_3| \tag{5.37a}$$

$$\begin{aligned} S_P = \mathbb{I}_{a_1} \otimes (&|\overline{00}\rangle\langle\overline{00}|_{q_0-q_3} + |\overline{01}\rangle\langle\overline{01}|_{q_0-q_3} \\ &+ |\overline{10}\rangle\langle\overline{10}|_{q_0-q_3} + |\overline{11}\rangle\langle\overline{11}|_{q_0-q_3}) \end{aligned} \tag{5.37b}$$

$$S_{AP} = S_A \otimes S_P \tag{5.37c}$$

The key comparison to understand the contribution of ancilla, a_1, is between the fidelity F_{S_P} and $F_{S_{AP}}$ of states projected by S_P and S_{AP}, respectively. Once the single qubit bit-flip errors are projected out of the prepared logical $|\overline{00}\rangle$ state, using S_P, any improvement in fidelity due to projection by S_{AP} is entirely due to the contribution of ancilla a_1 and due to detection of multi-qubit error events.

5.4 Results

The [[4,2,2]] encoded VQE circuit shown in **Figure 5.3** and the unencoded circuit shown in **Figure 5.1** were simulated using the IBM 'aer' simulator with $N = 2 \times 10^6$ shots under a standard depolarizing noise model. All qubits were measured and the measurement counts were used to calculate expectation values of the Hamiltonian for the unencoded circuit, and the encoded circuit before and after post-selection. We find the threshold of depolarizing noise at which the energy estimates fall within the chemical accuracy benchmark, present the change in energy estimates with increasing two-qubit gate noise and calculate probability of success after each post-selection strategy. We simulated the exact state for both the encoded and unencoded ansatzes using the IBM 'aer' density-matrix simulator to calculate the logical fidelity, and in the case of the encoded ansatz, the logical error as well. We also calculate the energy expectation values from the exact state.

The energy expectation values, variance of the calculation and probability of success at the noise parameter value at which the energy estimate reached chemical accuracy ($p = 0.09\%$) are presented in **Table 5.2**. The PSAP method reaches chemical accuracy at the highest noise parameter value of 0.09% than all other methods. Without post-selection, the energy of the encoded ansatz is much higher than the unencoded ansatz and the exact energy of -1.13712 Ha. PSA improves the energy of the encoded ansatz while still falling short of the unencoded ansatz by 0.2% and PSP leads to a lower energy than PSA and the unencoded ansatz.

Table 5.2: Comparing outcomes of the numerical simulations of the unencoded and [[4,2,2]] encoded ansatzes with and without post-selection at 0.09% depolarizing noise parameter value and $N = 2 \times 10^6$ shots.

	Energy (mHa)	**Variance (mHa)**	**Prob. of Success (%)**
Unencoded	-1134.81 ± 0.52	5.38	100
Encoded No PS	-1131.40 ± 0.72	5.10	100
PSA	-1132.88 ± 0.71	4.99	99.644 ± 0.002
PSP	-1134.87 ± 0.70	4.84	99.472 ± 0.002
PSAP	-1135.89 ± 0.69	4.76	99.232 ± 0.003

The combined method, PSAP, leads to the highest improvement in the accuracy of the energy estimate and brings the energy estimate within chemical accuracy of 1.6 mHa.

The energy estimates from $N = 2 \times 10^6$ shots at the lower end of the noise range considered are compared against the benchmark of chemical accuracy in **Figure 5.5** for all post-selection methods. The trends are similar to those observed in **Table 5.2**. The PSAP method is within chemical accuracy at noise parameters $\leq 0.09\%$ followed closely by the PSP method, which reaches chemical accuracy at $\leq 0.08\%$ noise. The trend continues even at larger noise values as shown in **Figure 5.6**. PSA improves the energy estimate over encoded ansatz simulation with no post-selection. However, it results in higher energy than the unencoded ansatz. PSP results in lower energy than both the encoded ansatz without post-selection and PSA. The results are also lower than the unencoded ansatz below noise level of 4%. Combining the two post-selection methods, PSAP results in the lowest energy and for all noise levels considered. Error bars in this plot of **Figure 5.6** are too small to be visible and are in the range $0.06 - 2.8$mHa.

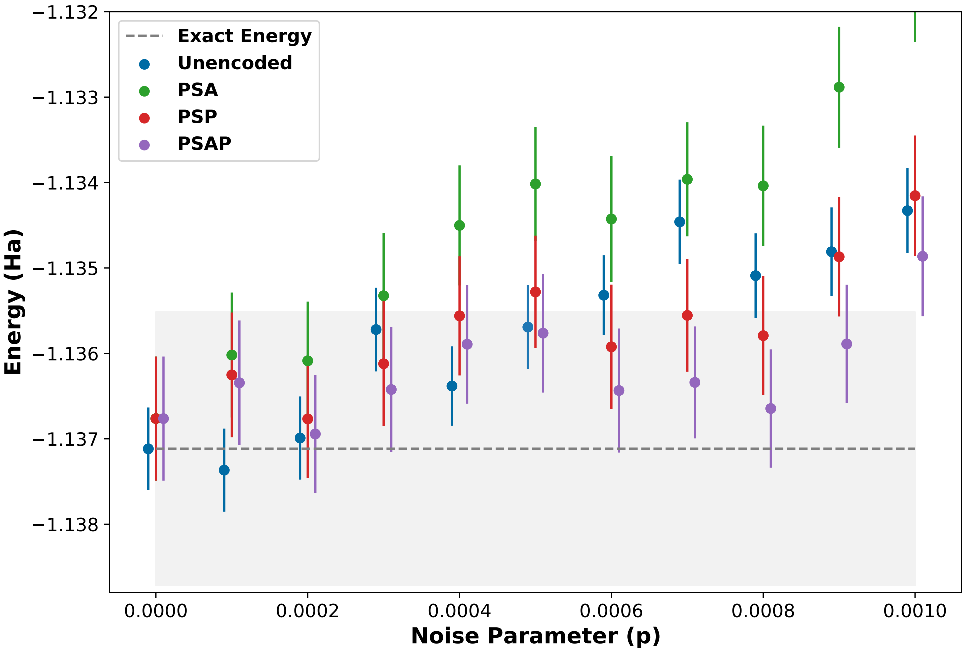

Figure 5.5: Estimated energy of post-selected outcomes and unencoded simulation compared against the benchmark of chemical accuracy. Shaded region represents the region of chemical accuracy and is set to ±1.6 mHa

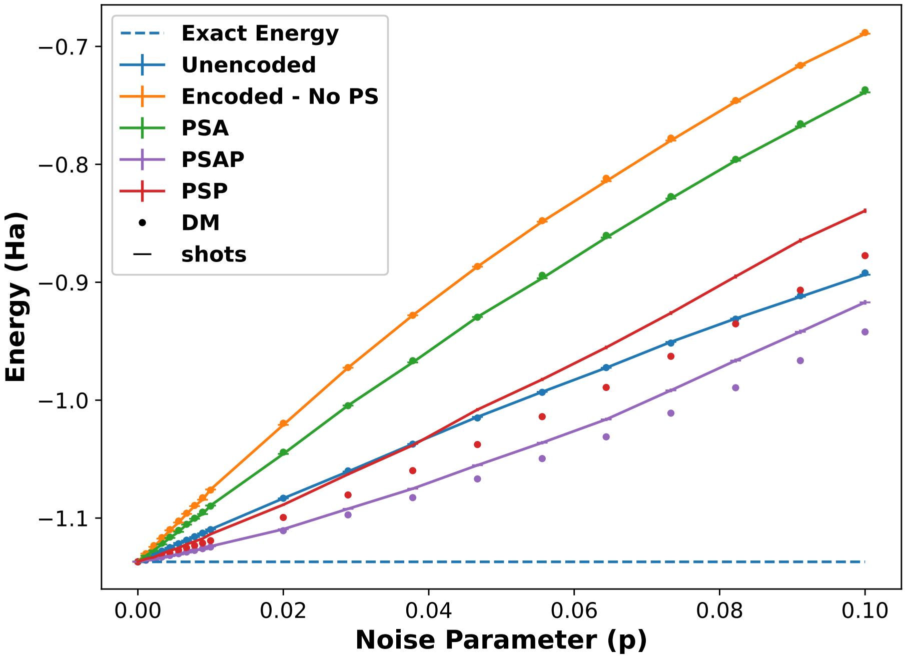

Figure 5.6: Energy expectation values calculated from numerical simulations of the unencoded and [[4,2,2]] encoded ansatz without (No PS) and with post-selection methods, PSA, PSP and PSAP with increasing two-qubit gate noise at 200000 shots using the IBM aer simulator and a standard depolarizing noise model.

We also present expectation value calculations using the exact density matrix for all simulations with increasing two-qubit gate noise in **Figure 5.6**. Since calculations using the exact density matrix represent estimates of the energy in the limit of infinite shots, the energy estimate from the simulations with finite number of shots should agree with the exact density matrix calculations within some standard deviation. They are in agreement for all simulations except the calculations for the PSP and PSAP method. For both methods, energy estimated from simulations with shots is higher than calculations using the exact density matrix.

The consequence of post-selection is having fewer samples for calculating energy expectation values. In all cases, including the noiseless case, since we are only considering half of the samples from the uniform superposition of the final state due to non-transversal rotation by ancilla a_2, i.e., only samples with $a_2 = |0\rangle$, we start with $\sim 50\%$ of the original number of shots prior to implementation of any post-selection method due to detection of errors. We present the change in probability of success after each post-selection method with increasing noise in **Figure 5.7**, and in **Table 5.2**, for a specific noise parameter value, normalized after selecting samples with $a_2 = |0\rangle$.

For all post-selection methods, the probability of success decreases with increasing noise indicating an increasing proportion of states with detected errors. This proportion is also determined by the method of post-selection. Post-selection by ancilla, $a_1 = 0$, measurement, PSA, retains the highest proportion of samples. However, energy expectation value calculations indicate that this does not lead to an improvement over the unencoded ansatz. Post-selection by logical state parity, PSP, results in a lower probability of success than PSA, while the highest proportion of samples are discarded due to the combined post-selection method, PSAP. Standard error of the mean in the figure are too small in magnitude to be visible but range from 0.01% (0.006% for 0.01% noise) to 0.2%. There's also a difference in the probability of success depending on the Pauli term being measured as shown in **Figure 5.7**. Probability of success for X Pauli term measurements are slightly lower than for Z Pauli term measurements due to additional noise in the circuit from the Hadamard gates used to rotate the state prior to making the measurement. The PSAP X and Z Pauli term plots are representative and apply to all other post-selection methods.

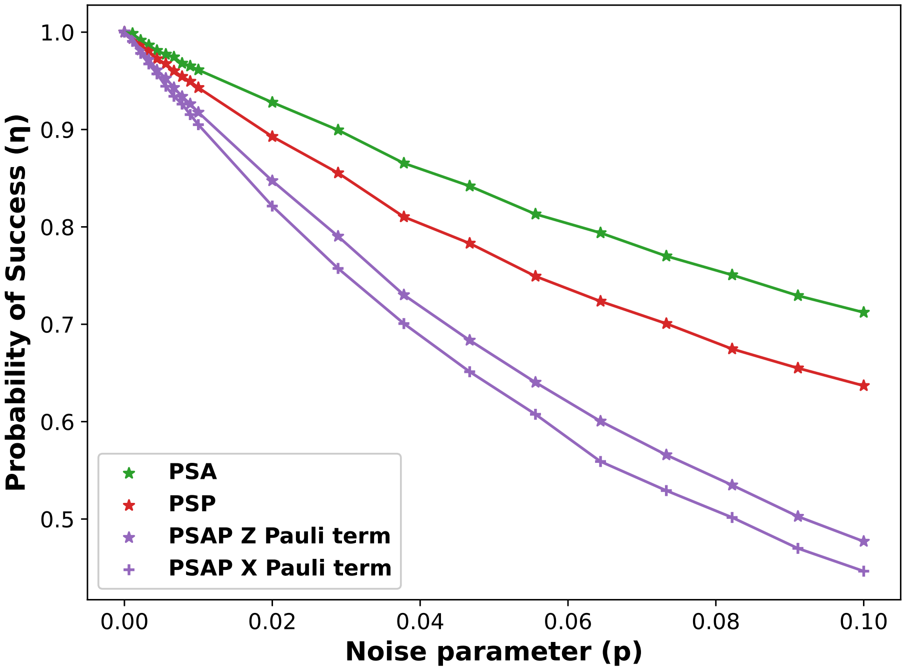

Figure 5.7: Probability of success of each post-selection method, PSA, PSP and PSAP of the [[4,2,2]] encoded ansatz under a standard depolarizing model. PSAP X and Z Pauli term plots are representative of the post-selection outcomes for circuits with and without the Hadamard rotation applied prior to measurement on all the encoded qubits ($q_0 - q_3$) in **Figure 5.3**, respectively. Trends between the two Pauli terms are similar for all post-selection methods.

The number of samples retained consequently impact the precision of the calculation. **Table 5.2** shows that there is a decrease in precision/ increase in standard error of the mean of the energy estimate from the encoded simulations with and without post-selection compared to the unencoded simulation. However, the variance of the calculation for the encoded post-selected calculations are lower than the unencoded simulations and lowest for PSAP calculation, which results in the highest accuracy of the energy estimate. The decrease in the SEM, therefore, is a result of considering only half the samples with ancilla $a_2 = 0$ measurement for the encoded ansatz which is not a consideration for the unencoded ansatz, where the full $N = 2 \times 10^6$ samples are included in the SEM calculation.

We now present the logical fidelity of the the unencoded state, and the encoded state, without and with projections $\Pi_i \in \{\Pi_A, \Pi_P, \Pi_{AP}\}$ corresponding with post-selection methods PSA, PSP and PSAP, respectively, with increasing two-qubit depolarizing noise p in **Figure 5.8**. The logical fidelity decreases with increasing noise, and changes with each post-selection strategy. The state fidelity of the unencoded ansatz, F_{unenc}, decreases with noise but is consistently better than the encoded state fidelity, F_{enc} even after projecting states based on the ancilla measurement using projector Π_A, as indicated by fidelity, F_A. A drastic improvement in fidelity is observed for states projected using projector Π_P. Not only is this fidelity, F_P, higher than the fidelity, F_A, it outperforms the fidelity of the unencoded state, F_{unenc}, up to a noise value of $\sim 2\%$. Combining the two post-selection methods results in the best fidelity, F_{AP}, for this circuit and is better than F_{unenc} for all noise parameters considered. Furthermore, overall decrease in fidelity of all cases with increasing noise in spite of projecting states against single- and multi-qubit errors is due to errors that go undetected in each projection, such as logical errors, introduced by the UCC ansatz or by combination of errors from state-preparation and UCC ansatz, that escaped detection by projection using Π_{AP}.

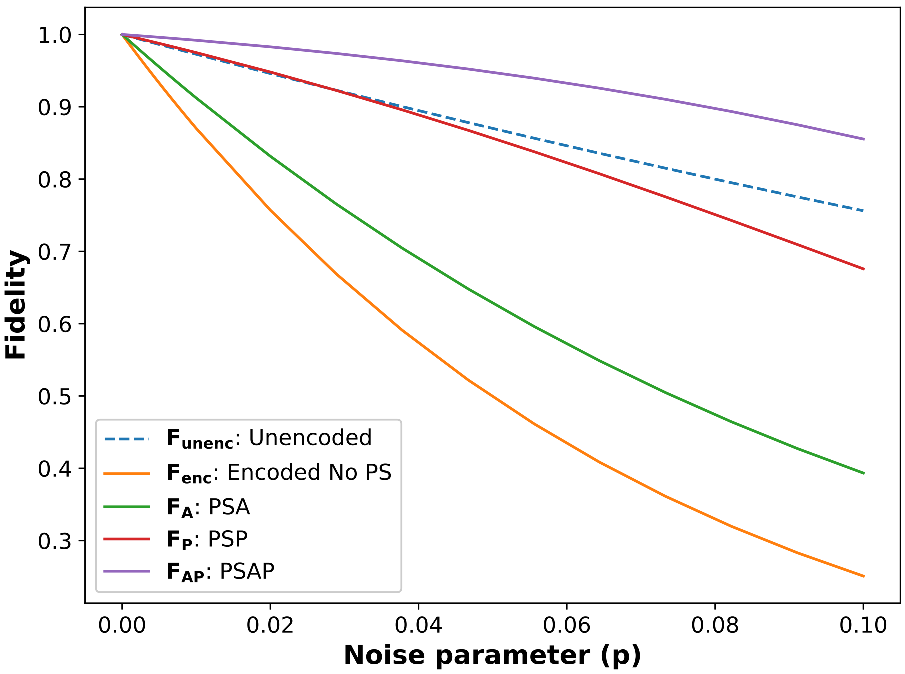

Figure 5.8: Fidelity of the states prepared by numerically simulating the respective unencoded state, [[4,2,2]] encoded state and projected states corresponding to the post-selection methods, PSA, PSP and PSAP, with increasing standard depolarizing noise, p.

Both fidelity and accuracy of the energy estimates in the simulated encoded and unencoded circuits are impacted by the errors introduced by the depolarizing error model. In the encoded circuit, in particular, the single- and two-qubit gate errors in the noise model manifest as logical, p_{ϵ_L} or non-logical errors $(p_{\epsilon_{NL}})$ in the final noisy mixed state. We present the proportion of logical errors, p_{ϵ_L}, in the encoded circuit and in the projected state with $a_1 = 0$ (p_{ϵ_A}) in **Figure 5.9** and also present the proportion of all errors with increasing two-qubit depolarizing noise. While the errors increase with increasing noise, the proportion of all errors that are logical is much smaller. Since a logical error in this encoding requires an error event on a minimum of two qubits, the small proportion of logical errors indicate that a large proportion of errors in the encoded circuit are non-logical, single- and multi-qubit errors.

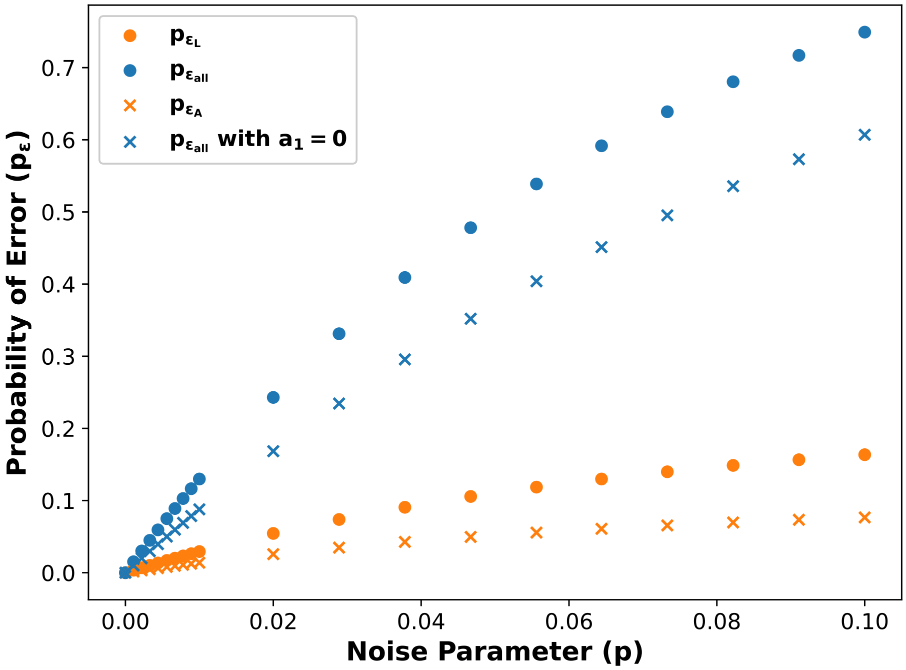

Figure 5.9: Probability of Error, (p_ϵ) in the encoded circuit with increasing two-qubit depolarizing noise. Plot labeled with $a_1 = 0$ are errors in the state projected with $a_1 = 0$

We also present the fidelity with increasing two-qubit depolarizing noise p for the encoded input state $|\overline{00}\rangle$ and the states projected using S_A, S_P and S_{AP} in **Figure 5.10** to further understand the contribution of ancilla a_1 to the improvement in the accuracy of the energy estimate. We compare the fidelity of the state projected by S_P with S_{AP} for the same final encoded, $|\overline{00}\rangle$, input state. Improvement in fidelity, F_{S_P}, is due to the removal of states with single qubit bit-flip errors by projection operator S_P. Combining the two methods using projector S_{AP} not only improves the fidelity over the fidelity F_{S_P} for the state projected by S_P, but also results in fidelity that's nearly 1 at $\lesssim 5\%$ noise.

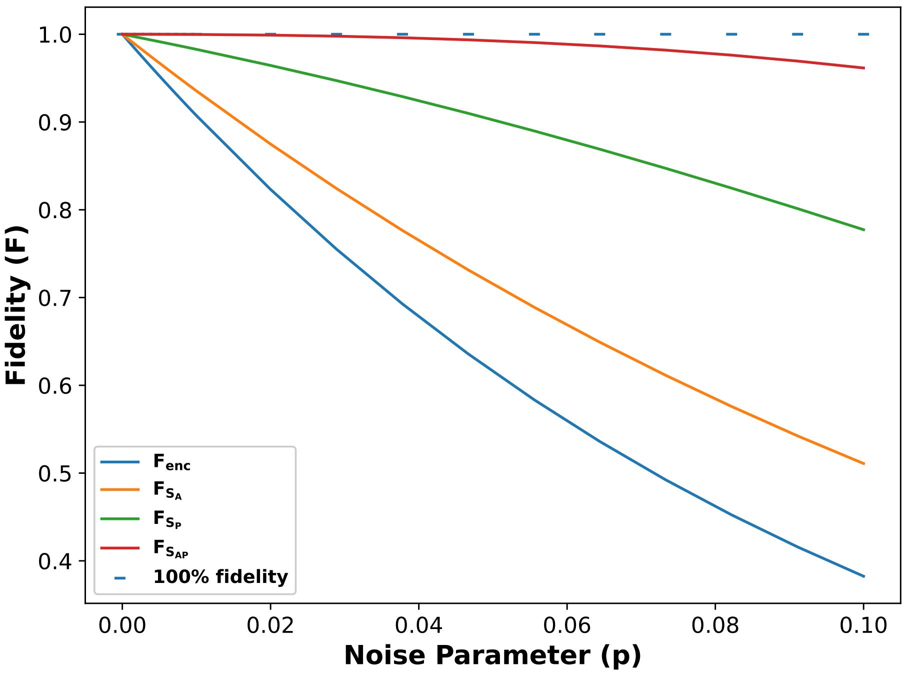

Figure 5.10: State fidelity for the noisy logical input $\overline{|00\rangle}$ state preparation and the projected states from the circuit labeled "State Prep" in **Figure 5.3** and shown in **Figure 5.4**

5.5 Discussion

Error detection improves energy estimates over the unencoded ansatz when using post-selection by logical state parity, PSP, by itself at low noise values, and in combination with post-selection by ancilla, a_1, measurement, PSAP, at least up to 10% noise. The latter also results in energy estimates within chemical accuracy at a higher noise threshold than the unencoded simulation. The magnitude of improvement in logical fidelity, F_P, of the state projected by Π_P, under the depolarizing noise model that we have considered, indicates that single physical qubit errors are the most probable errors and the leading cause of decrease in energy accuracy. Such single physical qubit errors can also be caused by multi-qubit errors that effectively become single qubit errors.

The decrease in precision of the estimated energy calculated from post-selected results of the simulation of the encoded ansatz compared to the unencoded ansatz is due to consideration of only one half of the results from ancilla, a_2, measurement as described in the Methods section. Within the different post-selection methods, improvement in precision is consistent with improvement in logical fidelity, indicating that in addition to improvement in the accuracy of the energy estimate, post-selection also improves the corresponding precision of the calculation. The improvement in precision in spite of increasing loss of samples with increasing accuracy of the post-selection method is a result of the improvement in variance of the calculation.

The deviation of the estimated energy using the the PSP and PSAP methods from the corresponding energy expectation value calculation using the density matrix, occurs due to the difference in order of operations between the two methods. In the latter, the states of interest are projected and the expectation value is calculated from these states. In the former, the bitstrings are post-selected from the measurement of the final state and then the expectation values are calculated from these post-selected bitstrings.

Post-selection strategies using the ancilla, a_1, lead to improvement in accuracy of the energy estimate due to detection of single and multi-qubit error events. Nearly unity fidelity, $F_{S_{AP}}$, for projecting states with logical state parity and $a_1 = 0$ measurement indicates that a_1 detects nearly all multi-qubit error events that are left undetected by projecting states with logical state parity alone. Additionally, the reduction in probability of logical errors in the state projected for ancilla, $a_1 = 0$ measurement, further confirm the detection of errors other than single qubit errors by ancilla a_1.

5.6 Conclusion

Post-selection based on detection of single qubit errors alone improves the accuracy of the energy estimate at low noise levels. Combining this post-selection method with post-selection using an ancilla for single and multi-qubit error detection during input state preparation further improves the accuracy of the estimate at noise levels as high as 10%. Constructing the input state-preparation circuit such that the control qubit for all the two-qubit $CNOT$ gates is the qubit, q_0, which is entagled with the ancilla, a_1, makes the detection of multi-qubit errors possible.

In addition to improvement in accuracy, post-selection also improves the precision of the calculation. Loss of precision compared to the unencoded ansatz simulation is due to the superposition of states introduced by the ancilla used to execute the VQE ansatz/sub-routine in the encoded state. Improvement in fidelity is limited by the errors, single and multi-qubit, that effectively become or remain as multi-qubit errors because they were either left undetected by the ancilla during input state preparation and/or by the parity check after the VQE sub-routine.

We have demonstrated that post-selection methods lead to an energy estimate within chemical accuracy at a higher threshold of noise than the unencoded simulation for a small two-electron system. Ansatzes for larger systems will increase the qubit and gate overhead, which will include an increase in rotation operations and potentially, parameters for optimization. Since the [[4,2,2]] code is known to be the simplest quantum error detection code, employing other error detection codes would also increase the resource cost in terms of qubits and gates. Therefore, the noise threshold at which the energy estimates reach chemical accuracy for larger systems will depend, at a minimum, on the complexity of the application circuit, the code used for error detection and the associated methods of post-selection.

5.7 Acknowledgements

This work was supported by the US Department of Energy, Advanced Scientific Computing Research, Accelerated Research for Quantum Computing program. D.C. acknowledges support by the "Embedding Quantum Computing into Many-body Frameworks for Strongly Correlated Molecular and Materials Systems" project, which is funded by the U.S. Department of Energy (DOE), Office of Science, Office of Basic Energy Sciences, the Division of Chemical Sciences, Geosciences, and Biosciences.

Appendix

Hamiltonian encoding

We start with the exact electronic Hamiltonian for molecular hydrogen in second quantized form:

$$\begin{aligned} H(R) = {} & h_{00}a_0^\dagger a_0 + h_{22}a_2^\dagger a_2 + h_{33}a_3^\dagger a_3 + h_{11}a_1^\dagger a_1 \\ & + h_{2002}a_2^\dagger a_0^\dagger a_0 a_2 + h_{3113}a_3^\dagger a_1^\dagger a_1 a_3 + h_{2112}a_2^\dagger a_1^\dagger a_1 a_2 \\ & + h_{0330}a_0^\dagger a_3^\dagger a_3 a_0 + (h_{2332} - h_{2323})a_2^\dagger a_3^\dagger a_3 a_2 \\ & + (h_{0110} - h_{0101})a_0^\dagger a_1^\dagger a_1 a_0 + h_{2103}(a_2^\dagger a_1^\dagger a_0 a_3 + a_3^\dagger a_0^\dagger a_1 a_2) \\ & + h_{2013}(a_2^\dagger a_0^\dagger a_1 a_3 + a_3^\dagger a_1^\dagger a_0 a_2) \end{aligned} \tag{5.38}$$

The possible states within the spin-singlet configuration in the fermionic basis for the hydrogen molecule and the corresponding states in the two qubit basis are presented in **Table 5.3**. The indices correspond with those of the molecular orbitals in 5.6.

Table 5.3: Mapping of fermionic basis to qubit basis for all possible states of the hydrogen molecule with the spin-singlet configuration. Indices for the fermionic basis correspond with indices in 5.6 and indices for the qubit basis correspond with the qubits used in the circuit construction of the unitary operator.

$\lvert\Psi_3\Psi_2\Psi_1\Psi_0\rangle$	$\lvert q_0q_1\rangle$
$\lvert 0101\rangle$	$\lvert 00\rangle$
$\lvert 0110\rangle$	$\lvert 01\rangle$
$\lvert 1001\rangle$	$\lvert 10\rangle$
$\lvert 1010\rangle$	$\lvert 11\rangle$

We define the qubit excitation, de-excitation and number operators as in (Shee et al., 2022)

$$\begin{aligned} Q^{+} &= |1\rangle\langle 0| = \frac{1}{2}(X - iY) \\ Q^{-} &= |0\rangle\langle 1| = \frac{1}{2}(X + iY) \\ N^{(0)} &= |0\rangle\langle 0| = \frac{1}{2}(I + Z) \\ N^{(1)} &= |1\rangle\langle 1| = \frac{1}{2}(I - Z) \end{aligned} \tag{5.39}$$

where X, Y, and Z are the Pauli operators. These operators are used to construct the reduced two-qubit Hamiltonian by using the mapping presented in **Table 5.4**.

Table 5.4: Fermionic (de)excitation and number operators mapped to the corresponding qubit and Pauli operators, where E_{pq} represents the excitation and number operators when $p \neq q$ and $p = q$, respectively. The Pauli operators are constructed using 5.39.

Operator	**Fermionic operators**	**qubit operators**	**Pauli operators for qubits**
E_{10}	$\vert 0110\rangle\langle 0101\vert + \vert 1010\rangle\langle 1001\vert$	$\vert 01\rangle\langle 00\vert + \vert 11\rangle\langle 10\vert$	$\frac{1}{2}(X_0 - iY_0)$
E_{32}	$\vert 1001\rangle\langle 0101\vert + \vert 1010\rangle\langle 0110\vert$	$\vert 10\rangle\langle 00\vert + \vert 11\rangle\langle 01\vert$	$\frac{1}{2}(X_1 - iY_1)$
E_{00}	$\vert 0101\rangle\langle 0101\vert + \vert 1001\rangle\langle 1001\vert$	$\vert 00\rangle\langle 00\vert + \vert 10\rangle\langle 10\vert$	$\frac{1}{2}(I + Z_0)$
E_{11}	$\vert 0110\rangle\langle 0110\vert + \vert 1010\rangle\langle 1010\vert$	$\vert 01\rangle\langle 01\vert + \vert 11\rangle\langle 11\vert$	$\frac{1}{2}(I - Z_0)$
E_{22}	$\vert 0101\rangle\langle 0101\vert + \vert 0110\rangle\langle 0110\vert$	$\vert 00\rangle\langle 00\vert + \vert 01\rangle\langle 01\vert$	$\frac{1}{2}(I + Z_1)$
E_{33}	$\vert 1001\rangle\langle 1001\vert + \vert 1010\rangle\langle 1010\vert$	$\vert 10\rangle\langle 10\vert + \vert 11\rangle\langle 11\vert$	$\frac{1}{2}(I - Z_1)$

The electronic Hamiltonian is then reduced as

$$H = \sum_{pq} h_{pq} E_{pq} + \frac{1}{2} \sum_{pqrs} h_{pqrs} \delta_{qr} E_{ps} - E_{pr} E_{qs} \tag{5.40}$$

where $E_{pq} = a_p^\dagger a_q$ includes terms with $p = q$ and are presented in **Table 5.4**. Using these operators we proceed to transform the electronic Hamiltonian in 5.38 to a qubit representation:

$$
\begin{aligned}
H &= h_{00}E_{00} + h_{22}E_{22} + h_{33}E_{33} + h_{11}E_{11} \\
&+ h_{2002}E_{22}E_{00} + h_{3113}E_{33}E_{11} + h_{2112}E_{22}E_{11} + h_{0330}E_{33}E_{00} \\
&+ (h_{2332} - h_{2323})(E_{22} - E_{23}E_{32}) + (h_{0110} - h_{0101})(E_{00} - E_{01}E_{10}) \\
&+ h_{2103}(0 - E_{23}E_{10} + 0 - E_{32}E_{01}) + h_{2013}(0 - E_{23}E_{01} + 0 - E_{32}E_{10}) \\
&= h_{00}(\frac{1}{2}(I + Z_0)) + h_{22}(\frac{1}{2}(I + Z_1)) + h_{33}(\frac{1}{2}(I - Z_1)) + h_{11}\frac{1}{2}(I - Z_0) \\
&+ h_{2002}(\frac{1}{4}(I + Z_1)(I + Z_0)) + h_{3113}(\frac{1}{4}(I - Z_1)(I - Z_0)) \\
&+ h_{2112}(\frac{1}{4}(I + Z_1)(I - Z_0)) + h_{0330}(\frac{1}{4}(I - Z_1)(I + Z_0)) \\
&+ (h_{2332} - h_{2323})(\frac{1}{2}(I + Z_1) - \frac{1}{4}(X_1 + iY_1)(X_1 - iY_1)) \\
&+ (h_{0110} - h_{0101})(\frac{1}{2}(I + Z_0) - \frac{1}{4}(X_0 + iY_0)(X_0 - iY_0)) \\
&+ h_{2103}(-\frac{1}{4}(X_1 + iY_1)(X_0 - iY_0) - \frac{1}{4}(X_1 - iY_1)(X_0 + iY_0)) \\
&+ h_{2013}(-\frac{1}{4}(X_1 + iY_1)(X_0 + iY_0) - \frac{1}{4}(X_1 - iY_1)(X_0 - iY_0)) \\
&= (h_{00} + h_{33} + \frac{h_{2002}}{4} + \frac{h_{3113}}{4} + \frac{h_{2112}}{4} + \frac{h_{0330}}{4})I \\
&+ (h_{00} - h_{11} + \frac{1}{4}(h_{2002} - h_{3113} - h_{2112} + h_{0330}))Z_0 \\
&+ (h_{22} - h_{33} + \frac{1}{4}(h_{2002} - h_{3113} + h_{2112} - h_{0330}))Z_1 \\
&+ \frac{1}{4}(h_{2002} + h_{3113} - h_{2112} - h_{0330})Z_1Z_0 + 0 + 0 \\
&+ h_{2103}(\frac{1}{2}(-X_1X_0 - Y_1Y_0) \\
&+ h_{2013}(\frac{1}{2}(-X_1X_0 + Y_1Y_0)
\end{aligned}
\tag{5.41}
$$

$$
\begin{aligned}
g_0 &= h_{00} + h_{33} + \frac{h_{2002}}{4} + \frac{h_{3113}}{4} + \frac{h_{2112}}{4} + \frac{h_{0330}}{4} \\
g_1 &= h_{00} - h_{11} + \frac{1}{4}(h_{2002} - h_{3113} - h_{2112} + h_{0330}) \\
g_2 &= h_{22} - h_{33} + \frac{1}{4}(h_{2002} - h_{3113} + h_{2112} - h_{0330}) \\
g_3 &= \frac{1}{4}(h_{2002} + h_{3113} - h_{2112} - h_{0330}) \\
g_4 &= -h_{2103}
\end{aligned} \tag{5.42}
$$

Additionally:

$$
\begin{aligned}
g_1 &= g_2 \\
h_{2013} &= h_{2103} \\
h_{2112} &= h_{0330}
\end{aligned} \tag{5.43}
$$

This leads to the final two qubit hamiltonian shown in 5.8.

Unitary Operator

To transform the fermionic unitary operator to a qubit representation specific to our encoding we use qubit operators from 5.39. Considering only the doubles contribution in 5.10 and 5.11, we replace the fermionic operators in T_2 with qubit operators using 5.39 as shown in 5.44.

$$
\begin{aligned}
T_2 = &\sum_{p>q\in occ.,r>s\in virt.} \theta^{pq}_{rs}(a_p^\dagger a_q^\dagger a_r a_s - a_s a_r a_q^\dagger a_p^\dagger) \\
&= \theta^{20}_{31}(a_2^\dagger a_0^\dagger a_3 a_1 - a_1^\dagger a_3^\dagger a_0 a_2) \\
&= \theta^{20}_{31}(E_{10}E_{32} - E_{23}E_{01}) \\
&= \theta^{20}_{31}\frac{1}{4}((X_0 - iY_0)(X_1 - iY_1)) - \frac{1}{4}((X_1 + iY_1)(X_0 + iY_0)) \\
&= \theta^{20}_{31}\frac{1}{2}(-iY_0X_1 - iX_0Y_1) \\
&= i\theta^{20}_{31}\frac{1}{2}(-Y_0X_1 - Y_0X_1Z_0Z_1)
\end{aligned} \tag{5.44}
$$

where we have used $Y_k Z_k = iX_k$, $X_k Z_k = -iY_k$, to factorize the operator in the final step. Considering our reference state $|00\rangle$, we arrive at the reduced UCC doubles ansatz as shown in 5.45:

$$\begin{aligned} U(\theta) &= e^{i\frac{\theta}{2}(-Y_0X_1)} e^{i\frac{\theta}{2}(-Y_0X_1Z_0Z_1)} \\ &= e^{i\frac{\theta}{2}(-Y_0X_1)} e^{i\frac{\theta}{2}(-Y_0X_1)} \\ &= e^{-i\theta Y_0X_1} \end{aligned} \tag{5.45}$$

Projection operators expanded

$$\begin{aligned} \Pi_P = \mathbb{I}_{a_1} \otimes (&|0000\rangle\langle 0000| + |0000\rangle\langle 1111| \\ &+ |1111\rangle\langle 0000| + |1111\rangle\langle 1111| \\ &+ |0011\rangle\langle 0011| + |0011\rangle\langle 1100| \\ &+ |1100\rangle\langle 0011| + |1100\rangle\langle 1100| \\ &+ |1010\rangle\langle 1010| + |1010\rangle\langle 0101| \\ &+ |0101\rangle\langle 0101| + |0101\rangle\langle 0101| \\ &+ |0110\rangle\langle 0110| + |0110\rangle\langle 1001| \\ &+ |1001\rangle\langle 0110| + |1001\rangle\langle 1001|) \otimes |0\rangle\langle 0|_{a_2} \\ \Pi_{AP} = |0\rangle\langle 0|_{a_1} \otimes (&|0000\rangle\langle 0000| + |0000\rangle\langle 1111| \\ &+ |1111\rangle\langle 0000| + |1111\rangle\langle 1111| \\ &+ |0011\rangle\langle 0011| + |0011\rangle\langle 1100| \\ &+ |1100\rangle\langle 0011| + |1100\rangle\langle 1100| \\ &+ |1010\rangle\langle 1010| + |1010\rangle\langle 0101| \\ &+ |0101\rangle\langle 0101| + |0101\rangle\langle 0101| \\ &+ |0110\rangle\langle 0110| + |0110\rangle\langle 1001| \\ &+ |1001\rangle\langle 0110| + |1001\rangle\langle 1001|) \otimes |0\rangle\langle 0|_{a_2} \end{aligned} \tag{5.46}$$

Chapter 6

Estimates for Error Management on a Near-Term Quantum Computer

The quantum computing methods developed in chapter 5 are now used to determine the computational accuracy of a noisy quantum computer To demonstrate the evaluation, the algorithm and methods developed in chapter 5 for simulating the ground state of molecular hydrogen are used to evaluate the resources required to calculate, with chemical accuracy, the ground state energy using a commercially available trapped-ion quantum computer.

6.1 Introduction

As discussed in chapter 1, state-of-the-art quantum computing devices are achieving lower error rates. This leads to the question: what is the computational accuracy of a given device? There are many approaches to evaluate this accuracy metric. In keeping with the motivation of the thesis, which is to understand the requirements for managing errors for quantum applications in near-term quantum computers, we perform the evaluation using a leading quantum application. Simulation of quantum chemistry on a quantum computer is widely considered to be one of the most promising and leading applications of quantum computing. The promise is an improvement in quantitative accuracy of results when using a quantum computer to simulate a quantum system in polynomial time. Within the domain of quantum chemistry, chemical accuracy is the threshold required for making reliable predictions of properties such as reaction enthalpies, atomization energies etc.. We study a small quantum chemistry application on a commercially available noisy quantum device and estimate the quantum resources required to benchmark the computational accuracy of the device in terms of the domain specific accuracy and precision benchmark of chemical accuracy.

Recent developments in quantum computing hardware indicate that the field is taking the first steps toward demonstrating fault tolerant computing. These developments include demonstrations of logical qubits and quantum error correction AI (2023); Livingston et al. (2022); Sivak et al. (2023); Ryan-Anderson et al. (2021); Krinner et al. (2022); Acharya et al. (2023); Mayer et al. (2024); Da Silva et al. (2024). However, physical noise in current quantum computers is not yet sufficient for large-scale fault-tolerant implementation of quantum algorithms Beverland et al. (2022). It has also been suggested that techniques to combat noise such as error mitigation will be required even in the fault-tolerant regime of quantum computing Lostaglio and Ciani (2021); Piveteau et al. (2021); Suzuki et al. (2022).

While these developments are part of an active and ongoing research effort to enable fault tolerant quantum computing, we have available today techniques for quantum error detection that have been used to study early fault tolerance on commercial quantum devices. These QED codes have been shown to improve the error rate of logical qubits compared to physical qubits when employing post-selection against detected errors and have been used to improve the accuracy of quantum applications, more recently Córcoles et al. (2015); Linke et al. (2017); Roffe et al. (2018); Zhong et al. (2014); Willsch et al. (2018); Vuillot (2017); Takita et al. (2017); Rosenblum et al. (2018); Urbanek et al. (2020b); Pokharel and Lidar (2024); Yamamoto et al. (2024). Here we perform an analysis of the resources required to benchmark the computational accuracy of a current noisy quantum computing device against the domain specific threshold of chemical accuracy by employing error detection to manage the dominant sources of error.

Simulation of molecular hydrogen using the variational quantum eigensolver algorithm calculates the molecular ground state energy. To manage errors in the calculation, we encode the algorithm using the [[4,2,2]] quantum error detection code and use post-selection to filter noisy outcomes. This encoding scheme has been shown to improve energy estimates compared to the unencoded ansatz on an IBM 5-qubit device Urbanek et al. (2020b). We use this encoding to perform the resource analysis for a commercial trapped-ion device by Quantinuum based on the methodology developed in chapter 5.

The analysis evaluates the effect of quantum error detection and sufficient sampling, on the accuracy and precision of the estimated energy. The energy expectation value is considered to be within chemical accuracy if it is estimated to be within 1.6 mHa of the exact energy of the chosen basis set Cao et al. (2019b). In order to evaluate the computational accuracy of the device, the precision of the estimated energy, which determines whether accuracy of the energy is reproducible on every execution of the computation, is required to be ±1.6 mHa. In the previous chapter, we performed analytical calculations for this application and determined the number of samples at which the ground state energy of molecular hydrogen was well within chemical accuracy to be $\sim 2 \times 10^6$. With such sampling and sufficiently low depolarizing noise, energy estimated from the noisy numerical simulation of the encoded circuit was found to reach chemical accuracy while the unencoded counterpart did not. We use the same framework to evaluate the computational accuracy of quantum computing hardware against the benchmark of chemical accuracy on a more realistic noise model.

While the numerical simulations indicated improved results with the encoded application, the improvements were observed for an isotropic depolarizing error model applied independently to each qubit. Modern devices however also have noise sources such as coherent noise and crosstalk. The previous simulations also did not include read out or measurement error, which is the dominant source of error in quantum computers. Therefore, it remains to be seen how the additional noise in current quantum computers is mitigated by the encoding, which adds significant number of gates and qubits to the problem compared to the unencoded ansatz.

We demonstrate the resource analysis using the emulator for the Quantinuum H1-1 device. The H1-1 is a trapped-ion device using atomic hyperfine states of $^{171}\mathrm{Yb}^{+}$ Ryan-Anderson et al. (2022). The device has 20 qubits with all-to-all connectivity. All the operations, single-, two-qubit gates, measurement and initialization are implemented in specific zones on the device called interaction zones by transporting the qubits individually or in pairs to these zones. The device has five such zones and can perform at most five operations in parallel at a time.

We estimate the H1-1 resources required to use the VQE algorithm for simulating the ground state of molecular hydrogen to calculate the energy expectation value and the precision. More precisely, the analysis requires the estimated energy expectation value to lie within 1.6 mHa of the exact energy while also having a standard error or precision within ±1.6 mHa to be considered as being within chemical accuracy. We use the emulator, H1-1E, provided by Quantinuum for their devices to verify the program and estimate the performance of the device to validate the resource analysis. The emulator is designed to closely mimic the device in terms of the noise model with the default parameters set to the error rates of the device. It uses an identical compiler and same set of quantum and classical operations as the actual H1-1 device. A subset of the error rates are provided in **Table 6.1**.

Table 6.1: Default error rates of Quantinuum H1-1E emulator reproduced from Quantinumm Emulator product data sheet.

Parameters	**H1-1E**
Single-Qubit Fault Probability (p1)	2.1×10^{-5}
Two-qubit Fault Probability (p2)	8.8×10^{-4}
Bit-Flip Error Probability (Prob(1/0))	1×10^{-3}
Bit-Flip Error Probability (Prob(0/1))	4×10^{-3}

In addition to gate noise, devices also have read-out noise, labeled as "Bit-Flip Error Probability" in **Table 6.1**. We mitigate this noise by encoding the qubits in a read-out error detection code. We compare the results of simulations with and without the read out error detection (RED) code to evaluate the impact of the encoding towards improving the accuracy of the calculation in addition to the [[4,2,2]] quantum error detection code.

6.2 Methods

We will use methods developed in chapter 5 in the emulator implementation of the problem. A brief explanation of the methods from the previous chapter is presented here. This is followed by a description of the read out error detection strategy using two- and three-qubit repetition codes and the details of the simulations on the emulator Hicks et al. (2022).

6.2.1 VQE And Quantum Chemistry

The variational quantum eigensolver algorithm is a quantum-classical hybrid algorithm widely used for quantum chemistry simulations on near-term quantum computers. We encode a reduced two-qubit molecular hydrogen ansatz for simulating the ground state of the hydrogen molecule using the [[4,2,2]] quantum error detection code. We simulate the unencoded and encoded circuits on the emulator and measure the Pauli terms in the Hamiltonian to estimate the energy in each case. In the case of the encoded ansatz, we will additionally post-select the results based on the methods presented in the previous chapter: post-selection by ancilla measurement (PSA), post-selection by logical state parity (PSP) and post-selection by ancilla measurement and logical state parity (PSAP), before calculation of the energy estimate. We calculate standard error of the mean for every calculation. In the case of post-selected calculations, we also present the probability of success, as it impacts the standard error of the mean.

Since the device and device emulator also have read out error which was not considered in the previously conducted numerical simulations, we additionally encode the two circuits, the unencoded two-qubit ansatz and the encoded ansatz, with a repetition code for read out error detection.

6.2.2 Read Out Error Detection (RED)

The dominant source of error in a quantum computer is read out error, also called measurement error. The [[4,2,2]]-encoded ansatz requires read out error mitigation for every shot or circuit measurement, since the read-out error mitigated results need to be further processed using post-selection strategies associated with the [[4,2,2]]-encoding. Additionally, read-out error results only in bit-flip error, a classical error, which can be managed using classical error detection codes. The classical repetition code is a suitable method both for detecting classical bit-flip errors and to filter noisy results from every measurement prior to post-selection for the [[4,2,2]]-encoded ansatz.

We test two read out error detection codes, the two-qubit and three-qubit repetition code referred to as [2,1]- and [3,1]-RED codes, respectively, in keeping with the $[n, k]$ nomenclature, where n physical qubits encode k logical qubits Hicks et al. (2022). The codes encode the data qubits just prior to measurement. The data qubits are encoded by entangling each of them with its own ancilla(s) just prior to measurement as demonstrated for the [3,1]-RED code in **Figure 6.1** by encoding the unencoded ansatz shown in **Figure 5.1**. The ancillary qubits for read out are represented by r_i, s_i for data qubits q_i for $i \in [0, 1]$. For the [2,1]-RED code the circuit will only be constructed with read out qubits r_i for data qubits q_i for $i \in [0, 1]$.

Using the unencoded circuit shown in **Figure 6.1** as an example, the data qubits q_0, q_1 are redundantly encoded using qubits r_0, s_0 and r_1, s_1, respectively. In the noiseless case, the qubits r_i, s_i for $i \in [0, 1]$ would be measured in the same state as the corresponding data qubits q_i that they are entangled with, respectively. Measurement differences between the data and encoded qubits such as $|q_0 r_0 s_0\rangle = |001\rangle$ indicate an error has occurred on one or two of the qubits and therefore, such measurements are discarded. Measurements that indicate that all three qubits are equal indicate either no error has occurred or an error has occurred on all three qubits. Since the latter cannot be detected by this encoding, measurements where all three bits are equal, such as $|q_0 r_0 s_0\rangle = |111\rangle$ or $|q_0 r_0 s_0\rangle = |000\rangle$, are retained. Similarly, for the [2,1]-RED code, measurements of the data qubit q_i and read out qubit r_i are discarded if they result in odd parity, such as $|q_0 r_0\rangle = |01\rangle$ and retained if they have even parity, such as $|q_0 r_0\rangle = |11\rangle$.

The success of the code depends on the difference in magnitude of error rates between the two-qubit gate error and read out error. Having a much lower two-qubit gate error rate than read out error rate will lead to higher accuracy of the observable calculated from the post-selected measurements. A much lower two-qubit gate error rate would introduce much fewer errors due to the gate than the read out error, increasing the probability that the error observed during RED is due to measurement error rather than two-qubit gate error. Using the RED method with a higher two-qubit gate error rate than read-out error rate will lead to a decrease in accuracy of the results as the likelihood that the errors in measurement are caused due to the additional two-qubit gates used for the RED encoding becomes higher than errors introduced due to the measurement itself.

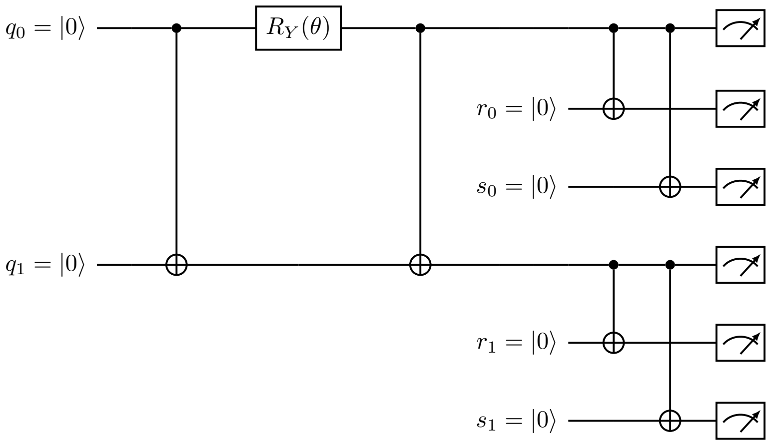

Figure 6.1: Unencoded UCC ansatz with encoding for [3,1]-RED using qubits r_i, s_i for $i \in [0, 1]$ for VQE

6.3 Encoding Methods

In this section, we present details on the methods to encode both the native UCCD ansatz and the [[4,2,2]]-encoded ansatz with the RED code. We also briefly review the methods used to simulate and post-process results for the electronic Hamiltonian of molecular hydrogen in the presence of circuit noise.

6.3.1 RED Encoding of the Unencoded and [[4,2,2]]-Encoded UCC Ansatz

Since the device and device emulator also have read out error, we encode the two circuits, the unencoded two-qubit ansatz and the [[4,2,2]]-encoded ansatz, with error detection code for RED.

The [[4,2,2]]-encoded and unencoded ansatzes with the [3,1]-RED results in the circuits shown in **Figure 6.1** and **Figure 6.2**, respectively. The ancillary qubits for [3,1]-RED code are represented by $r_i s_i$ for $i \in [0,1]$ and $k_i l_i$ for $i \in [0,5]$, respectively, for the unencoded and [[4,2,2]]-encoded ansatzes. The corresponding circuits with the [2,1]-RED code will be represented by read-out qubits r_i for $i \in [0,1]$ and k_i for $i \in [0,,5]$ for the unencoded and [[4,2,2]]-encoded ansatzes, respectively.

We use the XACC framework to run the numerical simulations of the VQE algorithm as in the previous chapter. We use the Quantinuum H1-1E emulator designed for the Quantinuum H1-1 device with their default error model within XACC for numerically simulating each ansatz with 3 values of the parameter $\theta \in [-0.400606, -0.22967, -0.058734]$ and the optimal parameter determined analytically to be $\theta^* = -0.22967$.

We calculate the energy expectation values for both the unencoded and encoded simulations, and for each post-selection method, with and without RED using $N = 188000$ shots, which we determined in the previous chapter by calculating the

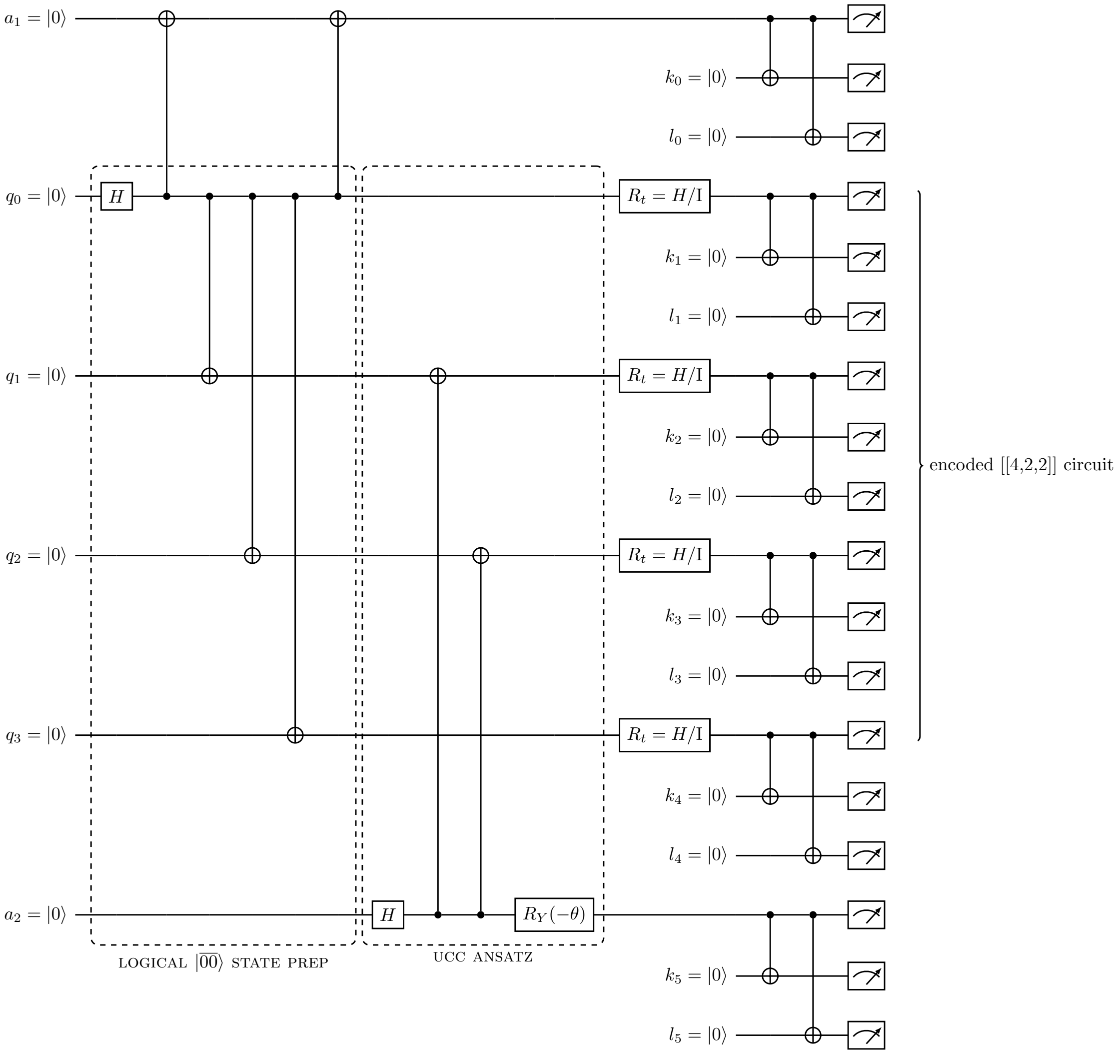

Figure 6.2: Encoded UCC ansatz using the [[4,2,2]] quantum error detection code, and additional encoding with qubits $k_i l_i$ for $i \in [0, 5]$ for [3,1]-RED

shot count required to estimate the energy within standard error of the mean (SEM) of 0.5mHa for a noiseless simulation as shown in equation 5.24.

$$\begin{aligned} N &= \frac{var}{\sigma^2_{E(\theta^*)}} \\ &= \frac{0.04700}{0.0005^2} \\ &= 188000 \end{aligned} \tag{6.1}$$

Post-Selection Strategies

We use the post-selection methods described the previous chapter for the [[4,2,2]]-encoded ansatz: post-selection by ancilla a_1 (PSA) measurement, in which we discard all measurements with $a_1 = 1$, post-selection by logical state parity (PSP), in which we discard measurement bitstrings that have odd parity but include measurement counts with both measurements of ancilla, $a_1 = 0$ and $a_1 = 1$ and PSAP, in which we discard measurement outcomes that have odd parity or ancilla, $a_1 = 1$. For circuits with encoding for RED, we perform an additional post-selection step prior to post-selection strategies listed for the [[4,2,2]]-encoding. In the case of the [3,1]-RED code, for each set of data and the corresponding read out qubits, a_i, k_i, l_i for $i \in [1, 2]$ and q_i, k_j, l_j for $i \in [0, 3]$ and $j \in [1, 4]$, in **Figure 6.2**, we discard outcomes in which all measurements are not equal to each other as they indicate read out error has occurred on one or two of the qubits. Similarly, in the case of the [2,1]-code we discard outcomes with odd parity for each set of data and read out qubits. The same method of post-selection applies for RED with the unencoded ansatz. We post-select outcomes from the measurement bitstrings once all qubits are measured. The expectation values of each Pauli term in the Hamiltonian are estimated from the available, post-selected measurements.

We also calculate the SEM for the energy estimated from each post-selection method by using equation 5.25.

Probability of Success

We report on the probability of success (η) for each post-selection strategy as defined in chapter 5 using equation 5.26. We present it along with the corresponding SEM calculating by using equation 5.27. For circuits with RED, n will include post-selection due to detected read out error events.

6.3.2 Simulations on the Emulator

Since we are evaluating the computational accuracy of the device using the emulator, we estimate the energy at the analytically determined optimal parameter with emulator for the Quantinuum H1-1 device. The Quantinuum H1-1 device is a trapped-ion quantum charge coupled device constructed with $^{171}\mathrm{Yb}^{+}$ ions as qubits and a "race-track" architecture with zones that have focused laser beams to implement gates Ryan-Anderson et al. (2022). The ions are transported to these zones for operations and the number of zones indicates the number of parallel operations possible in the device. The H1-1 device has five such zones. The maximum number of shots that can executed for a single circuit execution is 10000. We accordingly perform multiple circuit executions to reach the targeted 188000 shots and combine the counts before estimating the results. As described in the product data sheet for the Quantinuum H1-1 emulators, the provided emulator is designed to closely mimic the noise profile of the device. At the time the simulations for this study were executed, the version of the latest product data sheet of the emulator was 6.8.3 and was dated 18th Jul 2024. The physical noise parameters listed in this version of the data sheet are reproduced in **Table 6.2** and are considered to be the parameters for the noisy simulations in this study.

The Single-Qubit and Two-Qubit Fault Probability are the single- and two-qubit gate noise are largely modeled with asymmetric depolarizing noise channels, respectively.

Table 6.2: Physical noise parameters reproduced from version 6.8.3 of the product data sheet of the Quantinuum H1-1E emulator.

Noise Parameter	**Noise Parameter Value**
Single-qubit Fault Probability (p1)	2.1×10^{-5}
Two-qubit Fault Probability (p2)	8.8×10^{-4}
Bit Flip Measurement Probability (0 outcome)	1.0×10^{-3}
Bit Flip Measurement Probability (1 outcome)	4.0×10^{-3}
Crosstalk Measurement Fault Probability	1.45×10^{-5}
Initialization Fault Probability	3.62×10^{-5}
Crosstalk Initialization Probability	5.020×10^{-6}
Ratio of Single-Qubit Spontaneous Emission to p1	0.54
Ratio of Single-Qubit Spontaneous Emission in Two-Qubit Gate to p2	0.43

Fractions of Single- and Two-qubit gate noise that represents spontaneous emission instead of the asymmetric depolarizing noise are represented by Ratio of Single-Qubit Spontaneous Emission to p1 and Ratio of Single-Qubit Spontaneous Emission in Two-Qubit Gate to p2, respectively. The Bit Flip Measurement Probability (0 outcome) indicates probability of measuring 1 when the qubit is in 0 and vice versa for Bit Flip Measurement Probability (1 outcome). Initialization Fault Probability, as the name suggests, indicates probability of error at qubit initialization. Crosstalk error rates during measurement and initialization are indicated by Crosstallk Measurement Fault and Crosstalk Initialization Probability, respectively.

We estimate the energy at the optimal parameter for the unencoded and encoded ansatzes of molecular hydrogen on the emulator with their default error model with parameters shown in **Table 6.2**. For the simulation with the best energy estimate, we run simulations at three different parameters including the known optimal parameter to verify that the minimum energy estimate corresponds with the analytical optimal parameter. We calculate the variance and precision and in the case of the encoded simulation, the probabilities of success. We execute ansatzes in parallel where possible. For instance, about nine circuits of the unencoded two-qubit hydrogen ansatz shown in **Figure 5.1** can be implemented in parallel on the 20 qubit Quantinuum H1-1E device and emulator. The all-to-all connectivity proves useful for such executions.

We compare these results against the chemical accuracy benchmark and against results from numerical simulations reported in the previous chapter. We evaluate impact of using the [[4,2,2]] quantum error detection code on hardware using the emulator and additionally compare the results against the estimates from circuits with RED to evaluate the effectiveness of the read out error encoding against the read out noise included in the emulator noise model. We also compare results between the two RED codes.

6.4 Results

We present results from noisy simulations on the Quantinuum H1-1E emulator with their default error model. Their default error model closely mimics their H1-1 device. We present energy estimates and the corresponding standard error of the mean for molecular hydrogen with the unencoded ansatz and the encoded ansatz with and without post-selection. For results with post-selection, we also show the probability of success. We additionally present these results with the encoding for RED for both the unencoded and encoded ansatzes with the corresponding the probability of success. We describe the reference names used for the different simulations presented in this section in **Table 6.3**.

Table 6.3: Index of reference names used for different simulations with their descriptions.

Simulation Reference	**Description**
Unenc/Enc noiseless	Noiseless simulation of the unencoded/encoded ansatz on the Quantinuum H1-1 emulator.
Unencoded	Simulation of unencoded ansatz with default error model of the Quantinuum H1-1 emulator.
Unenc [2,1]-RED/[3,1]-RED	Simulation of unencoded ansatz with [2,1]-RED or [3,1]-RED encoding with default error model of the Quantinuum H1-1 emulator.
Enc PSA/PSP/PSAP/no PS	Simulation of [[4,2,2]]-encoded ansatz with default error model of the Quantinuum H1-1 emulator with PSA, PSP, PSAP or without PS.
Enc [2,1]-RED/[3,1]-RED PSA/PSP/PSAP/no PS	Simulation of [[4,2,2]]-encoded ansatz with [2,1]-RED or [3,1]-RED encoding on the Quantinuum H1-1 emulator with default error model with PSA, PSP, PSAP or without PS.

We first present results of the energy estimates of simulation of the unencoded ansatz and the encoded ansatz with post-selection with and without RED in **Table 6.4**. The table includes the energy estimates with and without RED of the unencoded ansatz and the best post-selection method of the encoded ansatz, PSAP, along with the corresponding difference, ΔE, from the exact energy of -1.13712Ha and the probability of success, η.

Table 6.4: Energy and Probability of Success (η) with and without RED for unencoded and [[4,2,2]]-Encoded ansatz with post-selection methods.

Simulation	Energy (mHa)	ΔE (mHa)	η (%)
Unencoded	-1133.39 ± 0.51	3.73	100
Encoded PSAP	-1129.78 ± 0.75	7.33	49.2
Unencoded with [2,1]-RED	-1134.60 ± 0.51	2.52	98.8
Encoded PSAP with [2,1]-RED	-1134.88 ± 0.73	2.23	48.2
Unencoded with [3,1]-RED	-1133.94 ± 0.51	3.17	98.2
Encoded PSAP with [3,1]-RED	-1135.74 ± 0.73	1.37	47.3

The simulation with the best energy estimate, the [[4,2,2]]-encoded ansatz with the [3,1]-RED, is presented with estimates for three parameter values and is presented in **Figure 6.3**. The parameter value for the minimum energy corresponds with the value calculated analytically.

We now show results of the energy estimates of simulation with the unencoded ansatz and the encoded ansatz with post-selection in **Figure 6.4**. These results do not include any mitigation against read out or measurement error. The Figure additionally has the corresponding noiseless estimates from the emulator as a reference. The shaded gray area represents the region within chemical accuracy or ±1.6 mHa of the exact energy for molecular hydrogen at 0.74Å. Error bars indicate the standard error of the mean. In this simulation, the unencoded ansatz results in the lowest energy estimate compared to the best and lowest energy estimates from encoded ansatz, i.e., with the PSAP strategy. Neither estimate, however, reaches chemical accuracy.

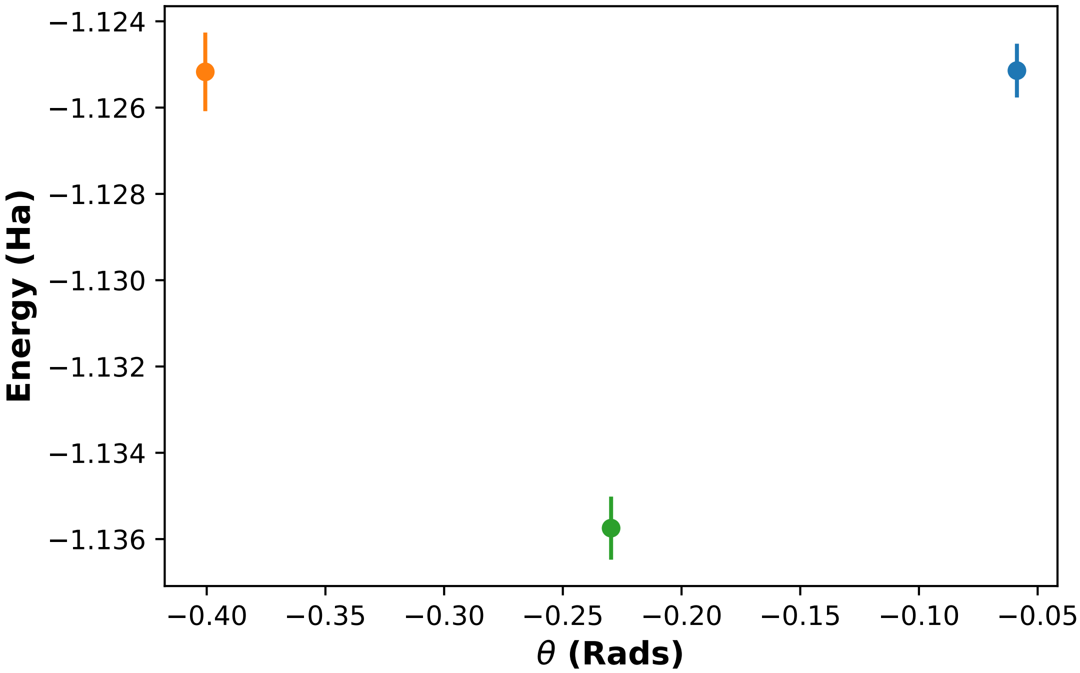

Figure 6.3: Energy estimates for three different parameters of the [[4,2,2]]-encoded ansatz simulation with the [3,1]-RED on the Quantinuum H1-1E emulator with the default error model.

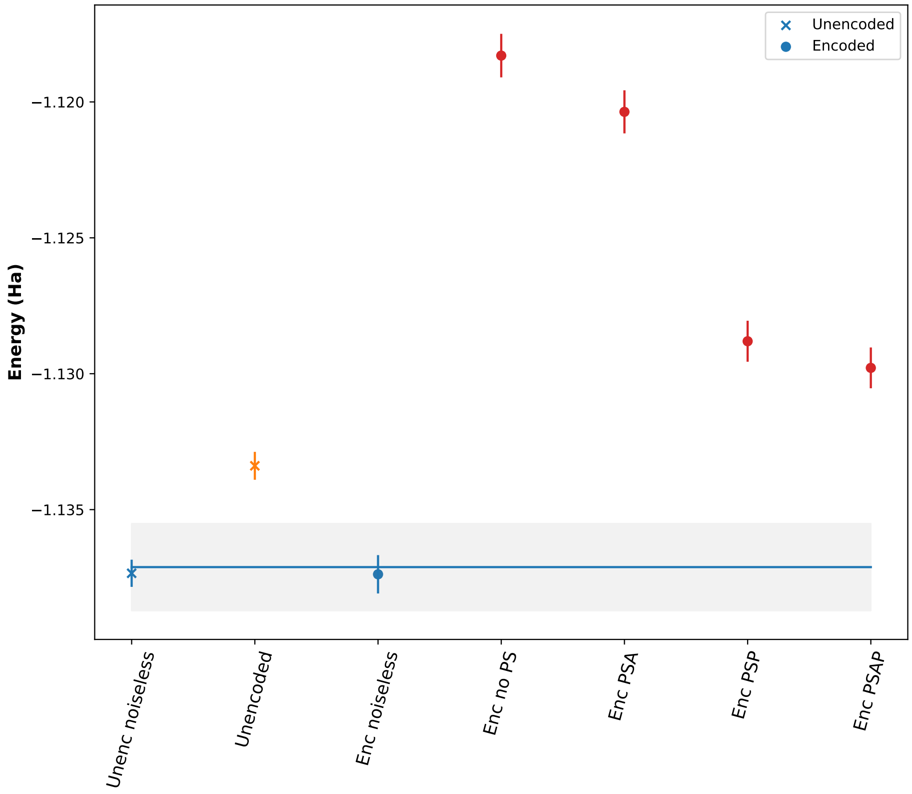

Figure 6.4: Energy estimates of unencoded and encoded simulations with post-selection without RED on the Quantinuum H1-1E emulator with the default error model. Shaded grey area represents the chemical accuracy region.

Employing RED leads to dramatic decrease in energy estimates for the encoded ansatz as shown in **Figure 6.5** and **Figure 6.6** for the [2,1]- and [3,1]-RED, respectively, and quantitatively presented in **Table 6.4**. For the unencoded ansatz, the codes only result in a slight decrease in the energy compared to the results without RED. The magnitude of reduction in the energy estimate for all post-selection methods of the [[4,2,2]]-encoded ansatz when using RED is higher than for the corresponding decrease in energy for the unencoded ansatz. Comparing the energy estimates resulting from the two RED codes in **Figure 6.7** for the unencoded and [[4,2,2]]-encoded ansatz shows that not only does the RED significantly improve the energy estimate for the [[4,2,2]]-encoded ansatz, the best estimate, the PSAP method, with the [3,1]-RED is within chemical accuracy and about 1.37 mHa from the exact energy as shown in **Table 6.4**. In the case of the unencoded ansatz the estimates are above the chemical accuracy regime for both RED codes with the lowest energy difference from the exact energy being ∼2.52 mHa with the [2,1]-RED code and this is about ∼1 mHa higher than chemical accuracy. The difference in the best estimate between the unencoded and [[4,2,2]]-encoded ansatz is about 1 mHa. Additionally, while using the [3,1]-RED code with the unencoded ansatz results in a better energy estimate than than not using any RED at all, it results in a slightly higher estimate than with the [2,1]-RED code.

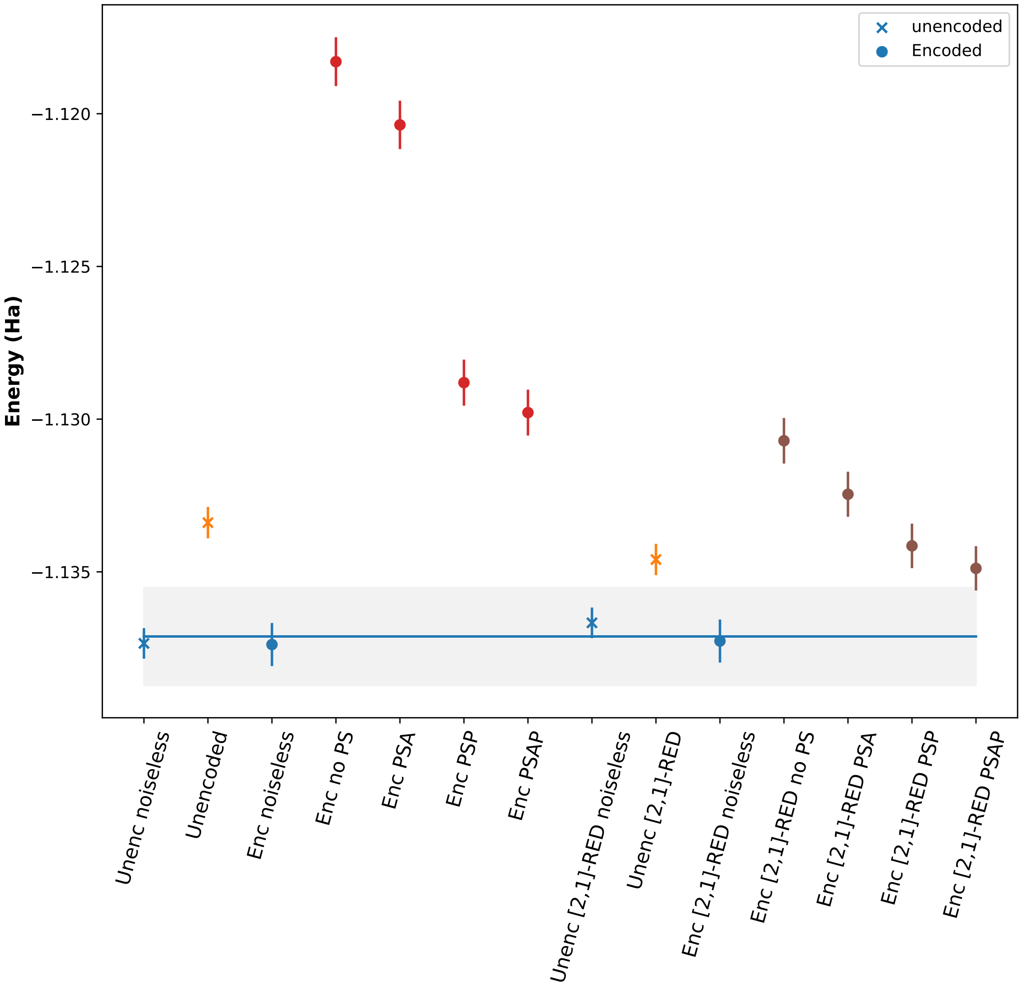

Figure 6.5: Energy estimates of unencoded and [[4,2,2]]-encoded simulations with post-selection without and with [2,1]-RED on the Quantinuum H1-1E emulator with the default error model. Shaded grey area represents the chemical accuracy region.

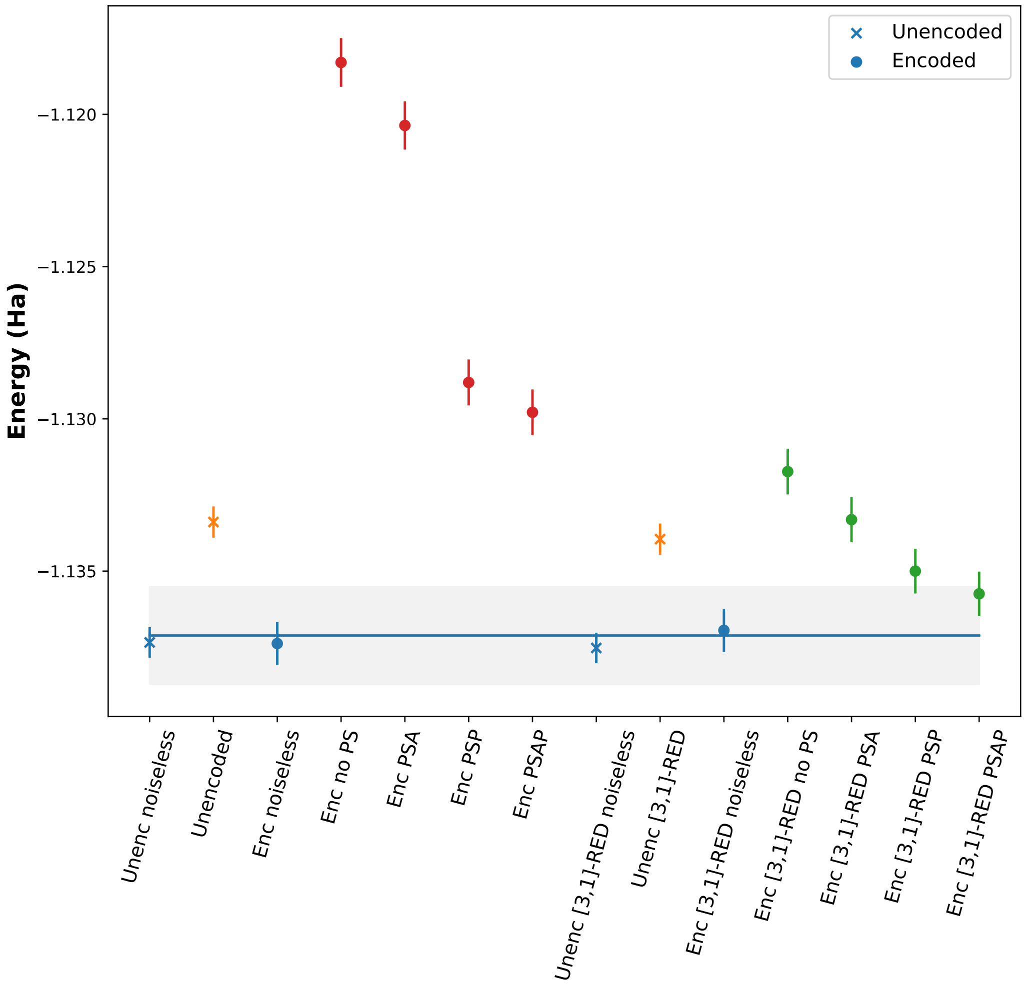

Figure 6.6: Energy estimates of unencoded and [[4,2,2]]-encoded simulations with post-selection without and with [3,1]-RED on the Quantinuum H1-1E emulator with the default error model. Shaded grey area represents the chemical accuracy region.

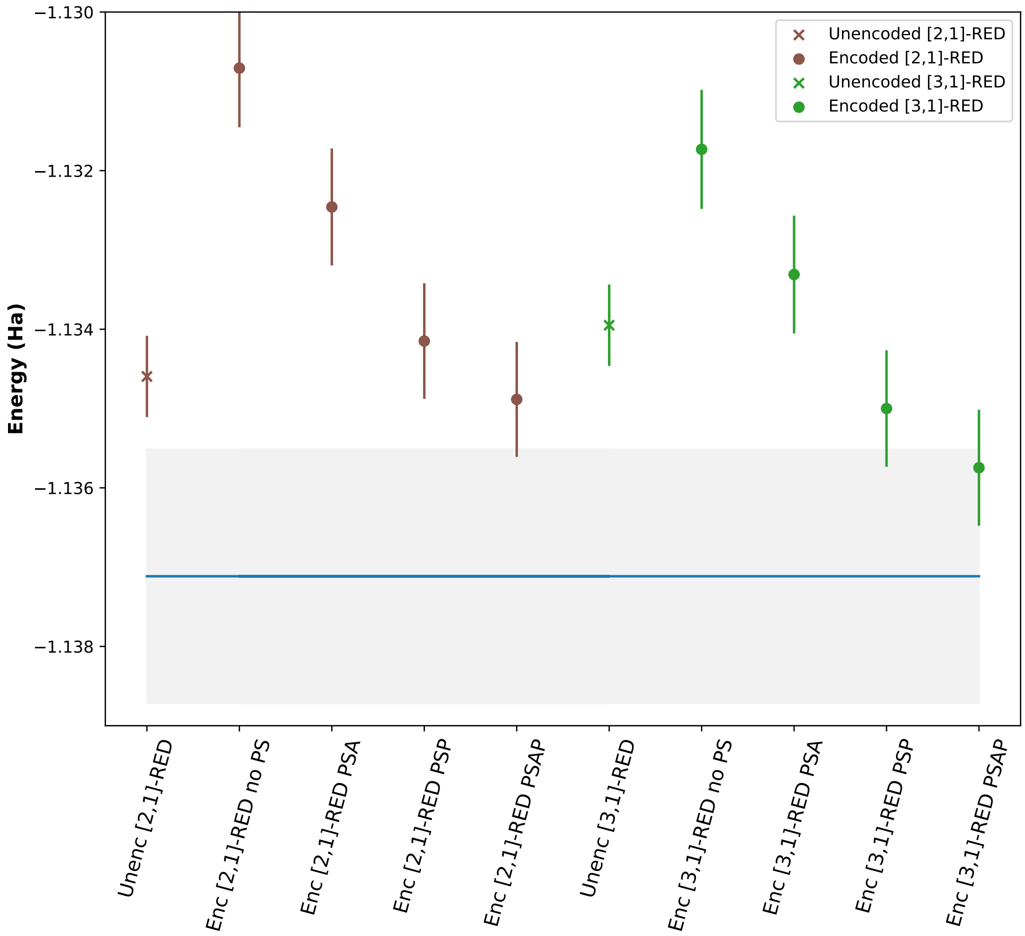

Figure 6.7: Energy estimates of unencoded and [[4,2,2]]-encoded simulations with [2,1]-RED and [3,1]-RED. Shaded grey area represents the chemical accuracy region.

We present the probability of success for the encoded ansatz simulation in **Figure 6.8** with and without RED. There is a drop in probability of success of ∼2% for the post-selection methods with [3,1]-RED from the simulations without RED but the corresponding drop in energy for the method with the best estimate, the PSAP method, with [3,1]-RED is nearly 6 mHa. The corresponding difference in energy for the best estimate with the unencoded ansatz is 1.2 mHa for a loss of 1.2% of samples as shown in **Table 6.4**. Additionally, the probability of success in the case of the unencoded ansatz is from 100% and for the [[4,2,2]]-encoded ansatz, from ∼50% as the implementation of gate teleportation with ancilla a_2 results in a uniform superposition of two equivalent states of which we only use one.

Finally, we present the resources required for the simulations of the [[4,2,2]]-encoded and unencoded ansatz for the best energy estimate with [3,1]-RED in **Table 6.5** based on the simulations on the emulator. Shots or number of samples are displayed as twice the amount since two circuit executions are required, one each for measuring the "Z_0Z_1" and "X_0X_1" Pauli term. Per run indicates the number of said resource that is required per execution of the circuit inlcuding parallel circuits. Parallel circuits per run are 0 for the encoded ansatz with [3,1]-RED as only one 18-qubit circuit can be executed on the 20-qubit emulator at a time, whereas three unencoded circuits can be executed with [3,1]-RED. Maximum number of single qubit gates point to the circuit for measuring "X_0X_1" Pauli term, which requires execution of additional Hadamard gates. The number of qubits required are reported for circuits with [3,1]-RED. Both the total number of qubits required for parallel executions and number of qubits required per ansatz execution is presented.

The expected cost is an approximate estimate of the total cost required as calculated by the Quantinuum emulator for executing these simulations on the Quantinuum device. Although this is not typically included in resource estimates, as devices become available for users commercially, there is a corresponding charge for accessing the devices which imposes an additional constraint that must be

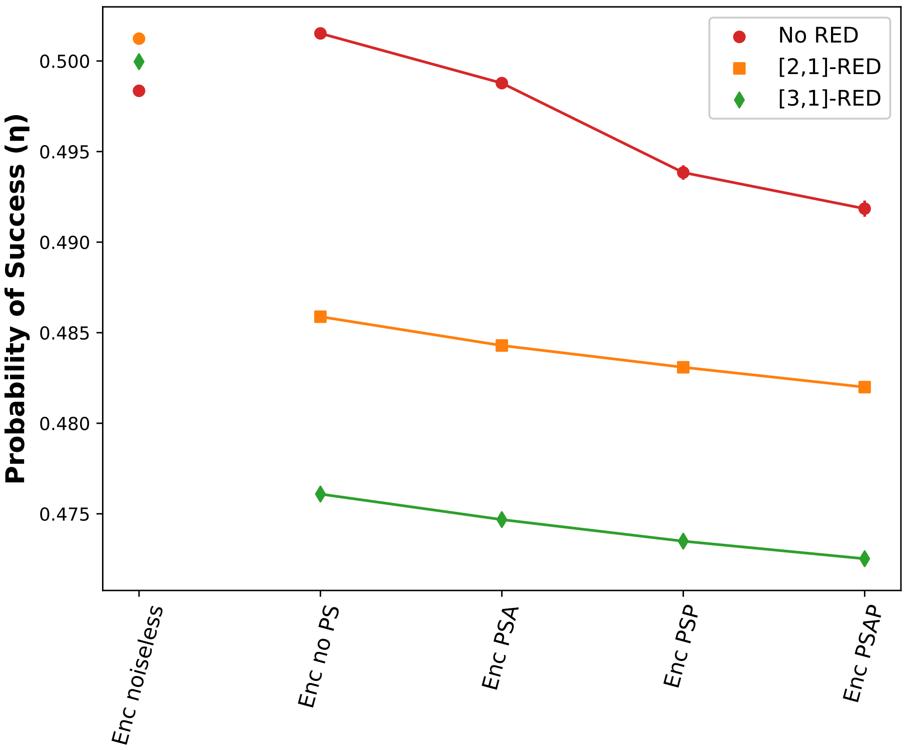

Figure 6.8: Probability of Success for Encoded Simulations on the Quantitnuum H1-1E emulator with and without RED.

Table 6.5: Resource analysis for estimating the ground state energy within chemical accuracy on the Quantinuum H1-1E emulator with [3,1]-RED for the unencoded and [[4,2,2]]-encoded ansatzes.

Resources	**Unencoded**	**[[4,2,2]]-Encoded**
Shots	2×62700	2×188000
Parallel Circuits per Run	3	0
Number of qubits per Ansatz with [3,1]-RED	6	18
Number of qubits per Run with [3,1]-RED	18	18
Max. Single-qubit Gates per Run	9	7
Two-qubit Gates per Run	18	25
Measurements per Run	18	18
Estimated Total Runtime	8.5 hrs	1.5 days
Expected cost of credits	10200	31400

considered when evaluating the cost of implementing such benchmarks on commercial devices, such as, Quantinuum. The cost of credits is calculated by the emulator using the formula shown in equation 6.2 and is provided by Quantinuum in their product data sheet.

$$HQC = 5 + \frac{N_{1q} + 10N_{2q} + 5N_m}{5000}C \tag{6.2}$$

where $N_{1q}, N_{2q} and N_m$ are number of native single-qubit gates, two-qubit gates and state preparation and measurement operations in the circuit, respectively and C is the number of shots. The product data sheet also suggests that the estimated run time for circuits is about an hour for circuits that require between 500 to 1200 HQCs, which depends on different factors such as the number of the connectivity required for the circuit and the dynamic calibrations of the system. The estimated total runtime in **Table 6.5** have been calculated by assuming execution of circuits worth 1200 credits per hour for the simple unencoded ansatz and about 800 credits per hour, the average of the two extremes of 500 and 1200, for the slightly more complicated encoded circuit.

6.5 Discussion

The results indicate that using error detection for mitigating the dominant sources of error can enable the estimates to reach the targeted level of accuracy and precision, which is chemical accuracy in this case. While combating just the gate error using the [[4,2,2]]-encoding with post-selection lowers the energy estimate and brings it closer to the exact energy without RED, the unencoded energy estimate results in a lower energy than the best post-selection strategy for the encoded ansatz, the PSAP energy estimate. Both ansatzes result in lower energies with RED. Using RED in addition to the PSAP method of the [[4,2,2]]-encoded ansatz results in an estimate of energy that is nearly 1 mHa lower than the best unencoded energy estimate and within chemical accuracy.

Improvement in the accuracy of the energy estimate with the [3,1]-RED compared to the [2,1]-RED indicates residual read out errors that were left undetected by the latter. Numerical simulations of the same [[4,2,2]]-encoded ansatz for molecular hydrogen with an isotropic two-qubit depolarizing error rate indicated that the threshold at which the energy estimate reached chemical accuracy was 0.09% as per results shown in **Figure 5.5**. The error model did not include read out error. The Quantinuum emulator error model not only considers an asymmetric depolarizing error channel but also includes leakage by spontaneous emission as part of the depolarizing error model. The energy estimate reaching chemical accuracy with the [3,1]-RED suggests that the read out error was nearly completely eliminated and that the [[4,2,2]]-encoding is at least as effective at detecting errors with this depolarizing error model as with the isotropic error model. Additionally, even though the other error sources listed in **Table 6.2** are an order(s) of magnitude lower than the leading error sources, they were not considered in the numerical simulations in Chapter 5 and yet resulted in a similar estimate indicating that they did not have as much of an effect on decreasing the accuracy.

Increase in the energy estimate of the unencoded ansatz with the [3,1]-RED compared to the [2,1]-RED in contrast to the [[4,2,2]]-encoded ansatz is the combined effect of the assymmetry in the read out error rate between measurement of qubits in state $|1\rangle$ and $|0\rangle$, and the target state being measured. This effect is amplified for a two-qubit target state with even parity, as in the case of the unencoded ansatz, and minimized in the case of the [[4,2,2]]-encoded ansatz. Nearly 50% of the measurements of the target state prepared by the unencoded ansatz will involve the $|00\rangle$ state and read out error rate for incorrectly measuring a qubit in state $|0\rangle$ is nearly as low as the two-qubit gate error rate as shown in **Table 6.2**. As more read out qubits are added, the effect of the two qubit error rate will dominate when measuring the state $|00\rangle$ and result in increasingly lower accuracy of the estimated energy. The [3,1]-RED yielded in an energy estimate lower than the corresponding estimate without RED for the unencoded ansatz due effective RED for the $|11\rangle$ state. On the other hand, measurement of any state prepared by the [[4,2,2]]-encoded ansatz, by design of the codespace, includes equal proportion of qubits in states $|1\rangle$ and $|0\rangle$. This results in an improvement in accuracy for every measurement due to mitigation of the much higher error rates associated with measuring qubits in state $|1\rangle$.

Precision in addition to accuracy is an important part of this benchmark and results indicate that both error detection strategies, [[4,2,2]] and [3,1]-RED not only improve accuracy but do not decrease the precision of the calculation. This is particularly remarkable when considering that the number of samples used to calculate the energy estimate is nearly half as many as that used for the unencoded ansatz but results in only ∼0.2 mHa increase in standard error with a significant improvement in accuracy. The need to run as many samples as the unencoded ansatz despite reaching chemical accuracy with half as many samples is due to the use of gate teleportation.

As an application benchmark, the study demonstrates that effectively removing errors in every sample measurement using methods such as quantum error detection and read out error detection can sufficiently manage dominant sources of errors typically found in current commercial devices and lead to the targeted accuracy if the error rate is sufficiently low. However, as can be seen from the resource analysis, the benchmark with error detection leads to a large increase in resource overhead with a three-fold increase in the number of qubits and two-qubit gates alone compared to the unencoded ansatz not to mention the corresponding increase in the cost to use the device. Such an increase in resources suggests that scaling up the benchmark exactly as it is to systems of larger scale may be prohibitive.

Resource scaling depends both on the choice of ansatz and the quantum error detection or correction scheme. The analysis is presented for the smallest molecular system using the smallest error detection code for a device with all-to-all connectivity, making it the best case scenario in terms of resources required. Increase in size of the molecular system, constraints in device connectivity, and change in quantum error correction/detection code will inevitably lead to an increase in the resources required. While the study demonstrates that the methods lead to an effective benchmark, innovative methods to optimize the scaling of resources with increase in system size are needed for such benchmarks to be applicable for more useful larger scale benchmarks across device architectures especially as technologies grow and error rates become lower. In this study itself, implementation of the rotation gate in the [[4,2,2]]-encoded ansatz without the consequence of losing nearly half the samples in the process would have led to a decrease in at least one of the resources: number of samples or shots compared to the unencoded ansatz. Similarly, optimizing ansatzes, using flag qubits to reduce overhead of larger quantum error correction codes, and combining other error mitigation techniques may be potential avenues for future work to improve the resource overhead of the benchmark presented here with increase in system size.

6.6 Conclusion

We have presented results from noisy simulations of the ground state of molecular hydrogen using VQE on the emulator of a commercial quantum computing device, the Quantinuum H1-1E emulator. The aim was to evaluate the outcomes against the benchmark of chemical accuracy defined as the estimated energy being within 1.6 mHa of the exact energy by using the [[4,2,2]] quantume error detection code and RED with post-selection to mitigate gate depolarizing error and read out error, respectively. We found that the results demonstrate the improvement in the accuracy and precision of energy estimates with the best estimate reaching chemical accuracy indicating effective mitigation of both gate and read out error. The two-qubit gate error rate of the emulator at 0.088% is slightly lower than the error rate reported to be the threshold, assessed by numerical simulations, at which the

[[4,2,2]]-encoded ansatz resulted in an energy estimate within chemical accuracy for molecular hydrogen in chapter 5. This indicates the read out error was sufficiently removed with the [3,1]-RED code, which was the only method to result in energy estimates within chemical accuracy.

The proposed framework for benchmarking a device is an investigation of accuracy of a small quantum application on a quantum device. As described earlier, computational accuracy of a device is characterized both by the difference in magnitude of estimated outcome from the exact outcome and the precision of the estimate. The latter is an indication of how reproducible the accuracy is on the given device. Error mitigation techniques typically are applied to the estimated average and the improvement in the accuracy often leads to an increase in variance Endo et al. (2021). The proposed framework improves both accuracy and precision by removing detected errors from every measured sample prior to calculating the average. Using additional error detection for combating read out error maintains this structure and similarly improves accuracy without decreasing the precision of the estimate. The scaling of resources with system size is the main limiting factor of this benchmark and we defer studies to improve this scaling to future work.

Chapter 7

Conclusion

Noise in quantum computers is a major roadblock to achieving quantum advantage in quantum computers. As discussed in the introduction, the promised advantage is exponential scaling in storage and speed-up in runtime for algorithms that are considered as yet intractable on classical computers. However, such speed-ups are only valuable if they are accompanied by the required accuracy. In this thesis we have explored the impact of noise on a specific quantum computing application and presented a benchmark for evaluating the performance of near-term quantum computers in terms of accuracy of a given computation. We have presented results for small quantum chemistry simulations using a quantum-classical hybrid algorithm, the variational quantum eigensolver (VQE), designed for near-term quantum computers.

In the first two studies, we explored the impact of standard single- and two-qubit gate depolarizing noise on the fidelity of the prepared state, and the accuracy and precision of estimating the energy for the ground state of sodium hydride using numerical simulations. We also investigated the change in impact of noise with different ansatzes and different optimizers. We then evaluated the use of quantum error detection for mitigating gate depolarizing error, reducing logical error rates and reaching chemical accuracy in estimating the ground state energy of molecular hydrogen using VQE. Finally, we develop a framework to evaluate the computational accuracy of a quantum device with chemical accuracy as the target accuracy benchmark and quantum error detection (QED) and read out error detection (ROD) as the techniques for mitigating the leading sources of noise, read out and two-qubit gate error, in the Quantinuum device considered.

From our studies on the impact of gate depolarizing error, we determined that gate depth was the most significant determining factor of error in energy and fidelity across all these ansatzes. Increase in gate depth increased error in energy and decreased the fidelity of the state prepared with the number of two-qubit CNOT gates being the leading contributor. Compared to the fixed ansatzes, the dynamically generated ansatzes as in the ADAPT-VQE method fluctuate in gate depth and number of parameters that lead to a significantly higher increase in error in energy and decrease in fidelity compared to the fixed depth ansatzes. We found that the optimizers we compared, L-BFGS and COBYLA, yielded different optimal parameters for the ansatzes but The influence on the outcomes of the fidelity and energy was very small or negligible.

Using quantum error detection with post-selection to mitigate gate depolarizing error had a significant impact on the logical error rates and accuracy of the energy estimated under noisy simulations for the ground state simulation of molecular hydrogen. We found that the magnitude of improvement in energy accuracy and fidelity varied between the different post-selection strategies involved with the PSAP leading in contribution. Significantly, we determined that the PSAP outcome reached within chemical accuracy at a higher threshold of depolarizing noise than the corresponding unencoded ansatz. Additionally, we found that the variance of the calculation for both the unencoded and encoded ansatzes were similar with standard error being influenced less by post-selection due to error detection and more by the use of an ancilla for gate teleportation of the rotation gate.

Finally, we found that the logical error rate in the encoded ansatz was much lower in probability than the total error rate in the circuit. However, using the ancilla for additional post-selection enables a reduction in both the overall error rate and the logical error-rate indicating the detection of Pauli errors of weight¿1.

With these results, we proceeded to develop a framework to benchmark the computational accuracy of a near-term quantum computing device by including ROD in addition [[4,2,2]]-QED for read out error mitigation and demonstrated the resource analysis to perform such a benchmark on near-quantum hardware by using the Quantinuum H1-1E emulator which is meant to mimic the actual Quantinuum H1-1 device in terms of the noise sources. We found a dramatic reduction in energy estimates for the [[4,2,2]]-encoded ansatz with post-selection, with slight improvement in energy for the unencoded ansatz, when simulated with ROD than without. While none of the estimates for the unencoded ansatz reached chemical accuracy, the best estimate for the [[4,2,2]]-encoded ansatz reached chemical accuracy with the [3,1]-ROD code.

The outcomes indicate that the 18-qubit [[4,2,2]]-encoded circuit has outperformed the 6-qubit unencoded circuit even though the latter has nearly three times as many two-qubit gates and qubits as the unencoded circuit. The [[4,2,2]]-QED and ROD have essentially nullified the impact of both the additional qubit and gate overhead while effectively mitigating the read out error and sufficiently mitigating gate errors. The high accuracy and precision of the resulting estimated energy indicate that the targeted accuracy benchmark is reproducible.

We have developed a framework that achieves the domain specific accuracy threshold of a leading quantum computing application with high precision by effectively managing the dominant sources of error, typically found in near-term quantum computers, with error detection. However, the framework has been applied to a very small problem that can be easily solved analytically and the resources required to achieve the benchmark scale prohibitively with system size. Avenues for improving the resource overhead with increase in system size include but are not limited to optimization of ansatzes to improve sampling overhead and development of hardware specific and/or application oriented error correction and detection codes and mitigation techniques that do not improve the accuracy at the cost of precision. The promise of quantum computing for large scale quantum applications is only feasible if the targeted accuracy is achieved and reproducible. This makes application oriented benchmarks invaluable and improving the feasibility of such benchmarks a significant area of current and future work.

Bibliography

Abraham, H., AduOffei, Agarwal, R., Akhalwaya, I. Y., Aleksandrowicz, G., Alexander, T., Amy, M., Arbel, E., Arijit02, Asfaw, A., Avkhadiev, A., Azaustre, C., AzizNgoueya, et al. (2019). Qiskit: An open-source framework for quantum computing. 42

Abrams, D. S. and Lloyd, S. (1999). Quantum Algorithm Providing Exponential Speed Increase for Finding Eigenvalues and Eigenvectors. *Physical Review Letters*, 83(24):5162–5165. 4

Acharya, R., Aleiner, I., Allen, R., Andersen, T. I., Ansmann, M., Arute, F., Arya, K., Asfaw, A., Atalaya, J., Babbush, R., Bacon, D., Bardin, J. C., Basso, J., Bengtsson, A., Boixo, S., Bortoli, G., Bourassa, A., Bovaird, J., Brill, L., Broughton, M., Buckley, B. B., Buell, D. A., Burger, T., Burkett, B., Bushnell, N., Chen, Y., Chen, Z., Chiaro, B., Cogan, J., Collins, R., Conner, P., Courtney, W., Crook, A. L., Curtin, B., Debroy, D. M., Del Toro Barba, A., Demura, S., Dunsworth, A., Eppens, D., Erickson, C., Faoro, L., Farhi, E., Fatemi, R., Flores Burgos, L., Forati, E., Fowler, A. G., Foxen, B., Giang, W., Gidney, C., Gilboa, D., Giustina, M., Grajales Dau, A., Gross, J. A., Habegger, S., Hamilton, M. C., Harrigan, M. P., Harrington, S. D., Higgott, O., Hilton, J., Hoffmann, M., Hong, S., Huang, T., Huff, A., Huggins, W. J., Ioffe, L. B., Isakov, S. V., Iveland, J., Jeffrey, E., Jiang, Z., Jones, C., Juhas, P., Kafri, D., Kechedzhi, K., Kelly, J., Khattar, T., Khezri, M., Kieferová, M., Kim, S., Kitaev, A., Klimov, P. V., Klots, A. R., Korotkov, A. N., Kostritsa, F., Kreikebaum, J. M., Landhuis, D., Laptev, P., Lau, K.-M., Laws, L., Lee, J., Lee, K., Lester, B. J., Lill, A., Liu, W., Locharla, A., Lucero, E., Malone, F. D., Marshall, J., Martin, O., McClean, J. R., McCourt, T., McEwen, M., Megrant, A., Meurer Costa, B., Mi, X., Miao, K. C., Mohseni, M., Montazeri, S., Morvan, A., Mount, E., Mruczkiewicz, W., Naaman, O., Neeley, M., Neill, C., Nersisyan, A., Neven, H., Newman, M., Ng, J. H., Nguyen, A., Nguyen, M., Niu, M. Y., O'Brien, T. E., Opremcak, A., Platt, J., Petukhov, A., Potter, R., Pryadko, L. P., Quintana, C., Roushan, P., Rubin, N. C., Saei, N., Sank, D., Sankaragomathi, K., Satzinger, K. J., Schurkus, H. F., Schuster, C., Shearn, M. J., Shorter, A., Shvarts, V., Skruzny, J., Smelyanskiy, V., Smith, W. C., Sterling, G., Strain, D., Szalay, M., Torres, A., Vidal, G., Villalonga, B., Vollgraff Heidweiller, C., White, T., Xing, C., Yao, Z. J., Yeh, P., Yoo, J., Young, G., Zalcman, A., Zhang, Y., Zhu, N., and Google Quantum AI (2023). Suppressing quantum errors by scaling a surface code logical qubit. *Nature*, 614(7949):676–681. 7, 78, 119

Adami, C. and Cerf, N. J. (1999). Quantum Computation with Linear Optics. In Williams, C. P., editor, *Quantum Computing and Quantum Communications*, pages 391–401, Berlin, Heidelberg. Springer. 5

Aharonov, D. and Ben-Or, M. (1997). Fault-tolerant quantum computation with constant error. In *Proceedings of the twenty-ninth annual ACM symposium on Theory of computing*, pages 176–188. 7

Aharonov, D., van Dam, W., Kempe, J., Landau, Z., Lloyd, S., and Regev, O. (2008). Adiabatic Quantum Computation Is Equivalent to Standard Quantum Computation. *SIAM Review*, 50(4):755–787. Publisher: Society for Industrial and Applied Mathematics. 4

AI, G. Q. (2023). Suppressing quantum errors by scaling a surface code logical qubit. *Nature*, 614(7949):676–681. 7, 78, 119

Aliferis, P., Gottesman, D., and Preskill, J. (2007). Accuracy threshold for postselected quantum computation. *arXiv preprint quant-ph/0703264*. 9

Arute, F., Arya, K., Babbush, R., Bacon, D., Bardin, J. C., Barends, R., Biswas, R., Boixo, S., Brandao, F. G. S. L., Buell, D. A., Burkett, B., Chen, Y., Chen, Z., Chiaro, B., Collins, R., Courtney, W., Dunsworth, A., Farhi, E., Foxen, B., Fowler, A., Gidney, C., Giustina, M., Graff, R., Guerin, K., Habegger, S., Harrigan, M. P., Hartmann, M. J., Ho, A., Hoffmann, M., Huang, T., Humble, T. S., Isakov, S. V., Jeffrey, E., Jiang, Z., Kafri, D., Kechedzhi, K., Kelly, J., Klimov, P. V., Knysh, S., Korotkov, A., Kostritsa, F., Landhuis, D., Lindmark, M., Lucero, E., Lyakh, D., Mandrà, S., McClean, J. R., McEwen, M., Megrant, A., Mi, X., Michielsen, K., Mohseni, M., Mutus, J., Naaman, O., Neeley, M., Neill, C., Niu, M. Y., Ostby, E., Petukhov, A., Platt, J. C., Quintana, C., Rieffel, E. G., Roushan, P., Rubin, N. C., Sank, D., Satzinger, K. J., Smelyanskiy, V., Sung, K. J., Trevithick, M. D., Vainsencher, A., Villalonga, B., White, T., Yao, Z. J., Yeh, P., Zalcman, A., Neven, H., and Martinis, J. M. (2019). Quantum supremacy using a programmable superconducting processor. *Nature*, 574(7779):505–510. Publisher: Nature Publishing Group. 6

Arute, F., Arya, K., Babbush, R., Bacon, D., Bardin, J. C., Barends, R., Boixo, S., Broughton, M., Buckley, B. B., Buell, D. A., et al. (2020). Hartree-fock on a superconducting qubit quantum computer. *arXiv preprint arXiv:2004.04174*. 36, 52

Aspect, A., Dalibard, J., and Roger, G. (1982). Experimental Test of Bell's Inequalities Using Time- Varying Analyzers. *Physical Review Letters*, 49(25):1804–1807. 20

Aspuru-Guzik, A., Dutoi, A. D., Love, P. J., and Head-Gordon, M. (2005). Simulated Quantum Computation of Molecular Energies. *Science*, 309(5741):1704–1707. Publisher: American Association for the Advancement of Science. 3, 25

Barenco, A., Bennett, C. H., Cleve, R., DiVincenzo, D. P., Margolus, N., Shor, P., Sleator, T., Smolin, J. A., and Weinfurter, H. (1995). Elementary gates for quantum computation. *Physical review A*, 52(5):3457. 85

Barends, R., Kelly, J., Megrant, A., Sank, D., Jeffrey, E., Chen, Y., Yin, Y., Chiaro, B., Mutus, J., Neill, C., O'Malley, P., Roushan, P., Wenner, J., White, T. C., Cleland, A. N., and Martinis, J. M. (2013). Coherent Josephson Qubit Suitable for Scalable Quantum Integrated Circuits. *Physical Review Letters*, 111(8):080502. 5

Barkoutsos, P. K., Gonthier, J. F., Sokolov, I., Moll, N., Salis, G., Fuhrer, A., Ganzhorn, M., Egger, D. J., Troyer, M., Mezzacapo, A., Filipp, S., and Tavernelli, I. (2018). Quantum algorithms for electronic structure calculations: Particle-hole hamiltonian and optimized wave-function expansions. *Phys. Rev. A*, 98:022322. 57

Bartlett, R. J., Kucharski, S. A., and Noga, J. (1989). Alternative coupled-cluster ansätze ii. the unitary coupled-cluster method. *Chemical physics letters*, 155(1):133–140. 27, 84

Bauer, B., Bravyi, S., Motta, M., and Chan, G. K.-L. (2020). Quantum algorithms for quantum chemistry and quantum materials science. *Chemical Reviews*, 120(22):12685–12717. 52

Bauman, N. P., Low, G. H., and Kowalski, K. (2019). Quantum simulations of excited states with active-space downfolded hamiltonians. *The Journal of chemical physics*, 151(23):234114. 53

Beale, S. J., Carignan-Dugas, A., Dahlen, D., Emerson, J., Hincks, I., Iyer, P., Jain, A., Hufnagel, D., Ospadov, E., Saunders, J., Stasiuk, A., Wallman, J. J., and Winick, A. (2020a). True-q. 44

Beale, S. J., Carignan-Dugas, A., Dahlen, D., Emerson, J., Hincks, I., Iyer, P., Jain, A., Hufnagel, D., Ospadov, E., Saunders, J., Stasiuk, A., Wallman, J. J., and Winick, A. (2020b). True-q. 62

Bell, J. S. (1964). On the Einstein Podolsky Rosen paradox. *Physics Physique Fizika*, 1(3):195–200. 19

Bernien, H., Schwartz, S., Keesling, A., Levine, H., Omran, A., Pichler, H., Choi, S., Zibrov, A. S., Endres, M., Greiner, M., Vuletić, V., and Lukin, M. D. (2017). Probing many-body dynamics on a 51-atom quantum simulator. *Nature*, 551(7682):579–584. Publisher: Nature Publishing Group. 6

Beverland, M. E., Murali, P., Troyer, M., Svore, K. M., Hoefler, T., Kliuchnikov, V., Low, G. H., Soeken, M., Sundaram, A., and Vaschillo, A. (2022). Assessing requirements to scale to practical quantum advantage. *arXiv preprint arXiv:2211.07629*. 119

Blatt, R. and Wineland, D. (2008). Entangled states of trapped atomic ions. *Nature*, 453(7198):1008–1015. Publisher: Nature Publishing Group. 5

Bluvstein, D., Evered, S. J., Geim, A. A., Li, S. H., Zhou, H., Manovitz, T., Ebadi, S., Cain, M., Kalinowski, M., Hangleiter, D., Bonilla Ataides, J. P., Maskara, N., Cong, I., Gao, X., Sales Rodriguez, P., Karolyshyn, T., Semeghini, G., Gullans, M. J., Greiner, M., Vuletić, V., and Lukin, M. D. (2024). Logical quantum processor based on reconfigurable atom arrays. *Nature*, 626(7997):58–65. Publisher: Nature Publishing Group. 7

Bohm, D. (1952). A Suggested Interpretation of the Quantum Theory in Terms of "Hidden" Variables. I. *Physical Review*, 85(2):166–179. Publisher: American Physical Society. 19

Bonet-Monroig, X., Sagastizabal, R., Singh, M., and O'Brien, T. E. (2018). Low-cost error mitigation by symmetry verification. *Physical Review A*, 98(6):062339. 8

Braunstein, S. L. and Van Loock, P. (2005). Quantum information with continuous variables. *Reviews of Modern Physics*, 77(2):513–577. 4

Bravyi, S., Cross, A. W., Gambetta, J. M., Maslov, D., Rall, P., and Yoder, T. J. (2024). High-threshold and low-overhead fault-tolerant quantum memory. 78

Calderbank, A. R. and Shor, P. W. (1996). Good quantum error-correcting codes exist. *Physical Review A*, 54(2):1098. 5, 78

Cao, Y., Romero, J., Olson, J. P., Degroote, M., Johnson, P. D., Kieferová, M., Kivlichan, I. D., Menke, T., Peropadre, B., Sawaya, N. P., et al. (2019a). Quantum chemistry in the age of quantum computing. *Chemical reviews*, 119(19):10856–10915. 38, 52

Cao, Y., Romero, J., Olson, J. P., Degroote, M., Johnson, P. D., Kieferová, M., Kivlichan, I. D., Menke, T., Peropadre, B., Sawaya, N. P. D., Sim, S., Veis, L., and Aspuru-Guzik, A. (2019b). Quantum Chemistry in the Age of Quantum Computing. *Chemical Reviews*, 119(19):10856–10915. Publisher: American Chemical Society. 3, 80, 82, 83, 120

Capdevila-Cortada, M. (2019). Electrifying the Haber–Bosch. *Nature Catalysis*, 2(12):1055–1055. Publisher: Nature Publishing Group. 2

Cerezo, M., Arrasmith, A., Babbush, R., Benjamin, S. C., Endo, S., Fujii, K., McClean, J. R., Mitarai, K., Yuan, X., Cincio, L., et al. (2021). Variational quantum algorithms. *Nature Reviews Physics*, 3(9):625–644. 83

Chen, E. H., Yoder, T. J., Kim, Y., Sundaresan, N., Srinivasan, S., Li, M., Córcoles, A. D., Cross, A. W., and Takita, M. (2022). Calibrated Decoders for Experimental Quantum Error Correction. *Physical Review Letters*, 128(11):110504. 79

Claudino, D., Peng, B., Bauman, N. P., Kowalski, K., and Humble, T. S. (2021). Improving the accuracy and efficiency of quantum connected moments expansions. *arXiv preprint arXiv:2103.09124*. 52

Claudino, D., Wright, J., McCaskey, A. J., and Humble, T. S. (2020). Benchmarking adaptive variational quantum eigensolvers. *Frontiers in Chemistry*, 8:1152. 36, 53, 60

Clauser, J. F., Horne, M. A., Shimony, A., and Holt, R. A. (1969). Proposed Experiment to Test Local Hidden-Variable Theories. *Physical Review Letters*, 23(15):880–884. 19

Colless, J. I., Ramasesh, V. V., Dahlen, D., Blok, M. S., Kimchi-Schwartz, M. E., McClean, J. R., Carter, J., de Jong, W. A., and Siddiqi, I. (2018a). Computation of molecular spectra on a quantum processor with an error-resilient algorithm. *Physical Review X*, 8(1):011021. 80, 85

Colless, J. I., Ramasesh, V. V., Dahlen, D., Blok, M. S., McClean, J. R., Carter, J., de Jong, W. A., and Siddiqi, I. (2018b). Robust determination of molecular spectra on a quantum processor. *Physical Review X*, 8(1):011021. arXiv:1707.06408 [quant-ph]. 80

Córcoles, A. D., Magesan, E., Srinivasan, S. J., Cross, A. W., Steffen, M., Gambetta, J. M., and Chow, J. M. (2015). Demonstration of a quantum error detection code using a square lattice of four superconducting qubits. *Nature communications*, 6(1):6979. 5, 79, 119

Cory, D. G., Fahmy, A. F., and Havel, T. F. (1997). Ensemble quantum computing by NMR spectroscopy. *Proceedings of the National Academy of Sciences*, 94(5):1634–1639. 5

Curtin, R. R., Edel, M., Lozhnikov, M., Mentekidis, Y., Ghaisas, S., and Zhang, S. (2018). mlpack 3: a fast, flexible C++ machine learning library. *Journal of Open Source Software*, 3:726. 65

Da Silva, M., Ryan-Anderson, C., Bello-Rivas, J., Chernoguzov, A., Dreiling, J., Foltz, C., Gaebler, J., Gatterman, T., Hayes, D., Hewitt, N., et al. (2024).

Demonstration of logical qubits and repeated error correction with better-than-physical error rates. *arXiv preprint arXiv:2404.02280*. 119

Dahlhauser, M. L. and Humble, T. S. (2021). Modeling noisy quantum circuits using experimental characterization. *Physical Review A*, 103(4):042603. 64

Daniel, C., J, M. A., and I, L. D. (2022). A Backend-agnostic, Quantum-classical Framework for Simulations of Chemistry in C++. *ACM Transactions on Quantum Computing*. Publisher: ACMPUB27New York, NY. 34, 92

Dasgupta, S. and Humble, T. S. (2021). Stability of noisy quantum computing devices. arXiv:2105.09472 [quant-ph]. 9

Devitt, S. J., Munro, W. J., and Nemoto, K. (2013). Quantum error correction for beginners. *Reports on Progress in Physics*, 76(7):076001. 9, 28, 29, 32, 78, 87

Devoret, M. H. and Schoelkopf, R. J. (2013). Superconducting Circuits for Quantum Information: An Outlook. *Quantum Information Processing*, 339. 5

Devoret, M. H., Wallraff, A., and Martinis, J. M. (2004). Superconducting qubits: A short review. *arXiv preprint cond-mat/0411174*. 5

Doherty, M. W., Manson, N. B., Delaney, P., Jelezko, F., Wrachtrup, J., and Hollenberg, L. C. L. (2013). The nitrogen-vacancy colour centre in diamond. *Physics Reports*, 528(1):1–45. 5

Einstein, A., Podolsky, B., and Rosen, N. (1935). Can Quantum-Mechanical Description of Physical Reality Be Considered Complete? *Physical Review*, 47(10):777–780. 19

Elfving, V. E., Broer, B. W., Webber, M., Gavartin, J., Halls, M. D., Lorton, K. P., and Bochevarov, A. (2020). How will quantum computers provide an industrially relevant computational advantage in quantum chemistry? arXiv:2009.12472 [physics, physics:quant-ph]. 3

Elfving, V. E., Millaruelo, M., Gámez, J. A., and Gogolin, C. (2021). Simulating quantum chemistry in the seniority-zero space on qubit-based quantum computers. *Physical Review A*, 103(3):032605. 53

Endo, S., Cai, Z., Benjamin, S. C., and Yuan, X. (2021). Hybrid quantum-classical algorithms and quantum error mitigation. *Journal of the Physical Society of Japan*, 90(3):032001. 147

Erhard, A., Wallman, J. J., Postler, L., Meth, M., Stricker, R., Martinez, E. A., Schindler, P., Monz, T., Emerson, J., and Blatt, R. (2019). Characterizing large-scale quantum computers via cycle benchmarking. *Nature communications*, 10(1):1–7. 37

Evangelista, F. A., Chan, G. K.-L., and Scuseria, G. E. (2019). Exact parameterization of fermionic wave functions via unitary coupled cluster theory. *The Journal of Chemical Physics*, 151(24):244112. 27, 84

Evered, S. J., Bluvstein, D., Kalinowski, M., Ebadi, S., Manovitz, T., Zhou, H., Li, S. H., Geim, A. A., Wang, T. T., Maskara, N., et al. (2023). High-fidelity parallel entangling gates on a neutral atom quantum computer. *arXiv preprint arXiv:2304.05420*. 7, 78

Farhi, E., Goldstone, J., and Gutmann, S. (2014). A quantum approximate optimization algorithm. *arXiv preprint arXiv:1411.4028*. 8

Farhi, E., Goldstone, J., Gutmann, S., and Sipser, M. (2000). Quantum Computation by Adiabatic Evolution. arXiv:quant-ph/0001106. 4

Fauseweh, B. and Zhu, J.-X. (2021). Digital quantum simulation of non-equilibrium quantum many-body systems. *Quantum Information Processing*, 20(4):138. 10

Feynman, R. P. (1982). Simulating physics with computers. *International Journal of Theoretical Physics*, 21(6):467–488. 4

Fowler, A. G., Mariantoni, M., Martinis, J. M., and Cleland, A. N. (2012). Surface codes: Towards practical large-scale quantum computation. *Phys. Rev. A*, 86:032324. 7, 78

Gambetta, J. M., Chow, J. M., and Steffen, M. (2017). Building logical qubits in a superconducting quantum computing system. *npj Quantum Information*, 3(1):1–7. Publisher: Nature Publishing Group. 6

Gard, B. T., Zhu, L., Barron, G. S., Mayhall, N. J., Economou, S. E., and Barnes, E. (2020). Efficient symmetry-preserving state preparation circuits for the variational quantum eigensolver algorithm. *npj Quantum Information*, 6(1):1–9. 53

Gershenfeld, N. A. and Chuang, I. L. (1997). Bulk Spin-Resonance Quantum Computation. *Science*, 275(5298):350–356. 5

Google AI Quantum, Arute, F., Arya, K., Babbush, R., Bacon, D., Bardin, J. C., Barends, R., Boixo, S., Broughton, M., Buckley, B. B., Buell, D. A., Burkett, B., Bushnell, N., Chen, Y., Chen, Z., Chiaro, B., Collins, R., Courtney, W., Demura, S., Dunsworth, A., Farhi, E., Fowler, A., Foxen, B., Gidney, C., Giustina, M., Graff, R., Habegger, S., Harrigan, M. P., Ho, A., Hong, S., Huang, T., Huggins, W. J., Ioffe, L., Isakov, S. V., Jeffrey, E., Jiang, Z., Jones, C., Kafri, D., Kechedzhi, K., Kelly, J., Kim, S., Klimov, P. V., Korotkov, A., Kostritsa, F., Landhuis, D., Laptev, P., Lindmark, M., Lucero, E., Martin, O., Martinis, J. M., McClean, J. R., McEwen, M., Megrant, A., Mi, X., Mohseni, M., Mruczkiewicz, W., Mutus, J., Naaman, O., Neeley, M., Neill, C., Neven, H., Niu, M. Y., O'Brien, T. E., Ostby, E., Petukhov, A., Putterman, H., Quintana, C., Roushan, P., Rubin, N. C., Sank, D., Satzinger, K. J., Smelyanskiy, V., Strain, D., Sung, K. J., Szalay, M., Takeshita, T. Y., Vainsencher, A., White, T., Wiebe, N., Yao, Z. J., Yeh, P., and Zalcman, A. (2020). Hartree-Fock on a superconducting qubit quantum computer. *Science*, 369(6507):1084–1089. Publisher: American Association for the Advancement of Science. 10, 26

Gottesman, D. (2016). Quantum fault tolerance in small experiments. *arXiv preprint arXiv:1610.03507*. 79, 89, 90

Gowrishankar, M., Wright, J., Claudino, D., Nguyen, T., McCaskey, A., and Humble, T. (2021a). Numerical simulations of noisy variational quantum eigensolver ansatz circuits. *2021 IEEE Intl. Conf. on Quantum Computing and Engineering*. 74

Gowrishankar, M., Wright, J., Claudino, D., Nguyen, T., McCaskey, A., and Humble, T. S. (2021b). Numerical simulations of noisy variational quantum eigensolver ansatz circuits. In *2021 IEEE International Conference on Quantum Computing and Engineering (QCE)*, pages 155–159. IEEE. 83

Grimsley, H. R., Claudino, D., Economou, S. E., Barnes, E., and Mayhall, N. J. (2019a). Is the trotterized uccsd ansatz chemically well-defined? *Journal of chemical theory and computation*, 16(1):1–6. 26, 53

Grimsley, H. R., Claudino, D., Economou, S. E., Barnes, E., and Mayhall, N. J. (2020). Is the Trotterized UCCSD Ansatz Chemically Well-Defined? *Journal of Chemical Theory and Computation*, 16(1):1–6. Publisher: American Chemical Society. 82

Grimsley, H. R., Economou, S. E., Barnes, E., and Mayhall, N. J. (2019b). An adaptive variational algorithm for exact molecular simulations on a quantum computer. *Nature communications*, 10(1):1–9. 36, 53, 60, 61

Grover, L. K. (1997). Quantum Mechanics Helps in Searching for a Needle in a Haystack. *Physical Review Letters*, 79(2):325–328. 4

Hashim, A., Naik, R. K., Morvan, A., Ville, J.-L., Mitchell, B., Kreikebaum, J. M., Davis, M., Smith, E., Iancu, C., O'Brien, K. P., et al. (2020). Randomized compiling for scalable quantum computing on a noisy superconducting quantum processor. *arXiv preprint arXiv:2010.00215*. 8, 37

Hashim, A., Naik, R. K., Morvan, A., Ville, J.-L., Mitchell, B., Kreikebaum, J. M., Davis, M., Smith, E., Iancu, C., O'Brien, K. P., Hincks, I., Wallman, J. J., Emerson, J., and Siddiqi, I. (accepted, 2021). Randomized compiling for scalable quantum computing on a noisy superconducting quantum processor. *Phys. Rev. X*. 62

Hensen, B., Bernien, H., Dréau, A. E., Reiserer, A., Kalb, N., Blok, M. S., Ruitenberg, J., Vermeulen, R. F. L., Schouten, R. N., Abellán, C., Amaya, W., Pruneri, V., Mitchell, M. W., Markham, M., Twitchen, D. J., Elkouss, D., Wehner, S., Taminiau, T. H., and Hanson, R. (2015). Loophole-free Bell inequality violation using electron spins separated by 1.3 kilometres. *Nature*, 526(7575):682–686. Publisher: Nature Publishing Group. 20

Hicks, R., Kobrin, B., Bauer, C. W., and Nachman, B. (2022). Active readout-error mitigation. *Physical Review A*, 105(1):012419. Publisher: American Physical Society. 32, 122, 123

Hoffman, B. M., Lukoyanov, D., Yang, Z.-Y., Dean, D. R., and Seefeldt, L. C. (2014). Mechanism of Nitrogen Fixation by Nitrogenase: The Next Stage. *Chemical Reviews*, 114(8):4041–4062. Publisher: American Chemical Society. 2

Imamoglu, A., Awschalom, D. D., Burkard, G., DiVincenzo, D. P., Loss, D., Sherwin, M., and Small, A. (1999). Quantum Information Processing Using Quantum Dot Spins and Cavity QED. *Physical Review Letters*, 83(20):4204–4207. Publisher: American Physical Society. 5

Johnson, S. G. (2007). The nlopt nonlinear-optimization package. http://github.com/stevengj/nlopt. 65

Jordan, P. and Wigner, E. (1928). Über das Paulische Äquivalenzverbot. *Zeitschrift für Physik*, 47(9):631–651. 24

Kandala, A., Mezzacapo, A., Temme, K., Takita, M., Brink, M., Chow, J. M., and Gambetta, J. M. (2017). Hardware-efficient variational quantum eigensolver for small molecules and quantum magnets. *Nature*, 549(7671):242–246. 52

Kitaev, A. Y. (1997). Quantum computations: algorithms and error correction. *Russian Mathematical Surveys*, 52(6):1191. Publisher: IOP Publishing. 4

Knill, E. (2004). Fault-tolerant postselected quantum computation: Threshold analysis. *arXiv preprint quant-ph/0404104*. 9, 79

Knill, E. (2005). Quantum computing with realistically noisy devices. *Nature*, 434(7029):39–44. Number: 7029 Publisher: Nature Publishing Group. 79

Kok, P., Munro, W. J., Nemoto, K., Ralph, T. C., Dowling, J. P., and Milburn, G. J. (2007). Linear optical quantum computing with photonic qubits. *Reviews of Modern Physics*, 79(1):135–174. Publisher: American Physical Society. 5

Krinner, S., Lacroix, N., Remm, A., Di Paolo, A., Genois, E., Leroux, C., Hellings, C., Lazar, S., Swiadek, F., Herrmann, J., et al. (2022). Realizing repeated quantum error correction in a distance-three surface code. *Nature*, 605(7911):669–674. 7, 78, 119

Leung, D. W., Nielsen, M. A., Chuang, I. L., and Yamamoto, Y. (1997). Approximate quantum error correction can lead to better codes. *Physical Review A*, 56(4):2567–2573. 79

Li, Y. and Benjamin, S. C. (2017). Efficient variational quantum simulator incorporating active error minimization. *Physical Review X*, 7(2):021050. 8

Lidar, D. A. and Wang, H. (1999). Calculating the thermal rate constant with exponential speedup on a quantum computer. *Physical Review E*, 59(2):2429–2438. 3

Lim, H., Kang, D. H., Kim, J., Pellow-Jarman, A., McFarthing, S., Pellow-Jarman, R., Jeon, H.-N., Oh, B., Rhee, J.-K. K., and No, K. T. (2024). Fragment molecular orbital-based variational quantum eigensolver for quantum chemistry in the age of quantum computing. *Scientific Reports*, 14(1):1–13. 83

Linke, N. M., Gutierrez, M., Landsman, K. A., Figgatt, C., Debnath, S., Brown, K. R., and Monroe, C. (2017). Fault-tolerant quantum error detection. *Science advances*, 3(10):e1701074. 79, 119

Liu, D. C. and Nocedal, J. (1989). On the limited memory BFGS method for large scale optimization. *Mathematical Programming*, 45:503–528. 54, 65

Liu, J.-G., Zhang, Y.-H., Wan, Y., and Wang, L. (2019). Variational quantum eigensolver with fewer qubits. *Physical Review Research*, 1(2):023025. 83

Liu, X., Liu, G., Zhang, H.-K., Huang, J., and Wang, X. (2024). Mitigating barren plateaus of variational quantum eigensolvers. *IEEE Transactions on Quantum Engineering*. 83

Livingston, W. P., Blok, M. S., Flurin, E., Dressel, J., Jordan, A. N., and Siddiqi, I. (2022). Experimental demonstration of continuous quantum error correction. *Nature communications*, 13(1):2307. 7, 78, 119

Lloyd, S. (1996). Universal Quantum Simulators. *Science*, 273(5278):1073–1078. Publisher: American Association for the Advancement of Science. 3, 4

Lloyd, S. and Braunstein, S. L. (1999). Quantum Computation over Continuous Variables. *Physical Review Letters*, 82(8):1784–1787. 4

Loss, D. and DiVincenzo, D. P. (1998). Quantum computation with quantum dots. *Physical Review A*, 57(1):120–126. Publisher: American Physical Society. 5

Lostaglio, M. and Ciani, A. (2021). Error Mitigation and Quantum-Assisted Simulation in the Error Corrected Regime. *Physical Review Letters*, 127(20):200506. 119

Mandviwalla, A., Ohshiro, K., and Ji, B. (2018). Implementing Grover's Algorithm on the IBM Quantum Computers. In *2018 IEEE International Conference on Big Data (Big Data)*, pages 2531–2537. 11

Matoušek, M., Pernal, K., Pavošević, F., and Veis, L. (2024). Variational quantum eigensolver boosted by adiabatic connection. *The Journal of Physical Chemistry A*, 128(3):687–698. 83

Mayer, K., Ryan-Anderson, C., Brown, N., Durso-Sabina, E., Baldwin, C. H., Hayes, D., Dreiling, J. M., Foltz, C., Gaebler, J. P., Gatterman, T. M., Gerber, J. A., Gilmore, K., Gresh, D., Hewitt, N., Horst, C. V., Johansen, J., Mengle, T., Mills, M., Moses, S. A., Siegfried, P. E., Neyenhuis, B., Pino, J., and Stutz, R. (2024). Benchmarking logical three-qubit quantum Fourier transform encoded in the Steane code on a trapped-ion quantum computer. arXiv:2404.08616 [quant-ph]. 7, 78, 119

McArdle, S., Endo, S., Aspuru-Guzik, A., Benjamin, S. C., and Yuan, X. (2020). Quantum computational chemistry. *Rev. Mod. Phys.*, 92:015003. 2, 3, 24, 52

McCaskey, A. J., Lyakh, D. I., Dumitrescu, E. F., Powers, S. S., and Humble, T. S. (2020). XACC: a system-level software infrastructure for heterogeneous quantum–classical computing. *Quantum Science and Technology*, 5(2):024002. 34, 42, 61, 92

McCaskey, A. J., Parks, Z. P., Jakowski, J., Moore, S. V., Morris, T. D., Humble, T. S., and Pooser, R. C. (2019). Quantum chemistry as a benchmark for near-term quantum computers. *npj Quantum Information*, 5(1):1–8. xiii, 10, 26, 36, 38, 40, 52, 60, 61

McClean, J. R., Babbush, R., Love, P. J., and Aspuru-Guzik, A. (2014). Exploiting Locality in Quantum Computation for Quantum Chemistry. *The Journal of Physical Chemistry Letters*, 5(24):4368–4380. Publisher: American Chemical Society. 25

McClean, J. R., Kimchi-Schwartz, M. E., Carter, J., and De Jong, W. A. (2017). Hybrid quantum-classical hierarchy for mitigation of decoherence and determination of excited states. *Physical Review A*, 95(4):042308. 8

McClean, J. R., Romero, J., Babbush, R., and Aspuru-Guzik, A. (2016a). The theory of variational hybrid quantum-classical algorithms. *New Journal of Physics*, 18(2):023023. Publisher: IOP Publishing. 25

McClean, J. R., Romero, J., Babbush, R., and Aspuru-Guzik, A. (2016b). The theory of variational hybrid quantum-classical algorithms. *New Journal of Physics*, 18(2):023023. 52

McKay, D. C., Alexander, T., Bello, L., Biercuk, M. J., Bishop, L., Chen, J., Chow, J. M., Córcoles, A. D., Egger, D., Filipp, S., et al. (2018). Qiskit backend specifications for openqasm and openpulse experiments. *arXiv preprint arXiv:1809.03452*. 64

Metcalf, M., Bauman, N. P., Kowalski, K., and De Jong, W. A. (2020). Resource-efficient chemistry on quantum computers with the variational quantum eigensolver and the double unitary coupled-cluster approach. *Journal of chemical theory and computation*, 16(10):6165–6175. 53, 83

Mi, X., Benito, M., Putz, S., Zajac, D. M., Taylor, J. M., Burkard, G., and Petta, J. R. (2018). A coherent spin–photon interface in silicon. *Nature*, 555(7698):599–603. Publisher: Nature Publishing Group. 6

Mizukami, W., Mitarai, K., Nakagawa, Y. O., Yamamoto, T., Yan, T., and Ohnishi, Y.-y. (2020). Orbital optimized unitary coupled cluster theory for quantum computer. *Physical Review Research*, 2(3):033421. 53

Monroe, C. and Kim, J. (2013). Scaling the Ion Trap Quantum Processor. *Quantum Information Processing*, 339. 5

Motta, M., P. Gujarati, T., E. Rice, J., Kumar, A., Masteran, C., A. Latone, J., Lee, E., F. Valeev, E., and Y. Takeshita, T. (2020). Quantum simulation of electronic structure with a transcorrelated Hamiltonian: improved accuracy with a smaller footprint on the quantum computer. *Physical Chemistry Chemical Physics*, 22(42):24270–24281. Publisher: Royal Society of Chemistry. 10

Nam, Y., Chen, J.-S., Pisenti, N. C., Wright, K., Delaney, C., Maslov, D., Brown, K. R., Allen, S., Amini, J. M., Apisdorf, J., Beck, K. M., Blinov, A., Chaplin, V., Chmielewski, M., Collins, C., Debnath, S., Hudek, K. M., Ducore, A. M., Keesan, M., Kreikemeier, S. M., Mizrahi, J., Solomon, P., Williams, M., Wong-Campos, J. D., Moehring, D., Monroe, C., and Kim, J. (2020). Ground-state energy estimation of the water molecule on a trapped-ion quantum computer. *npj Quantum Information*, 6(1):33. 82

Nayak, C., Simon, S. H., Stern, A., Freedman, M., and Das Sarma, S. (2008). Non-Abelian anyons and topological quantum computation. *Reviews of Modern Physics*, 80(3):1083–1159. Publisher: American Physical Society. 5

Nielsen, M. A. and Chuang, I. L. (2010a). *Quantum computation and quantum information*. Cambridge university press. 5, 16

Nielsen, M. A. and Chuang, I. L. (2010b). *Quantum Computation and Quantum Information: 10th Anniversary Edition*. Cambridge University Press. 4, 85

Nocedal, J. (1980). Updating quasi-newton matrices with limited storage. *Math. Comp.*, 35:773–782. 54, 65

O'Malley, P. J. J., Babbush, R., Kivlichan, I. D., Romero, J., McClean, J. R., Barends, R., Kelly, J., Roushan, P., Tranter, A., Ding, N., Campbell, B., Chen, Y., Chen, Z., Chiaro, B., Dunsworth, A., Fowler, A. G., Jeffrey, E., Lucero, E., Megrant, A., Mutus, J. Y., Neeley, M., Neill, C., Quintana, C., Sank, D., Vainsencher, A., Wenner, J., White, T. C., Coveney, P. V., Love, P. J., Neven, H., Aspuru-Guzik, A., and Martinis, J. M. (2016). Scalable quantum simulation of molecular energies. *Phys. Rev. X*, 6:031007. 52

O'Malley, P., Babbush, R., Kivlichan, I., Romero, J., McClean, J., Barends, R., Kelly, J., Roushan, P., Tranter, A., Ding, N., Campbell, B., Chen, Y., Chen, Z., Chiaro, B., Dunsworth, A., Fowler, A., Jeffrey, E., Lucero, E., Megrant, A., Mutus, J., Neeley, M., Neill, C., Quintana, C., Sank, D., Vainsencher, A., Wenner, J., White, T., Coveney, P., Love, P., Neven, H., Aspuru-Guzik, A., and Martinis, J. (2016). Scalable Quantum Simulation of Molecular Energies. *Physical Review X*, 6(3):031007. 10, 80, 82

P, B. N., Chládek, J., Veis, L., Pittner, J., and Karol, K. (2021). Variational quantum eigensolver for approximate diagonalization of downfolded Hamiltonians using generalized unitary coupled cluster ansatz. *Quantum Science and Technology*, 6(3):034008. Publisher: IOP Publishing. 82

Park, C.-Y. (2024). Efficient ground state preparation in variational quantum eigensolver with symmetry-breaking layers. *APL Quantum*, 1(1). 83

Park, J. L. (1970). The concept of transition in quantum mechanics. *Foundations of Physics*, 1(1):23–33. 5

Parrish, R. M., Hohenstein, E. G., McMahon, P. L., and Martínez, T. J. (2019). Quantum computation of electronic transitions using a variational quantum eigensolver. *Physical review letters*, 122(23):230401. 83

Paudel, H. P., Syamlal, M., Crawford, S. E., Lee, Y.-L., Shugayev, R. A., Lu, P., Ohodnicki, P. R., Mollot, D., and Duan, Y. (2022). Quantum Computing and Simulations for Energy Applications: Review and Perspective. *ACS Engineering Au*, 2(3):151–196. Publisher: American Chemical Society. 3

Peruzzo, A., McClean, J., Shadbolt, P., Yung, M.-H., Zhou, X.-Q., Love, P. J., Aspuru-Guzik, A., and O'Brien, J. L. (2014a). A variational eigenvalue solver on a photonic quantum processor. *Nature Communications*, 5(1):4213. Number: 1 Publisher: Nature Publishing Group. 8, 10, 24, 26, 82, 83

Peruzzo, A., McClean, J., Shadbolt, P., Yung, M.-H., Zhou, X.-Q., Love, P. J., Aspuru-Guzik, A., and O'brien, J. L. (2014b). A variational eigenvalue solver on a photonic quantum processor. *Nature communications*, 5(1):1–7. 36, 38

Peterson, K. A., Feller, D., and Dixon, D. A. (2012). Chemical accuracy in ab initio thermochemistry and spectroscopy: current strategies and future challenges. *Theoretical Chemistry Accounts*, 131(1):1079. 3

Piveteau, C., Sutter, D., Bravyi, S., Gambetta, J. M., and Temme, K. (2021). Error Mitigation for Universal Gates on Encoded Qubits. *Physical Review Letters*, 127(20):200505. 119

Pokharel, B. and Lidar, D. A. (2024). Better-than-classical Grover search via quantum error detection and suppression. *npj Quantum Information*, 10(1):1–17. Publisher: Nature Publishing Group. 79, 120

Powell, M. J. (1998). Direct search algorithms for optimization calculations. *Acta numerica*, 7:287–336. 54, 65

Preskill, J. (2018a). Quantum Computing in the NISQ era and beyond. *Quantum*, 2:79. Publisher: Verein zur Förderung des Open Access Publizierens in den Quantenwissenschaften. 8

Preskill, J. (2018b). Quantum computing in the nisq era and beyond. *Quantum*, 2:79. 52

Ramanathan, C., Boulant, N., Chen, Z., Cory, D. G., Chuang, I., and Steffen, M. (2005). NMR Quantum Information Processing. In Everitt, H. O., editor, *Experimental Aspects of Quantum Computing*, pages 15–44. Springer US, Boston, MA. 5

Raussendorf, R. and Briegel, H. J. (2001). A One-Way Quantum Computer. *PHYSICAL REVIEW LETTERS*, 86(22). 4

Raussendorf, R., Browne, D. E., and Briegel, H. J. (2003). Measurement-based quantum computation on cluster states. *PHYSICAL REVIEW A*. 4

Reichardt, B. W. (2009). Error-Detection-Based Quantum Fault-Tolerance Threshold. *Algorithmica*, 55(3):517–556. 9, 79

Reiher, M., Wiebe, N., Svore, K. M., Wecker, D., and Troyer, M. (2017). Elucidating reaction mechanisms on quantum computers. *Proceedings of the National Academy of Sciences*, 114(29):7555–7560. Company: National Academy of Sciences Distributor: National Academy of Sciences Institution: National Academy of Sciences Label: National Academy of Sciences Publisher: Proceedings of the National Academy of Sciences. 2, 3

Rice, J. E., Gujarati, T. P., Motta, M., Takeshita, T. Y., Lee, E., Latone, J. A., and Garcia, J. M. (2021). Quantum computation of dominant products in lithium–sulfur batteries. *The Journal of Chemical Physics*, 154(13):134115. 3

Roffe, J., Headley, D., Chancellor, N., Horsman, D., and Kendon, V. (2018). Protecting quantum memories using coherent parity check codes. *Quantum Science and Technology*, 3(3):035010. 79, 119

Romero, J., Babbush, R., McClean, J. R., Hempel, C., Love, P. J., and Aspuru-Guzik, A. (2018a). Strategies for quantum computing molecular energies using the unitary coupled cluster ansatz. *Quantum Science and Technology*, 4(1):014008. 24, 27, 56, 57

Romero, J., Babbush, R., McClean, J. R., Hempel, C., Love, P. J., and Aspuru-Guzik, A. (2018b). Strategies for quantum computing molecular energies using the unitary coupled cluster ansatz. *Quantum Science and Technology*, 4(1):014008. Publisher: IOP Publishing. 26, 27, 82, 84

Rosenblum, S., Reinhold, P., Mirrahimi, M., Jiang, L., Frunzio, L., and Schoelkopf, R. J. (2018). Fault-tolerant detection of a quantum error. *Science*, 361(6399):266–270. Publisher: American Association for the Advancement of Science. 79, 120

Ryan-Anderson, C., Bohnet, J. G., Lee, K., Gresh, D., Hankin, A., Gaebler, J., Francois, D., Chernoguzov, A., Lucchetti, D., Brown, N. C., et al. (2021). Realization of real-time fault-tolerant quantum error correction. *Physical Review X*, 11(4):041058. 7, 78, 119

Ryan-Anderson, C., Brown, N. C., Allman, M. S., Arkin, B., Asa-Attuah, G., Baldwin, C., Berg, J., Bohnet, J. G., Braxton, S., Burdick, N., Campora, J. P., Chernoguzov, A., Esposito, J., Evans, B., Francois, D., Gaebler, J. P., Gatterman, T. M., Gerber, J., Gilmore, K., Gresh, D., Hall, A., Hankin, A., Hostetter, J., Lucchetti, D., Mayer, K., Myers, J., Neyenhuis, B., Santiago, J., Sedlacek, J., Skripka, T., Slattery, A., Stutz, R. P., Tait, J., Tobey, R., Vittorini, G., Walker, J., and Hayes, D. (2022). Implementing Fault-tolerant Entangling Gates on the Five-qubit Code and the Color Code. arXiv:2208.01863 [quant-ph]. 121, 129

Saffman, M. (2019). Quantum computing with neutral atoms. *National Science Review*, 6(1):24–25. 6

Sagastizabal, R., Bonet-Monroig, X., Singh, M., Rol, M. A., Bultink, C. C., Fu, X., Price, C. H., Ostroukh, V. P., Muthusubramanian, N., Bruno, A., Beekman, M., Haider, N., O'Brien, T. E., and DiCarlo, L. (2019a). Experimental error mitigation via symmetry verification in a variational quantum eigensolver. *Phys. Rev. A*, 100:010302. 8, 53

Sagastizabal, R., Bonet-Monroig, X., Singh, M., Rol, M. A., Bultink, C. C., Fu, X., Price, C. H., Ostroukh, V. P., Muthusubramanian, N., Bruno, A., Beekman, M., Haider, N., O'Brien, T. E., and DiCarlo, L. (2019b). Experimental error mitigation via symmetry verification in a variational quantum eigensolver. *Physical Review A*, 100(1):010302. Publisher: American Physical Society. 8

Schumacher, B. (1995). Quantum coding. *Physical Review A*, 51(4):2738–2747. 15

Shee, Y., Tsai, P.-K., Hong, C.-L., Cheng, H.-C., and Goan, H.-S. (2022). Qubit-efficient encoding scheme for quantum simulations of electronic structure. *Physical Review Research*, 4(2):023154. 24, 82, 113

Shor, P. (1994). Algorithms for quantum computation: discrete logarithms and factoring. In *Proceedings 35th Annual Symposium on Foundations of Computer Science*, pages 124–134. 4

Shor, P. (1996). Fault-tolerant quantum computation. In *Proceedings of 37th Conference on Foundations of Computer Science*, pages 56–65. 5

Shor, P. W. (1995a). Scheme for reducing decoherence in quantum computer memory. *Physical Review A*, 52(4):R2493–R2496. 5

Shor, P. W. (1995b). Scheme for reducing decoherence in quantum computer memory. *Physical review A*, 52(4):R2493. 78

Shor, P. W. (1999). Polynomial-time algorithms for prime factorization and discrete logarithms on a quantum computer. *SIAM review*, 41(2):303–332. 4

Sivak, V., Eickbusch, A., Royer, B., Singh, S., Tsioutsios, I., Ganjam, S., Miano, A., Brock, B., Ding, A., Frunzio, L., et al. (2023). Real-time quantum error correction beyond break-even. *Nature*, 616(7955):50–55. 7, 78, 119

Smart, S. E. and Mazziotti, D. A. (2020). Efficient two-electron ansatz for benchmarking quantum chemistry on a quantum computer. *Phys. Rev. Research*, 2:023048. 53

Smil, V. (2004). World history and energy. *Encyclopedia of energy*, 6(558). 1

Smil, V. (2018). *Energy and civilization: a history*. MIT press. 1

Smith, A., Kim, M. S., Pollmann, F., and Knolle, J. (2019). Simulating quantum many-body dynamics on a current digital quantum computer. *npj Quantum Information*, 5(1):1–13. Publisher: Nature Publishing Group. 10

Sokolov, I. O., Barkoutsos, P. K., Ollitrault, P. J., Greenberg, D., Rice, J., Pistoia, M., and Tavernelli, I. (2020a). Quantum orbital-optimized unitary coupled cluster methods in the strongly correlated regime: Can quantum algorithms outperform their classical equivalents? *The Journal of chemical physics*, 152(12):124107. 27, 57

Sokolov, I. O., Barkoutsos, P. K., Ollitrault, P. J., Greenberg, D., Rice, J., Pistoia, M., and Tavernelli, I. (2020b). Quantum orbital-optimized unitary coupled cluster methods in the strongly correlated regime: Can quantum algorithms outperform their classical equivalents? *The Journal of Chemical Physics*, 152(12):124107. 52

Sokolov, I. O., Dobrautz, W., Luo, H., Alavi, A., and Tavernelli, I. (2023). Orders of magnitude increased accuracy for quantum many-body problems on quantum computers via an exact transcorrelated method. *Physical Review Research*, 5(2):023174. 10

Solomon, B. D. and Krishna, K. (2011). The coming sustainable energy transition: History, strategies, and outlook. *Energy Policy*, 39(11):7422–7431. 1

Steane, A. M. (1996). Error correcting codes in quantum theory. *Physical Review Letters*, 77(5):793. 5, 78

Sun, Q., Timothy C. Berkelbach, N. S. B., Booth, G. H., Guo, S., Li, Z., Liu, J., McClain, J. D., Sayfutyarova, E. R., Sharma, S., Wouters, S., and Chan, G. K.-L. (2018). Software focuspyscf: the python-basedsimulations of chemistryframework. *WIREs Computational Molecular Science*, 8(1):1340. 42, 65

Suzuki, M. (1993). General decomposition theory of ordered exponentials. *Proceedings of the Japan Academy, Series B*, 69(7):161–166. 27, 84

Suzuki, Y., Endo, S., Fujii, K., and Tokunaga, Y. (2022). Quantum Error Mitigation as a Universal Error Reduction Technique: Applications from the NISQ to the Fault-Tolerant Quantum Computing Eras. *PRX Quantum*, 3(1):010345. 119

Szabo, A. and Ostlund, N. S. (1984). *Modern Quantum Chemistry*. Dover Publications, Mineola, New York. 59

Sørensen, A. and Mølmer, K. (1999). Quantum Computation with Ions in Thermal Motion. *Physical Review Letters*, 82(9):1971–1974. Publisher: American Physical Society. 5

Takagi, R., Endo, S., Minagawa, S., and Gu, M. (2022). Fundamental limits of quantum error mitigation. *npj Quantum Information*, 8(1):1–11. Publisher: Nature Publishing Group. 8

Takita, M., Cross, A. W., Córcoles, A., Chow, J. M., and Gambetta, J. M. (2017). Experimental Demonstration of Fault-Tolerant State Preparation with Superconducting Qubits. *Physical Review Letters*, 119(18):180501. 79, 119

Tang, H. L., Shkolnikov, V., Barron, G. S., Grimsley, H. R., Mayhall, N. J., Barnes, E., and Economou, S. E. (2021). qubit-adapt-vqe: An adaptive algorithm for constructing hardware-efficient ansätze on a quantum processor. *PRX Quantum*, 2(2):020310. 53

Taube, A. G. and Bartlett, R. J. (2006). New perspectives on unitary coupled-cluster theory. *International journal of quantum chemistry*, 106(15):3393–3401. 27, 84

Temme, K., Bravyi, S., and Gambetta, J. M. (2017a). Error mitigation for short-depth quantum circuits. *Physical review letters*, 119(18):180509. 8

Temme, K., Bravyi, S., and Gambetta, J. M. (2017b). Error mitigation for short-depth quantum circuits. *Phys. Rev. Lett.*, 119:180509. 64

Tilly, J., Chen, H., Cao, S., Picozzi, D., Setia, K., Li, Y., Grant, E., Wossnig, L., Rungger, I., Booth, G. H., et al. (2022). The variational quantum eigensolver: a review of methods and best practices. *Physics Reports*, 986:1–128. 83

Tkachenko, N. V., Sud, J., Zhang, Y., Tretiak, S., Anisimov, P. M., Arrasmith, A. T., Coles, P. J., Cincio, L., and Dub, P. A. (2021). Correlation-informed permutation of qubits for reducing ansatz depth in the variational quantum eigensolver. *PRX Quantum*, 2(2):020337. 53

Trotter, H. F. (1959). On the product of semi-groups of operators. *Proceedings of the American Mathematical Society*, 10(4):545–551. 27, 84

Urbanek, M., Camps, D., Van Beeumen, R., and de Jong, W. A. (2020a). Chemistry on quantum computers with virtual quantum subspace expansion. *Journal of Chemical Theory and Computation*, 16(9):5425–5431. 10, 36

Urbanek, M., Nachman, B., and de Jong, W. A. (2020b). Error detection on quantum computers improving the accuracy of chemical calculations. *Phys. Rev. A*, 102:022427. 10, 12, 79, 90, 120

Ville, J.-L., Morvan, A., Hashim, A., Naik, R. K., Lu, M., Mitchell, B., Kreikebaum, J.-M., O'Brien, K. P., Wallman, J. J., Hincks, I., et al. (2021). Leveraging randomized compiling for the qite algorithm. *arXiv preprint arXiv:2104.08785*. 64

Von Burg, V., Low, G. H., Häner, T., Steiger, D. S., Reiher, M., Roetteler, M., and Troyer, M. (2021). Quantum computing enhanced computational catalysis. *Physical Review Research*, 3(3):033055. 3

Vuillot, C. (2017). Is error detection helpful on ibm 5q chips? *arXiv preprint arXiv:1705.08957*. 9, 79, 90, 119

Wallman, J. J. and Emerson, J. (2016a). Noise tailoring for scalable quantum computation via randomized compiling. *Physical Review A*, 94(5):052325. 8, 37

Wallman, J. J. and Emerson, J. (2016b). Noise tailoring for scalable quantum computation via randomized compiling. *Phys. Rev. A*, 94:052325. 62

Wendin, G. (2017). Quantum information processing with superconducting circuits: a review. *Reports on Progress in Physics*, 80(10):106001. Publisher: IOP Publishing. 6

Whitfield, J. D., Biamonte, J., and Aspuru-Guzik, A. (2011a). Simulation of electronic structure hamiltonians using quantum computers. *Molecular Physics*, 109(5):735–750. 52

Whitfield, J. D., Biamonte, J., and Aspuru-Guzik, A. (2011b). Simulation of Electronic Structure Hamiltonians Using Quantum Computers. *Molecular Physics*, 109(5):735–750. arXiv:1001.3855 [physics, physics:quant-ph]. 82

Willsch, D., Willsch, M., Jin, F., De Raedt, H., and Michielsen, K. (2018). Testing quantum fault tolerance on small systems. *Physical Review A*, 98(5):052348. 79, 119

Wineland, D., Monroe, C., Itano, W., King, B., Leibfried, D., Meekhof, D., Myatt, C., and Wood, C. (1999). Experimental Primer on the Trapped Ion Quantum Computer. In *Quantum Computing*, pages 57–84. John Wiley & Sons, Ltd. Section: 3 _eprint: https://onlinelibrary.wiley.com/doi/pdf/10.1002/3527603093.ch3. 5

Wootters, W. K. and Zurek, W. H. (1982). A single quantum cannot be cloned. *Nature*, 299(5886):802–803. Publisher: Nature Publishing Group. 5

Wright, J., Gowrishankar, M., Claudino, D., Lotshaw, P. C., Nguyen, T., McCaskey, A. J., and Humble, T. S. (2022). Numerical simulations of noisy quantum circuits for computational chemistry. *Materials Theory*, 6(1):18. 83

Xia, R. and Kais, S. (2020). Qubit coupled cluster singles and doubles variational quantum eigensolver ansatz for electronic structure calculations. *Quantum Science and Technology*, 6(1):015001. 53

Yamamoto, K., Duffield, S., Kikuchi, Y., and Ramo, D. M. (2024). Demonstrating bayesian quantum phase estimation with quantum error detection. *Physical Review Research*, 6(1):013221. 7, 78, 79, 120

Yeter-Aydeniz, K., Gard, B. T., Jakowski, J., Majumder, S., Barron, G. S., Siopsis, G., Humble, T. S., and Pooser, R. C. (2021). Benchmarking quantum chemistry computations with variational, imaginary time evolution, and krylov space solver algorithms. *Advanced Quantum Technologies*, page 2100012. 36, 42, 52

Yung, M.-H., Whitfield, J. D., Boixo, S., Tempel, D. G., and Aspuru-Guzik, A. (2014). Introduction to Quantum Algorithms for Physics and Chemistry. In *Quantum Information and Computation for Chemistry*, pages 67–106. John Wiley & Sons, Ltd. _eprint: https://onlinelibrary.wiley.com/doi/pdf/10.1002/9781118742631.ch03. 4

Zhang, F., Gomes, N., Berthusen, N. F., Orth, P. P., Wang, C.-Z., Ho, K.-M., and Yao, Y.-X. (2021). Shallow-circuit variational quantum eigensolver based on symmetry-inspired hilbert space partitioning for quantum chemical calculations. *Physical Review Research*, 3(1):013039. 83

Zhang, Y., Cincio, L., Negre, C. F. A., Czarnik, P., Coles, P. J., Anisimov, P. M., Mniszewski, S. M., Tretiak, S., and Dub, P. A. (2022). Variational quantum eigensolver with reduced circuit complexity. *npj Quantum Information*, 8(1):1–10. Number: 1 Publisher: Nature Publishing Group. 82, 83

Zhong, H.-S., Wang, H., Deng, Y.-H., Chen, M.-C., Peng, L.-C., Luo, Y.-H., Qin, J., Wu, D., Ding, X., Hu, Y., Hu, P., Yang, X.-Y., Zhang, W.-J., Li, H., Li, Y., Jiang, X., Gan, L., Yang, G., You, L., Wang, Z., Li, L., Liu, N.-L., Lu, C.-Y., and Pan, J.-W. (2020). Quantum computational advantage using photons. *Science*, 370(6523):1460–1463. Publisher: American Association for the Advancement of Science. 6

Zhong, Y. P., Wang, Z. L., Martinis, J. M., Cleland, A. N., Korotkov, A. N., and Wang, H. (2014). Reducing the impact of intrinsic dissipation in a superconducting circuit by quantum error detection. *Nature Communications*, 5(1):3135. Number: 1 Publisher: Nature Publishing Group. 79, 119

Vita

Meenambika Gowrishankar spent her childhood in India and Bahrain. She received her Bachelor of Science in Chemistry and Biology and Master of Science in Chemistry from Colorado State University-Pueblo and University of Oregon, respectively. Between the different educational pursuits she also worked in research and development at different companies before deciding to pursue a Doctor of Philosophy degree in Energy Science and Engineering at the University of Tennessee, Knoxville with a focus on Quantum Computing. She is excited about leveraging quantum error correction and mitigation techniques for advancing quantum computing technologies towards fault tolerance. She hopes to pursue a career in research through a post-doctoral position at a research institute or research and development position in industry.